

THESIS

A SIMULATION METHOD AND LABORATORY BRAKE FRICTION DYNAMOMETER
FOR TRIBOLOGY STUDIES

Submitted by

Peter Thompson Nivala

Mechanical Engineering

In partial fulfillment of the requirements

For the Degree of Master of Science

Colorado State University

Fort Collins, Colorado

Summer 2009

COLORADO STATE UNIVERSITY

May 1st, 2009

WE HEREBY RECOMMEND THAT THE THESIS PREPARED UNDER OUR SUPERVISION BY PETER NIVALA ENTITLED, "A SIMULATION METHOD AND LABORATORY BRAKE FRICTION DYNAMOMETER FOR TRIBOLOGY STUDIES" BE ACCEPTED AS FULFILLING IN PART REQUIREMENTS FOR THE DEGREE OF MASTER OF SCIENCE.

Committee on Graduate work

Dr. Paul R. Heyliger

Dr. Hiroshi Sakurai

Dr. Donald W. Radford, Advisor

Dr. Allan T. Kirkpatrick, Department Head

ABSTRACT OF THESIS

A SIMULATION METHOD AND LABORATORY BRAKE FRICTION DYNAMOMETER FOR TRIBOLOGY STUDIES

Two of the most important parameters of brake system design are the frictional and wear capabilities of the rotor and pad materials. These parameters must meet minimum design requirements in an effort to enhance friction and reduce wear to improve the performance and life of brake system components. The frictional and wear performance of the rotor and pad materials can be assessed through laboratory brake dynamometer testing and evaluation.

In the current study, a wear testing simulation and an inertia laboratory brake dynamometer were developed to resolve differences in wear rates of brake materials. Dynamometer testing was conducted to verify the logic of the simulation and the functionality of the dynamometer by measuring wear rates of brake rotor material samples, some of which were subjected to cryogenic heat treatment to modify their wear rates, at varying brake application pressures.

Dynamometer testing established that the wear simulation and inertia laboratory brake dynamometer developed during the current study could function together as a suitable tribological experimental apparatus. Specifically, dynamometer testing demonstrated the ability of the experimental apparatus to resolve differences in wear rates of brake materials due to variations in brake application pressure at relatively short test durations; however, dynamometer test results did not show conclusive evidence to suggest an advantage in subjecting the rotor materials used in the current study to cryogenic treatment to lower the rotor or pad wear rates.

Peter Thompson Nivala
Mechanical Engineering Department
Colorado State University
Fort Collins, CO 80523
Summer 2009

ACKNOWLEDGEMENTS

The author would like to thank Dr. Donald Radford for his guidance, patience and the continued opportunities affording the author persistent challenge and growth as a developing engineer. The author would also like to thank the remaining committee members, Dr. Heyliger and Dr. Sakurai, for their time and contributions towards this thesis effort. In addition, many thanks to Dr. Patrick Fitzhorn, Dr. Susan James, Gene Fatton, Terry Jensen, Austin Dvorak, Nick Gruber, and Blake Holloway. Lastly but not least, a special thanks to my family, specifically my mother and fiancée for their invaluable advice and eternal patience during this long and trying journey.

TABLE OF CONTENTS

Chapters

ABSTRACT OF THESIS	III
ACKNOWLEDGEMENTS	IV
TABLE OF CONTENTS	V
LIST OF FIGURES.....	VIII
LIST OF TABLES.....	XI
LIST OF ABBREIVATIONS, SYMBOLS AND VARIABLES	XII
1. INTRODUCTION.....	1
1.1. Overview of brake systems.....	1
1.1.1. Energy conversion principles.....	1
1.1.2. Modern production passenger automobiles	3
1.1.3. Modern rotor and pad friction materials.....	4
1.1.4. Testing and evaluation.....	5
1.2. Overview of tribology.....	7
1.2.1. Friction	7
1.2.2. Wear	9
1.2.3. Testing and measurement.....	10
1.2.4. Treatments to increase wear resistance.....	10
1.3. Objectives of study.....	11
1.4. Research approach.....	11
2. WEAR SIMULATION DEVELOPMENT	13
2.1. Objectives	13
2.1.1. Full-scale brake system.....	13
2.1.2. Generate measurable wear rates	13
2.1.3. Maximize wear rate to minimize wear test duration.....	16
2.2. Bedding procedure development.....	16
2.2.1. Differential scanning calorimetry.....	19
2.2.2. SAE J2522 standard.....	25
2.3. Wear procedure development.....	26
2.3.1. ASTM G99-05 standard.....	26
2.3.2. SAE J2522 standard.....	27

3.	EXPERIMENTAL APPARATUS DEVELOPMENT	28
3.1.	Objectives	28
3.2.	Layout overview	28
3.3.	Temperature system	28
3.3.1.	Exergen non-contact, infrared thermocouple calibration	30
3.4.	Pressure system	32
3.4.1.	Hydraulic system	32
3.4.2.	Electric linear actuator and master cylinder	33
3.4.3.	Pressure transducer	36
3.5.	Drive system	38
3.5.1.	Electric motor	39
3.5.2.	Clutch system	40
3.5.3.	Power transmission	41
3.5.4.	Shaft encoder	44
3.6.	Power system	46
3.6.1.	Elgar programmable power supply	47
3.6.2.	Philips programmable power supply	47
3.6.3.	Battery-based power supplies	49
3.7.	Measurement and control system	50
3.7.1.	Hardware connections	50
3.7.2.	Hardware noise interference	55
3.7.3.	Software programs	57
3.7.4.	Load cell transducer	60
3.8.	Equations	61
3.8.1.	Coefficient of friction	61
3.8.2.	Sliding distance	61
3.8.3.	Wear rate	62
3.9.	Safety system	62
3.10.	Implementation of Inertia	64
3.10.1.	Mechanical	64
3.10.2.	Electrical	65
3.10.3.	Energy compensation	66
3.10.4.	Energy equivalent	66
4.	VERIFICATION	68
4.1.	Objectives	68
4.2.	Brake system components	68
4.2.1.	Caliper	68
4.2.2.	Pads	69
4.2.3.	Rotors	70
4.2.4.	Brake hat	74
4.2.5.	Caliper mount	76
4.3.	Procedure	77
4.3.1.	Bedding test procedure	78
4.3.2.	Wear test procedure	82
5.	RESULTS AND DISCUSSION	85
5.1.	Results	85
5.1.1.	Experimental apparatus test data	85
5.1.2.	Mass loss	90

5.1.3.	Wear rate	95
5.1.4.	Optical microscopy	98
5.2.	Discussion	100
5.2.1.	Resolved wear rates	100
5.2.2.	Coefficient of friction	104
5.2.3.	Optical microscopy	106
5.2.4.	Experimental apparatus failures	106
5.2.5.	Summary.....	108
6.	CONCLUSIONS.....	110
6.1.	Significant findings	111
6.2.	Future work	111
	REFERENCES.....	113
	APPENDICES	117
A.	Differential scanning calorimetry	118
A.1.	Measurement principle	118
A.2.	Test results	119
B.	Test details.....	122
B.1.	SAE J2522 standard	122
B.2.	Bedding test procedure.....	124
C.	Equation development	127
C.1.	Vehicle deceleration	127
C.2.	Brake rotor surface temperature.....	128
C.3.	Effective brake rotor radius.....	129
C.4.	Coefficient of friction	130
D.	Wiring connections.....	131
D.1.	Shielded connector block.....	131
E.	Experimental apparatus design drawings.....	133
E.1.	Brake actuator mount	134
E.2.	Shaft encoder mount	135
E.3.	Shaft encoder toothed wheels	136
E.4.	Brake rotor	137
E.5.	Brake hat.....	138
E.6.	Caliper mount.....	139
E.7.	Load cell lower mount.....	140
E.8.	Load cell upper mount	141
F.	Experimental apparatus exploded views	142
F.1.	Brake actuator mount	143
F.2.	Shaft encoder mount	144
F.3.	Brake rotor and hat	145
F.4.	Caliper mount.....	146
F.5.	Load cell.....	147
G.	Verification Results	148
G.1.	Bedding test procedures.....	148
G.2.	Wear test procedures	151
G.3.	Brake rotor and pad mass loss	165

LIST OF FIGURES

Figure 2.1: Disk-on-disk geometry as used for tribological testing of rolling contact [37].....	14
Figure 2.2: Typical friction force profiles observed during running-in [39]	17
Figure 2.3: DSC plot of a low-metal brake pad friction material as measured by Guipu, et al. [15]	19
Figure 2.4: DTA and TGA plots of the phenolic binding resin found in a semi-metallic brake pad friction material as measured by Ramousse, et al. [18]	20
Figure 2.5: TGA plot of the semi-metallic brake pad friction material as measured by Ramousse, et al. [18].....	21
Figure 2.6: Seiko Instruments Inc. DSC220C differential scanning calorimeter	22
Figure 2.7: Temperature detail for first DSC test	23
Figure 2.8: Temperature detail for second DSC test	24
Figure 2.9: DSC test results from the first test set for the first temperature exposure of the <i>new</i> compound sample	25
Figure 3.1: Environmental chamber exhaust system as-installed in the experimental apparatus.	29
Figure 3.2: Omega K-type thermocouple probe shown with brass adapter	29
Figure 3.3: Exergen IRTc.3x non-contact, infrared thermocouple and mount.....	30
Figure 3.4: Third-order calibration polynomial fitted to the measured rotor surface temperature data	31
Figure 3.5: Rotor surface temperature as measured by a k-type thermocouple, Exergen IRTc.3x (raw), and Exergen IRTc.3x (as-calibrated)	31
Figure 3.6: Hydraulic system schematic	33
Figure 3.7: Linear actuator coupled to Tilton master cylinder as-installed (top) and as-designed (bottom)	34
Figure 3.8: Haydon DCM8055 high performance microstepping chopping driver as-installed in the experimental apparatus	35
Figure 3.9: Schematic of electric linear actuator, driver, power supply, and controller	36
Figure 3.10: MSP 300 pressure transducer as-installed in the experimental apparatus	37
Figure 3.11: Tubes 'N Hoses custom rubber hydraulic line	38
Figure 3.12: Drive system schematic.....	38
Figure 3.13: Toshiba Corporation electric, 3 phase induction motor as-installed in the experimental apparatus	39
Figure 3.14: Cutler-Hammer VFD as-installed in the experimental apparatus	40
Figure 3.15: Clutch system schematic	41
Figure 3.16: Clutch system showing flywheel, clutch, pressure plate, hydraulic release bearing, hydraulic plumbing, and electromechanical linear actuator	42
Figure 3.17: Power Transmission as-installed in the experimental apparatus	43
Figure 3.18: Shaft encoder with 26-toothed wheel as-installed (left) and as-designed (right)	45
Figure 3.19: Circuit diagram of Omron SX770 photomicrosensor and measurement system showing placement of necessary resistor (R) to successfully measure output.....	45
Figure 3.20: Power system schematic	48
Figure 3.21: Elgar AT8000A programmable power supply	48
Figure 3.22: Philips PM2812 programmable power supply	49
Figure 3.23: Custom built 27 VDC battery power supply	49
Figure 3.24: Custom built 24 VDC battery power supply	50
Figure 3.25: Measurement and control system hardware components.....	51
Figure 3.26: National Instruments SCB-68 I/O connector block.....	53
Figure 3.27: National Instruments USB-9211A thermocouple DAQ unit	53

Figure 3.28: Circuit schematic of a single SCB-68 analog input channel with single-pole, low-pass filter components (R, C) and bias resistor (R_b).....	57
Figure 3.29: Manual operation program front panel	58
Figure 3.30: Automated operation program front panel.....	59
Figure 3.31: Manual operation program state machine diagram.....	59
Figure 3.32: Automated operation program state machine diagram	60
Figure 3.33: Safety system schematic.....	63
Figure 3.34: Eaton Cutler-Hammer mushroom pushbuttons as-installed on the door frame (left) and on a mobile chassis (right)	63
Figure 4.1: Wilwood brake pad compound coefficient of friction verses temperature profiles [50].....	80
Figure 4.2: Wilwood Dynalite billet single caliper.....	69
Figure 4.3: Wilwood PolyMatrix A brake pads	70
Figure 4.4: As manufactured ASTM A36 steel rotor	72
Figure 4.5: ICE cryogenic treatment process profile [51].....	74
Figure 4.6: Brake hat as-manufactured (left) and as-designed (right).....	75
Figure 4.7: Caliper mount as-manufactured with thermocouple probe and bushings installed (left) and as-designed (right).....	77
Figure 5.1: Bedding test data for control test specimen 1	86
Figure 5.2: Wear test data for control test specimen 1, repetition 1	87
Figure 5.3: Average coefficient of friction verses sliding distance (km).....	90
Figure 5.4: Cumulative brake rotor mass loss (%) verses sliding distance (km).....	91
Figure 5.5: Progression of brake rotor wear for treated test specimen 3	92
Figure 5.6: Cumulative brake pad mass loss (%) verses sliding distance (km)	93
Figure 5.7: Brake rotor wear rate (mg / km) verses sliding distance (km).....	95
Figure 5.8: Brake pad wear rate (mg / km) verses sliding distance (km)	97
Figure 5.10: Brake rotor surface images of control test specimen 2 (magnification: 40x).....	98
Figure 5.11: Brake rotor surface images of treated test specimen 2 (magnification: 40x)	98
Figure 5.12: Brake pad surface images of control test specimen 2 (magnification: 40 x).....	99
Figure 5.13: Brake pad surface images of treated test specimen 2 (magnification: 40 x).....	99
Figure 5.14: Coefficient of friction variation during the first 12 cycles for each set of 100 cycles of control test specimen 1, repetition 7.....	105
Figure A.1: Seiko Instruments Inc. DSC220C chamber structure [42]	118
Figure A.2: DSC test results from the first test set for the first temperature exposure of the <i>new</i> compound sample	119
Figure A.3: DSC test results from the first test set for the first temperature exposure of the <i>used</i> compound sample	119
Figure A.4: DSC test results from the first test set for the second temperature exposure of the <i>new</i> compound sample.....	120
Figure A.5: DSC test results from the first test set for the third temperature exposure of the <i>new</i> compound sample	120
Figure A.6: DSC test results from the second test set for the <i>new</i> compound sample	121
Figure A.7: DSC test results from the second test set for the <i>used</i> compound sample	121
Figure D.1: SCB-68 wiring connections	132
Figure E.1: Brake actuator mount design drawing.....	134
Figure E.2: Shaft encoder mount design drawing.....	135
Figure E.3: Shaft encoder toothed wheels design drawing	136
Figure E.4: Brake rotor design drawing	137
Figure E.5: Brake hat design drawing.....	138
Figure E.6: Caliper mount design drawing.....	139
Figure E.7: Load cell lower mount design drawing	140
Figure E.8: Load cell upper mount design drawing	141
Figure F. 1: Brake actuator mount exploded view	143
Figure F.2: Shaft encoder exploded view	144
Figure F.3: Brake rotor and hat exploded view	145
Figure F.4: Caliper mount exploded view	146
Figure F.5: Load cell exploded view	147

Figure G.1: Bedding test procedure results for control test specimen 1	148
Figure G.2: Bedding test procedure results for treated test specimen 1	149
Figure G.3: Bedding test procedure results for control test specimen 2.....	149
Figure G.4: Bedding test procedure results for treated test specimen 2	150
Figure G.5: Bedding test procedure results for treated test specimen 3	150
Figure G.6: Wear test procedure results for control test specimen 1, repetition 1	151
Figure G.7: Wear test procedure results for control test specimen 1, repetition 2	151
Figure G.8: Wear test procedure results for control test specimen 1, repetition 3	152
Figure G.9: Wear test procedure results for control test specimen 1, repetition 4	152
Figure G.10: Wear test procedure results for control test specimen 1, repetition 5	153
Figure G.11: Wear test procedure results for control test specimen 1, repetition 6	153
Figure G.12: Wear test procedure results for control test specimen 1, repetition 7	154
Figure G.13: Wear test procedure results for control test specimen 1, repetition 8	154
Figure G.14: Wear test procedure results for treated test specimen 1, repetition 1	155
Figure G.15: Wear test procedure results for treated test specimen 1, repetition 2.....	155
Figure G.16: Wear test procedure results for treated test specimen 1, repetition 3.....	156
Figure G.17: Wear test procedure results for treated test specimen 1, repetition 4	156
Figure G.18: Wear test procedure results for treated test specimen 1, repetition 5.....	157
Figure G.19: Wear test procedure results for treated test specimen 1, repetition 6.....	157
Figure G.20: Wear test procedure results for treated test specimen 1, repetition 7.....	158
Figure G.21: Wear test procedure results for treated test specimen 1, repetition 8.....	158
Figure G.22: Wear test procedure results for control test specimen 2, repetition 1	159
Figure G.23: Wear test procedure results for control test specimen 2, repetition 2	159
Figure G.24: Wear test procedure results for control test specimen 2, repetition 3	160
Figure G.25: Wear test procedure results for control test specimen 2, repetition 4	160
Figure G.26: Wear test procedure results for treated test specimen 2, repetition 1	161
Figure G.27: Wear test procedure results for treated test specimen 2, repetition 2.....	161
Figure G.28: Wear test procedure results for treated test specimen 2, repetition 3.....	162
Figure G.29: Wear test procedure results for treated test specimen 2, repetition 4	162
Figure G.30: Wear test procedure results for treated test specimen 3, repetition 1	163
Figure G.31: Wear test procedure results for treated test specimen 3, repetition 2.....	163
Figure G.32: Wear test procedure results for treated test specimen 3, repetition 3.....	164
Figure G.33: Wear test procedure results for treated test specimen 3, repetition 4.....	164
Figure G.34: Cumulative brake rotor mass loss (g) verses sliding distance (km)	166
Figure G.35: Cumulative brake pad mass loss (g) verses sliding distance (km).....	167

LIST OF TABLES

Table 2.1: Predictions of wear test durations for various heat treatment combinations and magnitudes of mass loss	15
Table 2.2: Temperature cycle detail for second DSC test	24
Table 4.1: Number of brake applications per wear test procedure repetition for the three test specimen groups	84
Table 5.1: Individual test specimen sliding distance (km) verses test procedure	89
Table 5.2: Cumulative brake rotor mass loss (%)	91
Table 5.3: Cumulative brake pad mass loss (%)	93
Table 5.4: Brake rotor wear rate (mg / km)	95
Table 5.5: Brake pad wear rate (mg / km)	97
Table 5.6: Results for test specimen group 1, wear repetition 1	101
Table 5.7: Test parameters used in experimentally determining wear rates	102
Table B.1: Green Mu Characteristic section detail [35]	122
Table B.2: Burnish section detail [35]	123
Table B.3: Characteristic Value section detail [35]	123
Table B.4: First 50 cycles of bedding test procedure	125
Table B.5: Second 50 cycles of bedding test procedure	126
Table G.1: Individual brake rotor mass loss (g)	165
Table G.2: Individual brake pad mass loss (g)	165
Table G.3: Cumulative brake rotor mass loss (g)	166
Table G.4: Cumulative brake pad mass loss (g)	167

LIST OF ABBREIVATIONS, SYMBOLS AND VARIABLES

Abbreviations:

- *AC* – alternating current
- *AGM* – absorbent glass mat
- *AMD* – Advanced Micro Devices, Inc.
- *AN* – Army-Navy fitting
- *ASTM* – American Society for Testing and Materials
- *CO* – state of Colorado
- *DAQ* – data acquisition
- *DC* – direct current
- *DLS* – Wilwood Dynalite billet single caliper
- *DOT* – U.S. Department of Transportation
- *DSC* – differential scanning calorimetry
- *DTA* – differential thermal analysis
- *GPIB* – general purpose interface bus
- *ID* – inner diameter
- *I/O* – input and output
- *ICE* – International Cryogenic Engineering, Inc.
- *MP* - megapixel
- *NI* – National Instruments
- *NPT* – national pipe thread tapered
- no. – number
- *OD* – outer diameter
- *PCI* – peripheral component interconnect
- *PID* – proportional, integral, derivative control

- *RAM* – random access memory
- *SAE* – Society of Automotive Engineers
- *SCB-68* – shielded connector block with 68 pins
- *SSR* – solid state relay
- *TGA* – thermogravimetric analysis
- *TTL* – transistor-transistor logic
- *UPS* – uninterruptible power supply
- *USB* – universal serial bus
- *VFD* – variable frequency drive

Unit symbols:

- °C – degree Celsius (temperature)
- °C/min – degree Celsius per minute (temperature rate)
- °F – degree Fahrenheit (temperature)
- *A* – ampere (electrical current)
- *Ah* – ampere-hour (electrical charge)
- *cm* – centimeter (length)
- *F* – farad (electrical capacitance)
- *ft* – foot (length)
- *GB* – gigabyte (computer memory)
- *GHz* – gigahertz (frequency)
- *g* – gram (mass)
- g/km – gram per kilometer (wear rate)
- *hp* – horsepower (power)
- *hr* – hour (time)
- *hrs* – hours (time)
- *Hz* – Hertz (frequency)

- *in* – inch (length)
- in^2 – inch-squared (area)
- $\frac{in}{step}$ – inch per step (stepper motor resolution)
- *J* – Joule (energy)
- $\frac{J}{kg^{\circ}C}$ – Joule per kilogram degree Celsius (specific heat)
- *kg* – kilogram (mass)
- $kg\text{-}m^2$ – kilogram meter-squared (moment of inertia)
- $\frac{kg}{m^2}$ – kilogram per meter-squared (indentation hardness)
- $\frac{kg}{m^3}$ – kilogram per meter-cubed (density)
- *kHz* – kilohertz (frequency)
- *km* – kilometer (length)
- *kph* – kilometer per hour (velocity)
- *kN* – kilonewton (force)
- *kΩ* – kilo-ohm (electrical resistance)
- *kPa* – kilopascal (pressure)
- *lb_f* – pound-force (force)
- *MHz* – Megahertz (frequency)
- *MPa* – Megapascal (pressure)
- *m* – meter (length)
- m^2 – meter-squared (area)
- m^3 – meter-cubed (volume)
- $\frac{m}{s}$ – meter per second (velocity)
- $\frac{m}{s^2}$ – meter per second-squared (acceleration)
- μF – microfarad (electrical capacitance)
- μm – micrometer (length)
- μs – microsecond (time)
- *mA* – milliampere (electrical current)

- mg – milligram (mass)
- mg/km – milligram per kilometer (wear rate)
- mm – millimeter (length)
- mg/km – milligram per kilometer (wear rate)
- ms – millisecond (time)
- mV – millivolt (electrical potential)
- min – minute (time)
- mph – miles per hour (velocity)
- ns – nanosecond (time)
- N – newton (force)
- $N\cdot m$ – newton meter (work energy)
- Ω – ohm (electrical resistance)
- Pa – pascal (pressure)
- psi – pound-force per inch-squared (pressure)
- rad – radian (angle)
- rpm – revolution per minute (rotational velocity)
- s – second (time)
- tpr – teeth per revolution (dimensionless)
- VAC – volts of alternating current (electrical potential)
- VDC – volts of direct current (electrical potential)
- W – Watt (power)
- $W/m^{\circ}C$ – (thermal conductivity)
- W/m^2 – Watt per meter-squared (heat flux)

Variable symbols:

- $\%_{fb}$ – front brake proportioning (%)
- $\%_{fm}$ – front static mass distribution (%)

- Δm_{pad} – brake pad mass loss (kg)
- Δm_{rotor} – brake rotor mass loss (kg)
- ΔT_b – maximum rotor surface temperature ($^{\circ}\text{C}$)
- ΔW – material loss during wear (g)
- ρ_r – rotor density (kg/m^3)
- τ_f – front brake torque (N-m)
- τ_r – rear brake torque (N-m)
- μ – coefficient of friction (dimensionless)
- μ_b – brake coefficient of friction (dimensionless)
- μ_{fb} – front brake coefficient of friction (dimensionless)
- μ_{ft} – front tire coefficient of friction (dimensionless)
- μ_{rb} – rear brake coefficient of friction (dimensionless)
- μ_{rt} – rear tire coefficient of friction (dimensionless)
- μ_t – tire coefficient of friction (dimensionless)
- ω – angular velocity (rad/s)
- ω_{brake} – brake rotor rotational velocity (rpm)
- ω_f – final angular velocity during brake application (rad/s)
- ω_i – initial angular velocity during brake application (rad/s)
- a – vehicle deceleration (m/s^2)
- A_{fp} – front brake caliper piston area (m^2)
- A_i – swept surface area on inside of effective rotor radius (m)
- A_o – swept surface area on outside of effective rotor radius (m)
- A_p – area of single brake piston (m^2)
- A_{rp} – rear brake caliper piston area (m^2)
- A_s – swept rotor surface area (m^2)
- C_{lp} – low-pass filter capacitor value (F)
- c_r – rotor specific heat ($\text{J}/\text{kg}^{\circ}\text{C}$)

- D_{fp} – front brake caliper piston diameter (m)
- D_{fr} – diameter of front brake rotor (m)
- D_p – diameter of single brake piston (m)
- D_r – diameter of brake rotor (m)
- D_{rp} – rear brake caliper piston diameter (m)
- D_{rr} – diameter of rear brake rotor (m)
- $E_b(t)$ – vehicle brake energy at time t (J)
- $F_{\%f}$ – brake system force distribution on front axle (%)
- f_c – low-pass filter cut-off frequency (Hz)
- F_f – total front brake force (N)
- F_{f-max} – maximum front brake force (N)
- $F_{friction}$ – friction force (N)
- F_{fc} – front brake caliper total piston force (N)
- $F_{kinetic}$ – kinetic friction force (N)
- F_{lc} – brake force as measured by the load cell transducer (lb_f)
- F_n – normal force (N)
- F_{normal} – normal force (N)
- F_r – total rear brake force (N)
- F_{r-max} – maximum rear brake force (N)
- F_{rc} – rear brake caliper total piston force (N)
- $F_{rolling}$ – rolling friction force (N)
- F_{static} – static friction force (N)
- f_{teeth} – change of state frequency of the Omron SX770 photomicrosensor (Hz)
- f_{TTL} – measured frequency of the TTL digital signal produced from the Omron SX770 photomicrosensor (Hz)
- h_{cg} – center-of-gravity height (m)
- I – moment of inertia (kg-m²)

- I_{cyc} – cylinder moment of inertia ($\text{kg}\cdot\text{m}^2$)
- $I_{flywheel}$ – mechanical flywheel moment of inertia ($\text{kg}\cdot\text{m}^2$)
- K – wear coefficient (dimensionless)
- KE_{rot} – rotational kinetic energy (J)
- KE_{brake} : vehicle kinetic energy converted during brake application (J)
- k_r – rotor thermal conductivity ($\text{W}/\text{m}\cdot\text{C}$)
- k_w – abrasive wear coefficient (dimensionless)
- L_{fp} – length of front brake pad (m)
- L_{lc} – moment arm of load cell transducer (m)
- L_p – length of brake pad (m)
- L_{rp} – length of rear brake pad (m)
- $L_{sliding}$ – sliding distance of brake pad during brake application (m)
- L_w – length of travel during abrasive wear (m)
- L_{wb} – vehicle wheelbase (m)
- m – vehicle mass (kg)
- m_{cyc} – cylinder mass (kg)
- N_{fc} – number of front brake calipers (dimensionless)
- N_{fp} – number of front brake caliper pistons (dimensionless)
- N_p – number of total brake pistons in single brake caliper (dimensionless)
- N_{rc} – number of rear brake calipers (dimensionless)
- N_{rp} – number of rear brake caliper pistons (dimensionless)
- N_{teeth} – toothed wheel number of teeth (tpr)
- P – brake pressure during wear (psi)
- P_b – brake application pressure as measured by the pressure transducer (psi)
- P_{b1} – brake application pressure for test specimen group 1 (MPa)
- P_{bn} – brake application pressure for test specimen group 2 or 3 (MPa)
- $P_b(t)$ – vehicle instantaneous brake power (W)

- $P_{b-avg}(t)$ – vehicle average brake power between times t_1 to t_2 (W)
- P_{b-avg}^* – single rotor, single side average brake power between times t_1 to t_2 (W)
- p_f – front brake pressure (Pa)
- p_{f-max} – maximum front brake pressure (Pa)
- p_r – rear brake pressure (Pa)
- p_w – indentation hardness of the softer base material under abrasive wear ($^{kg}/m^2$)
- $q''_{(o)}$ – heat flux into rotor surface at onset of brake application ($^W/m^2$)
- $Q_{\%r}$ – brake system thermal energy distribution on rotor (%)
- R_b – bias resistor value (Ω)
- r_{cyc} – cylinder radius (m)
- R_e – effective brake rotor radius (m)
- R_{fe} – effective front brake rotor radius (m)
- R_{ft} – front tire rolling radius (m)
- R_i – inner radius (m)
- R_{lp} – low-pass filter resistor value (Ω)
- R_o – outer radius (m)
- R_{re} – effective rear rotor radius (m)
- R_{rt} – rear tire rolling radius (m)
- t – time (s)
- t_{brake} – brake application time (s)
- T_{cal} – calibrated Exergen IRTc.3x temperature ($^{\circ}F$)
- t_f – duration of brake event (s)
- T_{IRTC} – raw Exergen IRTc.3x temperature ($^{\circ}F$)
- V – rotor speed during wear (rpm)
- $V(t)$ – vehicle velocity at time t ($^m/s$)
- V_i – initial vehicle velocity during brake application ($^m/s$)
- V_f – final vehicle velocity during brake application ($^m/s$)

- V_w – material volume loss due to wear (m^3)
- W_{fs} – front axle static load (N)
- $W'_{avg-pad1}$ – average brake pad wear rate for test specimen group 1 (g/km)
- $W'_{avg-padr}$ – average brake pad wear rate for test specimen group 2 or 3 (g/km)
- $W'_{avg-rotor1}$ – average brake rotor wear rate for test specimen group 1 (g/km)
- $W'_{avg-rotorr}$ – average brake rotor wear rate for test specimen group 2 or 3 (g/km)
- W'_{pad} – brake pad wear rate (g/km)
- W'_{rotor} – brake rotor wear rate (g/km)
- W_{rs} – rear axle static load (N)

1. INTRODUCTION

1.1. Overview of brake systems

Fundamentally, a brake system is designed to convert energy between two forms. When installed on an automobile, for example, the brake system converts kinetic energy, or the energy of motion, to thermal energy. This energy conversion results in an increase in temperature of the brake system and a decrease in speed of the automobile. Energy conversion can take place as the result of several different scientific principles including aerodynamics, electromagnetic induction, and kinetic friction.

Brake systems based on the kinetic friction principle are the most widely used across the vast majority of applications today. Such brake systems can be controlled through mechanical, hydraulic, pneumatic, electric or electromagnetic means. One disadvantage of brake systems based on the kinetic friction principle, is that the relative motion of the surface pair when brought into contact causes the material on both surfaces to wear. Wear results in the eventual need to replace both components of the surface pair. On a brake system, this means replacement of pads and rotors, where it is common to replace pads at shorter intervals than rotors.

1.1.1. Energy conversion principles

The aerodynamic principle is used to achieve energy conversion primarily through an increase in form, or pressure, drag. When a vehicle moves through a fluid, such as air, pressure differences can be created from the separation of the fluid due to the shape of the vehicle. The pressure differential acts on all surfaces not parallel to the fluid velocity and results in a force which opposes the vehicles motion in the direction opposite to the upstream fluid velocity [1]. This opposing force is a component of the total drag force and since it is largely a result of the vehicles shape, is referred to as form drag, streamlining a vehicle attempts to reduce its form

drag [2]. Kinetic energy of the vehicle is converted to thermal energy and stored mainly in the fluid through an increase in its temperature. The aerodynamic principle is mainly utilized in secondary braking systems such as those commonly found on aircraft, including commercial aircraft, military fighter aircraft and even NASA's Space Shuttle, as well as on a select number of production automobiles, such as the Bugatti Veyron. Such secondary braking systems commonly extend movable surface elements into the on coming air stream to increase the form drag of the vehicle and thus reduce its speed.

The electromagnetic induction principle is used to achieve energy conversion primarily through the creation of eddy currents. When a non-magnetic, metal conductor is passed through a changing magnetic field, circulating eddies of current are created within the conductor body. These eddy currents oppose the change of the applied magnetic field giving rise to forces which act to resist the relative motion between the conductor and applied magnetic field source. Kinetic energy of the conductor is converted to thermal energy and stored mainly in the conductor through an increase in its temperature. The electromagnetic induction principle is mainly utilized in primary braking systems such as those found on trains and roller coasters. Such primary braking systems commonly pass a metal rotor, for rotational motion, or a metal rail, for linear motion, through electro- or permanent magnets to reduce the vehicle speed.

The kinetic friction principle is used to achieve energy conversion primarily through chemical bonding. When two surfaces with relative motion are brought into contact, chemical bonds are formed between the contact surfaces. Due to the relative motion, the chemical bonds are soon broken after they are formed. Each chemical bond requires energy to be broken and thus, the relative kinetic energy of the two surfaces in contact is converted to thermal energy and stored mainly between the two surfaces through an increase in their temperatures. The kinetic friction principle is mainly utilized in primary braking systems such as those found on automobiles, motorcycles, bicycles, aircraft, and trains. Such primary braking systems commonly force a stationary pad into contact with a rotating disc or drum to reduce the vehicle speed.

1.1.2. Modern production passenger automobiles

The vast majority of brake systems found in modern production passenger automobiles are controlled hydraulically and are primarily comprised of disc brakes, although drum brakes are still used in select applications. The components of a modern disc brake system for production passenger automobiles include: rotors (discs), pads, calipers, hydraulic fluid, hydraulic lines, proportioning valve, master cylinder, vacuum booster, pedal. A brake rotor is indirectly attached to each tire on the automobile and assumes a rotational motion when the vehicle assumes a linear motion through the interaction of the tire with the road surface. Brake pads are located on either side of the rotor surface and at some distance radially from the center of the rotor. Together, the rotor and pads form the surface pair, or friction couple, necessary to utilize the kinetic friction principle. The brake caliper houses the pads and is fixed to the vehicle. The brake caliper forces the pads into contact with the rotor through the linear movement of one or more internal pistons. Hydraulic pressure provides the motive for piston movement and is conveyed to the pistons through hydraulic lines using incompressible fluid as the powering medium. Hydraulic lines are plumbed between the caliper and the proportioning valve, which decreases the hydraulic pressure to the rear brakes because they require less pressure to reach their maximum braking capability. The master cylinder pressurizes the hydraulic system by converting an applied force into hydraulic pressure through the linear movement of an internal piston, much in the same way the caliper converts hydraulic pressure into force, but in reverse. The applied force acting against the master cylinder is generated from the depression of the brake pedal which, through a lever ratio determined by the brake pedal geometry, multiplies the magnitude of the driver's input force against the brake pedal. For modern production passenger automobiles, an additional multiplication occurs to the driver's input force by means of a vacuum booster, before reaching the master cylinder.

The modern disc brake system for production passenger automobiles is a compromise between stopping performance, safety, cost, reliability, and passenger comfort requiring, among numerous parameters, a high and consistent coefficient of friction, low rotor and pad wear rates,

and minimal noise and vibration characteristics [3]. Rotor and pad material selection plays a vital role in obtaining these parameters during the design of the brake system [4].

1.1.3. Modern rotor and pad friction materials

Several material options exist for the manufacture of brake discs. It is common to use some form of iron, such as grey cast iron, or some form of steel, such as carbon, alloy, or stainless steels. Although brittle, gray cast iron is found on most production passenger automobiles because it is capable of high wear resistance, high thermal conductivity and low production costs [3], [5], [6], [7], [8], [9], [10]. Compositional modifications such as the addition of alloying elements, and heat treatments are used to improve the mechanical and thermal properties of gray cast iron, in part, to avoid thermal cracking and geometry distortion of the rotor [6], [11]. A select number of high-end production passenger automobiles use carbon-ceramic brake discs, such as those found on the Bugatti Veyron, Porsche Carrera GT, or the Chevrolet Corvette ZR1. The advantage of using carbon-ceramic over more conventional iron or steel is mainly: weight savings (approximately 50 percent) [12], higher abrasion resistance resulting in longer rotor life [12], and superior fade resistance resulting in consistent high temperature braking performance [13]. Additional *exotic* materials include carbon-carbon brake discs found on various aircraft and racecars. First introduced to motorsport world by the Brabham Formula One team and its technical director, Gordon Murray, during the late 1970s [14], carbon-carbon brake discs have been continuously developed and remain a staple in the upper echelons of motorsport ever since. The advantage of using carbon-carbon over more conventional iron or steel is mainly: weight savings (approximately 75 percent), and retention of friction properties over a much higher, albeit a narrow, temperature range [14]. Carbon-carbon brake discs are not even found on high-end production passenger automobiles due to the very high, narrow temperature range necessary to achieve optimal performance, far exceeding typical production passenger automobile brake temperatures. Titanium has found limited use as a brake rotor material in motorsport and has even been considered for use in commercial truck brake discs to reduce weight (approximately 37 percent) and to improve corrosion resistance to road salt [6]. Four current disadvantages prevent the widespread commercial use of titanium as a rotor material: low

thermal conductivity relative to gray cast iron, need of surface modification or coating, raw material cost, and machining difficulty [6].

Modern pad friction materials are required to maintain a high and consistent coefficient of friction with a low wear rate across a range of conditions including brake pressure, temperature, disk rotational velocity, and environmental factors, such as humidity, while maintaining a feasible manufacturing cost and minimizing their effects on rotor wear [5], [10], [15]. Modern pad friction materials are complex composites formed from numerous ingredients [3], [4], [5], [8], [15], [16] with such classifications as low-metallic, semi-metallic, non-asbestos inorganic, and sintered metal [17], [18]. The chemical composition and microstructure of the ingredients affect the friction and wear behavior of the pad [10] and typically include various polymers, metals, and ceramics [5], [8] used to form the binder (typically phenolic resin, or rubber), reinforcing fibers (typically asbestos, steel, glass, or organic), solid lubricants, abrasives, and fillers constituting a modern pad friction material [5], [6], [10], [15]. Development relies on experience from empirical or trial-and-error methods [5], [15] and focuses on the optimization of the chemical composition and microstructure of the ingredients to achieve targeted performance parameters for the pad friction materials [10].

1.1.4. Testing and evaluation

It is often necessary to determine the level of performance of a particular brake system with regard to target design parameters. Two of the most important parameters of brake system design are the frictional and wear capabilities of the rotor and pad materials [10], [19], [20], [21] which must meet minimum requirements for, as previously mentioned, stopping performance, safety, cost, reliability, and passenger comfort. The frictional and wear performance of the rotor and pad materials can be measured through vehicle or laboratory brake dynamometer testing and evaluation [5], [10], [19]. The requirements for such tests include development, assessment, selection, certification, classification, quality control, and quality audit of rotor and pad materials [22].

Vehicle testing and evaluation of rotor and pad materials typically takes place on actual roads in various geographical locations, terrains, and seasons [3]. Vehicle testing will subject the

brake system to conditions encountered in the real world for which a dynamometer may not be fully capable of simulating accurately [23]; however, vehicle testing is expensive, and requires a serious resource commitment [10], [23]. Additionally, vehicle testing introduces extraneous measurement variances due to several factors including road conditions, environmental conditions (wind, ambient temperature, humidity, dust, etc.), driving style, traffic, etc. [10], [23], [24].

Several styles of laboratory dynamometers have been developed to reproduce the desirable vehicle test conditions and results while eliminating the extraneous measurement variances to provide more reproducible and reliable measurements costing less time and money compared to vehicle testing and evaluation of rotor and pad materials [10], [22], [24]. Laboratory testing and evaluation of rotor and pad materials is conducted on full-scale or reduced-scale brake dynamometers where test conditions can be controlled [10]; however, results do not always correlate well between vehicle and laboratory dynamometer testing [23], [24].

Full-scale, or inertia, brake dynamometers allow laboratory testing and evaluation of rotor and pad materials using a full-scale brake system and can simulate vehicle testing reasonably well [10]. The typical inertia brake dynamometer consists of a variable speed motor, inertia discs to reproduce the vehicle kinetic energy, automated brake actuation system using hydraulics or pneumatics based on pressure or torque feedback, load/torque cell transducer, pressure transducer, environmental chamber to mount brake system hardware and allow for airflow system to control braking temperatures, and measurement and control system [16]. Inertia brake dynamometers are capable of measuring, controlling, and/or simulating numerous braking parameters including initial brake temperature, deceleration, brake application frequency, rotor rotational velocity, and vehicle kinetic energy [10], [16]; however, inertia brake dynamometer testing is still relatively expensive and time consuming [10], while typically providing a hardware dependent, average coefficient of friction value which fails to describe the friction variation during brake application or report the material coefficient of friction values [17].

As a response to the limitations of full-scale laboratory testing and evaluation, reduced-scale dynamometers have been developed specifically to measure the coefficient of friction from

various combinations of brake friction materials. The typical reduced-scale dynamometer consists of a small friction material sample, approximately 1.0 in. square, pressed against a rotating drum using a pneumatic system [10]. Reduced-scale dynamometers are capable of measuring the coefficient of friction for a given friction couple as a function of drum rotational velocity, application pressure, and temperature allowing friction materials to be evaluated before the completion of the brake system design and prototype manufacturing, potentially saving development time and cost [17], [20]. Reduced-scale dynamometers also eliminate full-scale hardware effects, such as brake system component deflections and local brake pressure variations [17], [20]; however, results produced by reduced-scale dynamometers do not always agree with those produced by full-scale dynamometers due to the differing conditions encountered by friction materials between the two laboratory dynamometers [10], [20]. To produce comparable results requires the use of scaling relations based on constant energy dissipation per unit area (energy density); all linear variables (pad area, effective radius, rolling radius, linear velocity, torque, and inertia) are scaled by the square-root of the scaling factor while the drum rotational velocity, application pressure, temperature, and deceleration are kept constant [20].

1.2. Overview of tribology

Tribology is the study of the interactions between two surfaces possessing relative motion. The science and technology of tribology concerns itself with friction, wear, and lubrication. Although general tribological research tends to focus on friction reduction to lower energy consumption [25], tribological research in the field of brake systems tends to focus on friction enhancement and wear reduction to improve the performance and life of brake system components.

1.2.1. Friction

Friction is the resistance to relative motion between two surfaces in contact expressed as a force. The main type of friction is classified as *dry friction*. Its magnitude is dependant on the values of the coefficient of friction and the normal force for the surface pair. The coefficient of

friction is a dimensionless ratio between the friction force and the normal force as defined in equation 1.1:

$$\mu = \frac{F_{friction}}{F_{normal}} \quad (1.1)$$

The normal force establishes the contact between the surface pair and acts perpendicular, or normal, to the contact interface.

Dry friction can be subdivided into: static, kinetic and rolling friction. Static friction occurs between a surface pair with no relative motion; kinetic friction occurs between a surface pair with relative motion; rolling friction occurs between a surface pair with relative motion where at least one surface is circular and rolls along the other. Static friction occurs, for example, when the clutch is engaged, without slipping, in a vehicle. Kinetic friction occurs, for example, when the brakes are applied in a vehicle. Rolling friction occurs, for example, when the tires on a vehicle roll along the road, or when the rolling elements in a bearing roll along the bearing race. It follows that:

$$F_{static} > F_{kinetic} > F_{rolling} \quad (1.2)$$

The adhesion and abrasion theories of dry friction attempt to explain the behavior of two surfaces in contact generating a friction force. The adhesion theory of dry friction is the most widely used for its tolerable agreement with experimental observations of dry friction behavior [26]. It is based upon the idea that *actual* contact between a surface pair only takes place across a small fraction of the total surface area, across the so-called *asperities* [26]. The applied normal force between the surface pair causes plastic deformation and eventual *microwelding* of some of the asperities; the friction force is required to shear the microwelded asperities [26]. The abrasion theory of dry friction is based upon the idea of *plowing*, where a difference in hardness between the surface pair causes the formation of grooves by plastic deformation or cutting of the softer surface [26]. The work done during the formation of grooves results from the frictional force acting through a distance [26].

1.2.2. Wear

Wear is the loss of material from a surface resulting from the actions of another surface or substance. Although wear for the most part is undesirable, it can have advantageous effects such as those found during the frictional running-in, or *bedding*, of fresh, unworn surfaces in an attempt to optimize friction and wear characteristics during the initial contact of a surface pair in relative motion. The main types of wear include: adhesive, abrasive, corrosive, and fatigue [8], [27]. Surface wear is not necessarily the result of a single type of wear, often combinations of different wear types constitute the overall wear mechanism.

Adhesive wear, much like the adhesion theory of dry friction, involves the loss of material from a surface due to the shearing of microwelded asperities. The adhesive bond formed between surface pair asperities from microwelding is typically stronger than either base material comprising the surface pair and thus the shearing of asperities occurs in one of the two base materials [26], [27]. The resulting wear fragment is attached to the harder base material until it is fully detached by sliding across the surface pair interface [26]. Surface contaminants, such as oxide layers or adsorbed layers of gas, can have a marked impact on the adhesive wear between a surface pair [26].

Abrasive wear, much like the abrasion theory of dry friction, involves the loss of material from a surface due to the plowing or cutting action of an abrading substance against a surface. Abrasive wear can be subdivided into: two-body and three-body wear. Two-body abrasive wear occurs when the abrading substance is another, harder surface [26], [27]. Three-body abrasive wear occurs when the abrading substance consists of loose particles trapped between the surface pair [26], [27].

Corrosive wear involves the loss of material from a surface due to chemical reactions with the environment and is highly temperature dependent [27]. The most familiar form of corrosive wear is rust. Rust forms from the chemical reaction of iron and oxygen in the presence of water.

Fatigue wear involves the loss of material from a surface due to repeated applications of a contact load or temperature, otherwise known as thermal fatigue [27]. Fatigue wear occurs

when spalling or pitting generates loose particles due to cracks which generate, grow, and join with other cracks within the material as a result of the applied cyclic loading [26], [27].

1.2.3. Testing and measurement

ASTM International has produced several standards relevant to friction and wear measurements including abrasive and non-abrasive wear. The standard of interest to the current study was the ASTM International standard, *G99-05: Standard Test Method for Wear Testing with a Pin-on-Disk Apparatus* [28]. *ASTM G99-05* describes a wear test using a pin-on-disk apparatus such that two specimens, a pin and a disk, are pressed together as one specimen is revolved about the disk center until a desired sliding distance is reached. Test parameters for the pin-on-disk apparatus include load, speed, sliding distance, temperature and atmosphere. *ASTM G99-05* suggests obtaining wear results by varying load and speed parameters for a given sliding distance across sets of test specimens. *ASTM G99-05* allows wear rates and coefficient of friction of the specimen pair to be determined.

1.2.4. Treatments to increase wear resistance

Several treatments are available to alter the friction and/or the wear characteristics of a particular material. Treatments largely constitute surface processes such as peening (shot, water jet, or laser), roller burnishing, hardening (explosive, or case), texturing (machining, ion beam, etching, or laser), coating (organic, ceramic, diamond, diffusion, or conversion), etc. [26], [29]. Surface texturing has been shown to reduce the coefficient of friction for a given material [29].

Two treatments claimed to reduce wear significantly involve exposing materials to sub-zero temperatures and are referred to as cold (-80 °C) and cryogenic (-196 °C) treatments. These sub-zero treatments have the potential advantage in that they affect the entire material volume, not simply the surface [30], [31], [32]. Although both sub-zero treatments have shown improvements experimentally, the cryogenic treatment appears to impart a higher wear resistance compared to the cold treatment [32], [33]; no conclusive scientific reasoning for the improvements has been established [32]. It is believed that cryogenic treatment imparts increased wear resistance in steels through the transformation of retained austenite to

martensite, and through the precipitation of fine carbon-carbide particles as a result of the removal of kinetic energy from atoms keeping them apart by the sub-zero temperature [30], [33], [34]. Materials such as hot work steels (H type), oil hardening steels (O type), cold work steels (A, and D type), high speed steels (M type), stainless steels (300, and 400 type) have shown improvements when subjected to cryogenic treatment [32].

1.3. Objectives of study

To demonstrate the ability of a tribological experimental apparatus to resolve differences in wear rates of brake materials, a wear testing simulation and an inertia laboratory brake dynamometer were developed. To verify the logic of the simulation and the functionality of the dynamometer, testing was performed to measure wear rate differences between brake rotor material samples subjected to cryogenic heat treatment and those not subjected to such treatment, at varying brake application pressures.

1.4. Research approach

To develop the wear simulation, two main objectives were identified: to test material samples as integrated components of a full-scale disc brake system and to generate measurable wear rates over reasonably short test durations. The wear simulation consisted of a bedding and a wear procedure, both created based on industry standards [28], [35] while taking advantage of inertia simulation.

An inertia laboratory brake dynamometer was developed to function as a tribological experimental apparatus. As such, the dynamometer needed to be capable of implementing both procedures of the wear simulation, which required the addition of appropriate equipment and instrumentation to be capable of resolving differences in wear rates of brake materials. The dynamometer was comprised of several sub-systems to meet these requirements including temperature, pressure, drive, power, measurement and control, and safety systems.

Five brake material test sets were created to allow verification testing of the wear simulation, including the energy equivalent inertia simulation, and the functionality of the additions to the inertia laboratory brake dynamometer. Each test set consisted of a single brake rotor and

two brake pads, from which three rotors were subjected to cryogenic heat treatment, and each functioned as integrated components of a full-scale brake system installed on the dynamometer. Verification testing consisted of exposing each test set to a single application of the bedding procedure followed by repeated applications of the wear procedure. Brake application pressure was purposely varied across specific test sets to investigate the wear rate sensitivity to brake application pressure. Optical microscopy and mass loss measurements were conducted on both rotor and pads after each verification test. Rotor and pad wear rates were calculated directly from the measured mass loss with respect to the calculated sliding distance.

2. WEAR SIMULATION DEVELOPMENT

2.1. Objectives

A simulation was developed to study wear rates of materials integrated in a full-scale brake system. As such, it was necessary for the simulation as implemented on an experimental apparatus, to generate measurable wear rates over a reasonably short duration. The simulation consisted of two portions: a bedding procedure and a wear procedure.

2.1.1. Full-scale brake system

Implementation of a full-scale brake system would generate wear rates consistent with expected real world observations and allow any wear testing conducted on the experimental apparatus to be vehicle application specific: a brake system from a particular vehicle could be readily tested as it is implemented on the actual vehicle to determine its specific wear rates.

2.1.2. Generate measurable wear rates

Generating measurable mass loss would allow brake rotors and pads to be weighed to determine a wear rate as mass loss per unit time, or mass loss per unit distance. Rate of mass loss would directly control the time to complete a wear test and concerns initially existed over the potential for excessively long wear test durations. A calculation was performed to predict potential wear test durations based upon the work in experimentally determining wear rates of AISI M2 tool steel by Molinari, et al. [36]. In this work by Molinari, et al., dry sliding tests on four samples exposed to various combinations of quenching, tempering, and cryogenic treatments were performed using disk-on-disk geometry at the following test parameters:

- *Load:* 150 N
- *Sliding speed:* 0.8 m/s
- *Sliding distance:* 5 km

Disk-on-disk, or twin-disk, geometry is utilized in tribological testing to investigate adhesive and/or fatigue wear due to rolling contact between two disk surfaces [37]. Typically a disk-on-disk apparatus employs a motor to power one disk, which in turn causes the other disk to rotate due to the contact established when both are forced together (see Figure 2.1) [37].

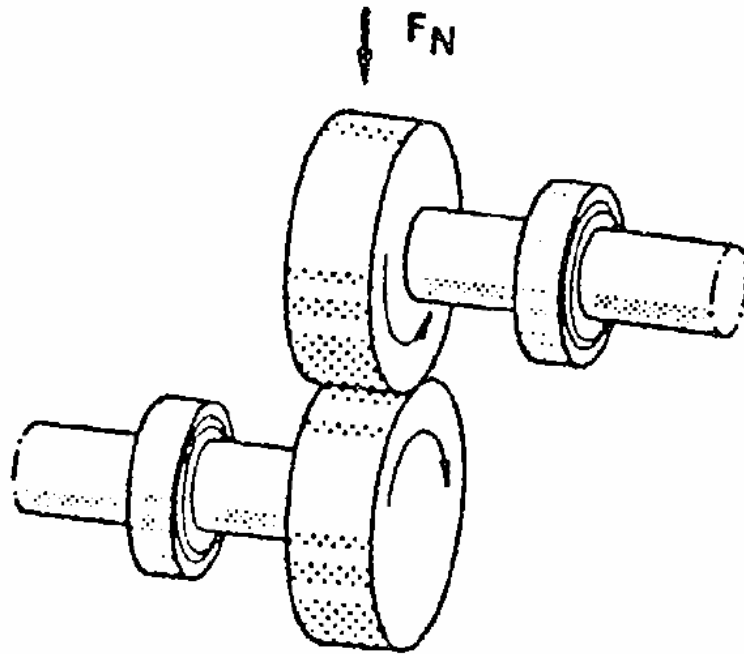


Figure 2.1: Disk-on-disk geometry as used for tribological testing of rolling contact [37]

Heat treatment of the four samples included a vacuum quench (Q) from 1220 °C, a temper cycle (T) at 550 °C for a duration of 2 hrs., and a cryogenic treatment (C) at -196 °C for a duration of 35 hours. The four samples, respective heat treatment combinations, and measured wear rates were [36]:

- Sample A (Q + T + T): 3.7 mg/kg
- Sample B (Q + T + T + C): 1.8 mg/kg
- Sample C (Q + C + T): 2.2 mg/kg
- Sample D (Q + C + T + T): 2.4 mg/kg

Predictions of wear test durations for the current study were made based upon the results from Molinari, et al. for various magnitudes of mass loss for a steel rotor with a rotational speed of

840 rpm and an effective radius of 10 cm (or a sliding speed of 8.8 m/s). The heat treatment combinations used by Molinari, et al. are extended to these predictions, summarized in Table 2.1.

Table 2.1: Predictions of wear test durations for various heat treatment combinations and magnitudes of mass loss

Sample	Wear Rate (mg/km)	0.01 g Mass Loss	0.10 g Mass Loss	1.00 g Mass Loss	10.00 g Mass Loss
A	3.7	0 hr., 3 min.	0 hr., 26 min.	4 hr., 24 min.	43 hr., 58 min.
B	1.8	0 hr., 5 min.	0 hr., 54 min.	9 hr., 2 min.	90 hr., 23 min.
C	2.2	0 hr., 4 min.	0 hr., 44 min.	7 hr., 24 min.	73 hr., 57 min.
D	2.4	0 hr., 4 min.	0 hr., 41 min.	6 hr., 47 min.	67 hr., 47 min.

Although the test duration predictions presented in Table 2.1 appear to be insignificant and potentially easily manageable, several important aspects were noted.

A single gram of mass loss, for instance, would be only 0.06 percent of the total mass for a Formula One carbon-carbon rotor or only 0.02 percent of the total mass for a Champ Car cast iron rotor. If a significantly greater percentage of mass loss were desired, numerous wear tests would be required, thus multiplying the wear test duration significantly. Additionally, a scale not only capable of physically weighing a rotor, but capable of resolving fractions of a gram on a rotor weighing 1.675 kg, would also be required.

Another important aspect noted from the wear test duration predictions was that the calculated durations were for continuous brake applications. Continuous brake applications lasting even just a couple of minutes at moderate pressure would result in a large temperature generation. Uncontrolled, the temperature generation can severely shorten component life expectancy and has the potential to influence test results.

However, it should be noted that the wear rates determined by Molinari, et al. are potentially sensitive to the particular test parameters (load, sliding speed, etc.); if the test parameters are varied the values of the wear rates are likely to change. A full-scale brake system is expected to produce much greater values of the test parameters and therefore potentially different wear rates altogether.

2.1.3. Maximize wear rate to minimize wear test duration

Due to concerns over potential for excessively long wear test durations, an attempt was made to maximize wear rates to generate measurable mass loss over short test durations. It was believed that controlling three key test parameters would result in sufficient wear rates: brake pad coefficient of friction, brake pad application pressure and brake rotor rotational speed.

Okamura and Ono [38] measured increased rotor wear with increased pad aggressiveness. It was believed that pad aggressiveness was solely influenced by the coefficient of friction and controlling it was limited to selecting from commercially available brake pad compounds; however, it is not sufficient to only select a compound with the largest peak coefficient or the greatest sustained coefficient over a certain temperature range. In order to perform at the limit of their capabilities brake pads must be conditioned for use through a process known as *frictional running-in*, or *bedding*, which also functions to condition the brake rotor for use with the brake pad.

It was believed that increasing the brake pad application pressure and/or the brake rotor rotational speed would increase the brake rotor wear rate. Control over both parameters would be possible during dynamometer testing. Although sufficiently high values for both parameters could be attained on the experimental apparatus, an effort was made to maintain realistic values for a given vehicle application.

2.2. Bedding procedure development

Bedding is a wear process intended to optimize the friction and wear characteristics of a surface pair in relative motion during the initial contact of their fresh, unworn surfaces where changes in friction, temperature, and wear rate have been known to occur (see Figure 2.2) [39]. Specifically, for the brake friction couple (rotor and pads), the bedding process attempts to maximize the coefficient of friction to realize peak performance of the brake system [40], [41] and in the process serves three purposes: to establish proper mating (compliant contact surfaces) of the friction couple [39], to *cook* the binding resin from the pad friction surface [40], and to form an uniform friction film on the rotor friction surface [40], [39].

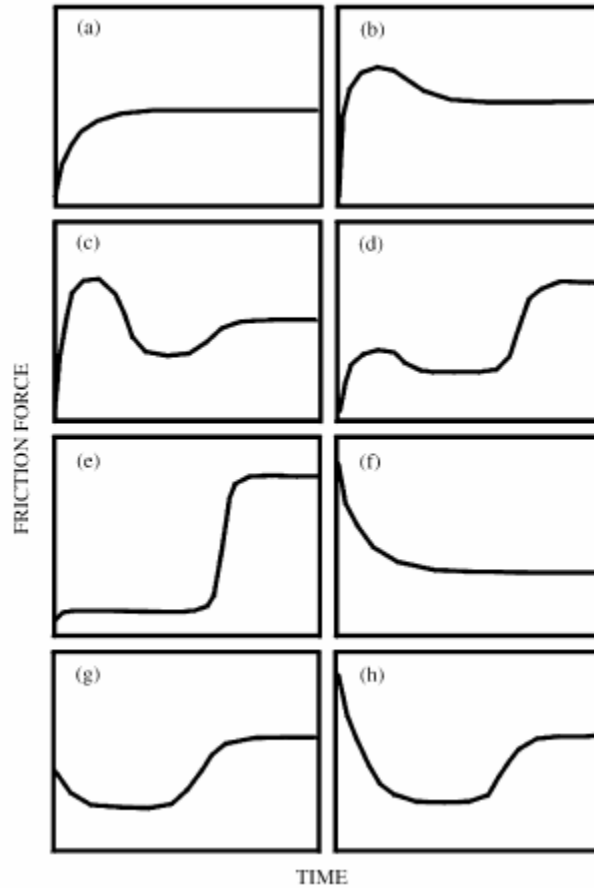


Figure 2.2: Typical friction force profiles observed during running-in [39]

During initial contact, a thin layer of compacted third-body deposits is formed on the friction surfaces of the brake rotor and pads commonly referred to as the transfer layer, or friction film [3], [5], [41]. This thin layer of compacted third-body deposits varies in thickness and uniformity across the friction surfaces where it has been reported to be in excess of 25 μm for pad materials, and to range from less than 1 μm to more than 5 μm for rotor materials [5]. Third-body deposits originate as wear debris generated from the rotor and pads and are subsequently compacted onto the friction surfaces forming the friction film [3]. It has also been suggested that the adhesive mechanism is a factor in the friction film formation on the rotor surface [40] causing material transfer between brake friction surfaces from the shearing of pad asperities which possess a lower shear strength than the rotor material. The creation and destruction of this friction film influences the friction and wear performance of the brake system [3], [5], [15] because

it is believed that the film promotes adhesive friction, where bonds are formed and broken between the brake pad and the film during the brake system conversion of kinetic to thermal energy [40].

Those who believe the adhesive mechanism is a factor in the friction film formation also believe that bedding of the brake friction couple needs to achieve and maintain, for sufficient duration, the *adhesive temperature* (typically 100 to 600 °F for *street pads*, and 600 to 1400 °F for *race pads*), or the temperature at which brake materials begin to create the friction film through the adhesive mechanism [40]. If the adhesive temperature is not achieved or maintained for sufficient duration, the friction will be primarily influenced by the abrasive mechanism causing the destruction of the friction film [40].

The purpose of the bedding procedure was to condition the brake friction couple to the maximum possible coefficient of friction to increase the brake rotor wear rate during wear simulation on the experimental apparatus. Unfortunately, a universal procedure to bed any pad compound with any rotor material does not exist. Brake pad manufacturers have created bedding procedures for their products; however, these procedures are not necessarily established on a firm scientific basis, most bedding procedures appear to consist of hand waving based on experience. Additionally, manufacture created bedding procedures are intended to be performed with the brake rotor and pads installed on a vehicle. Due to the difficulty in interpreting the generalized, vehicle-based specifications constituting these procedures, none of the manufacturer created bedding procedures could be easily adapted to condition the brake system using the experimental apparatus. Therefore, an attempt was made to establish a suitable bedding procedure scientifically using differential scanning calorimetry; however, the differential scanning calorimetry results did not present information particularly suited to forming a proper bedding procedure. As a result, an inertia brake dynamometer test standard established by SAE [43] was used as the basis for the bedding procedure employed for the current study.

2.2.1. Differential scanning calorimetry

Differential scanning calorimetry (DSC) is a thermal analysis process used to determine thermal transitions of materials, such as melting point and glass transition temperature of polymers (see Appendix A.1: Measurement principle).

Guipu, et al. [15] conducted a DSC temperature sweep to investigate the possible thermal transitions of a non-asbestos, low-metal brake pad friction material formed, in part, from a phenolic binding resin (10 % by weight). The DSC temperature sweep consisted of a single ramp from room temperature to 300 °C at a rate of +10 °C/min. Guipu, et al. observed the thermal decomposition of some of the organic ingredients (phenolic resin is a thermosetting organic polymer) in the friction material above 220 °C and believed that this thermal decomposition would deteriorate the size and mechanical properties of the lesser wear resistant pad constituents (resin binder, fillers, friction modifiers) which form a portion of the friction film. Guipu, et al. concluded that the thermal decomposition of the organic ingredients observed during the DSC temperature sweep was responsible for the high temperature wear of the brake pad friction material observed during inertia dynamometer testing (see Figure 2.3).

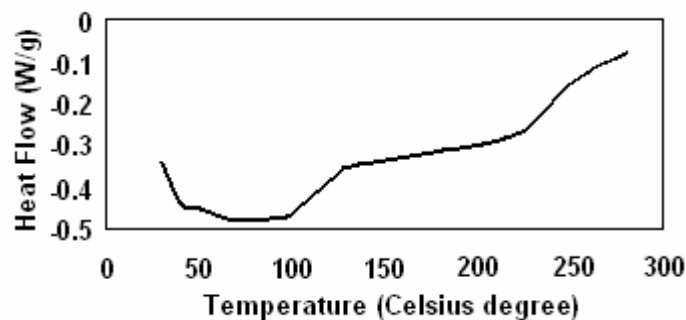


Figure 2.3: DSC plot of a low-metal brake pad friction material as measured by Guipu, et al. [15]

Ramousse, et al. [18] conducted a differential thermal analysis (DTA) and a thermogravimetric analysis (TGA) temperature sweep to investigate the chemical and physical processes occurring during elevated temperature exposure of a semi-metallic brake pad friction material formed, in part, from a phenolic binding resin. DTA is a similar thermal analysis process

to DSC, while TGA is a thermal analysis process used to determine the changes in mass of a material in response to changes in temperature. The DTA and TGA temperature sweep consisted of a ramp from room temperature to 1 000 °C at a rate of +2 °C/min, with a 1.0 hr hold at 1 000 °C, followed by a ramp from 1 000 °C to 25 °C a rate of -10 °C/min. Ramousse, et al. believed the thermal decomposition of the binding resin would appear as a mass loss, as measured by the TGA, accompanied by an exothermic peak, as measured by the DTA. Ramousse, et al. observed the partial thermal decomposition of the binding resin between 250 and 450 °C with a corresponding mass loss of 33 percent (see Figure 2.4). A summary of the full thermal behavior, as measured by the TGA, of the semi-metallic brake pad friction material investigated by Ramousse, et al. is shown in Figure 2.5.

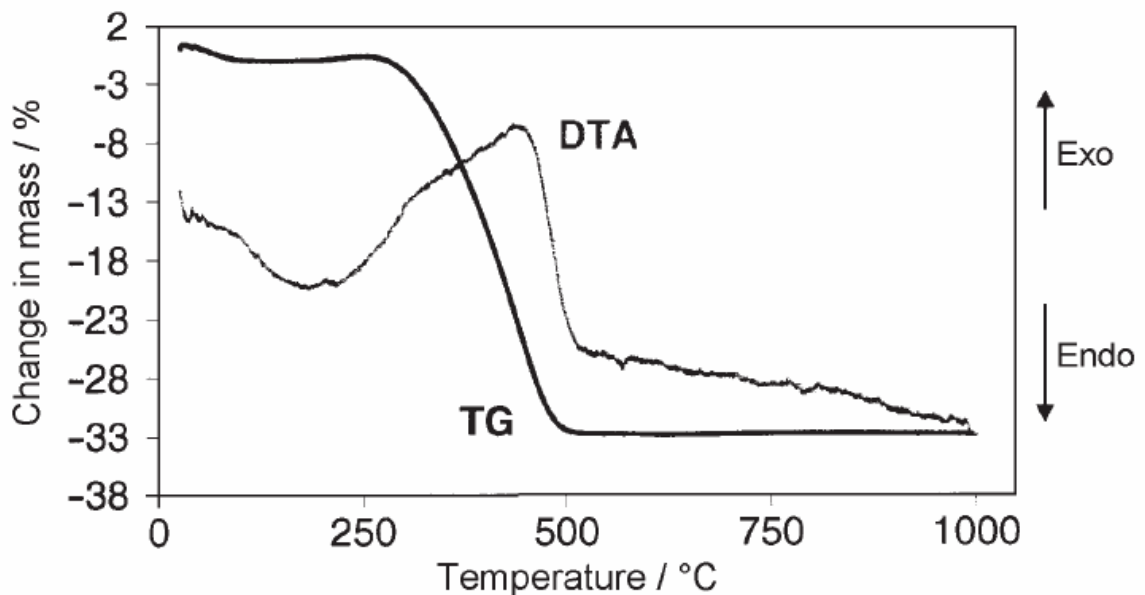


Figure 2.4: DTA and TGA plots of the phenolic binding resin found in a semi-metallic brake pad friction material as measured by Ramousse, et al. [18]

2.2.1.1. Test objective

Based upon the work of Guipu, et al. [15] and Ramousse, et al. [18], it was believed that exposure to a DSC temperature sweep would cause a measurable thermal transition in a fresh sample of brake pad friction material used in the current study due to the thermal decomposition

of the binding resin. As previously mentioned (see Section 2.2: Bedding procedure development), one of the three purposes of the bedding process is to cook the binding resin from the pad friction surface, which would occur if the brake pads were exposed to a temperature greater than or equal to that necessary to cause the thermal decomposition of the binding resin. It was intended to create a bedding procedure to ensure the pads were exposed to such a temperature to help condition them to the maximum possible coefficient of friction by removing the friction-reducing resin at the friction surface to increase the brake rotor wear rate during wear simulation on the experimental apparatus.

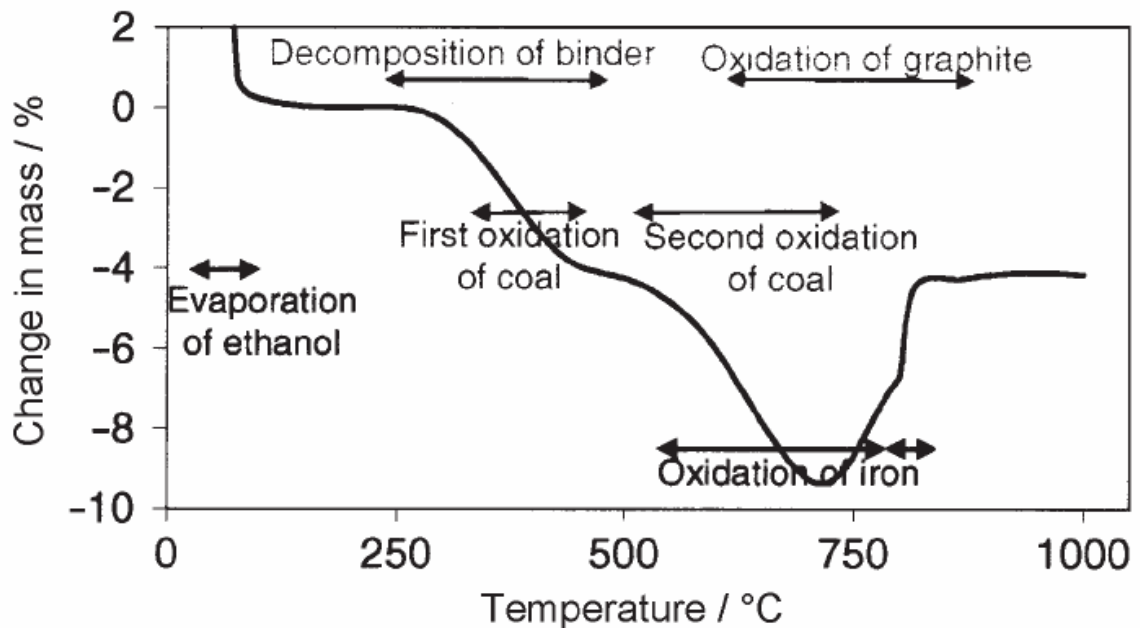


Figure 2.5: TGA plot of the semi-metallic brake pad friction material as measured by Ramousse, et al. [18]

Therefore, several DSC tests were conducted during the current study on various fresh and used (for comparison) samples of the brake pad friction material employing a differential scanning calorimeter produced by Seiko Instruments Inc. (model no.: DSC220C; see Figure 2.6). The specifications of the DSC220C are [42]:

- *Temperature range:* -150 to 725 °C
- *Heating rate range:* 0.01 to 100 °C/min

- *Cooling limit:* -100 °C at a rate of 10 °C/min



Figure 2.6: Seiko Instruments Inc. DSC220C differential scanning calorimeter

2.2.1.2. Test procedure

Two sets of tests were conducted using the DSC220C. The first test applied a single temperature ramp to a single set of new and used brake pad friction material samples. The temperature ramp was re-applied to the new sample an additional two times. The second test applied two consecutive temperature cycles to a different single set of new and used brake pad friction material samples. All samples were prepared by removing suitable amounts of material from Wilwood PolyMatrix A brake pads using a non-oiled, laboratory razor blade and measured using a Scientech laboratory scale set to a 100 g capacity and a 0.1 mg readability (model no.: SA 210D). Using a Seiko Instruments sample sealer, all samples were sealed in 5 mm diameter Seiko aluminum open sample pans and crimping covers to prevent leakage and loss of sample materials as evaporation and expansion occurs during measurement. The details of the first differential scanning calorimetry test were (see Figure 2.7):

- Starting temperature: 30 °C
- Finishing temperature: 500 °C
- Hold time at finishing temperature: 5 min
- Temperature rate: 20 °C/min
- Mass of 'new' sample: 16.8 mg
- Mass of 'used' sample: 17.2 mg

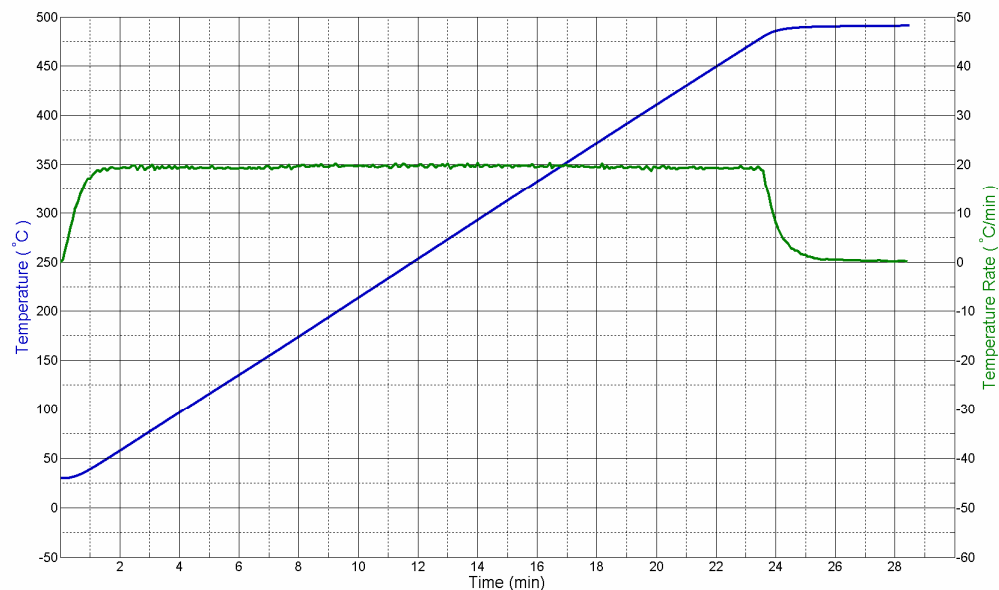


Figure 2.7: Temperature detail for first DSC test

The details of the second differential scanning calorimetry test were (see Table 2.2 and Figure 2.8):

- Mass of 'new' sample: 26.5 mg
- Mass of 'used' sample: 27.3 mg

Table 2.2: Temperature cycle detail for second DSC test

Cycle Number	1	2	3	4
Starting temperature (°C)	-30	500	-30	500
Finishing temperature (°C)	500	-30	500	40
Hold time (min)	5	1	5	0
Temperature Rate (°C/min)	20	-20	20	-40

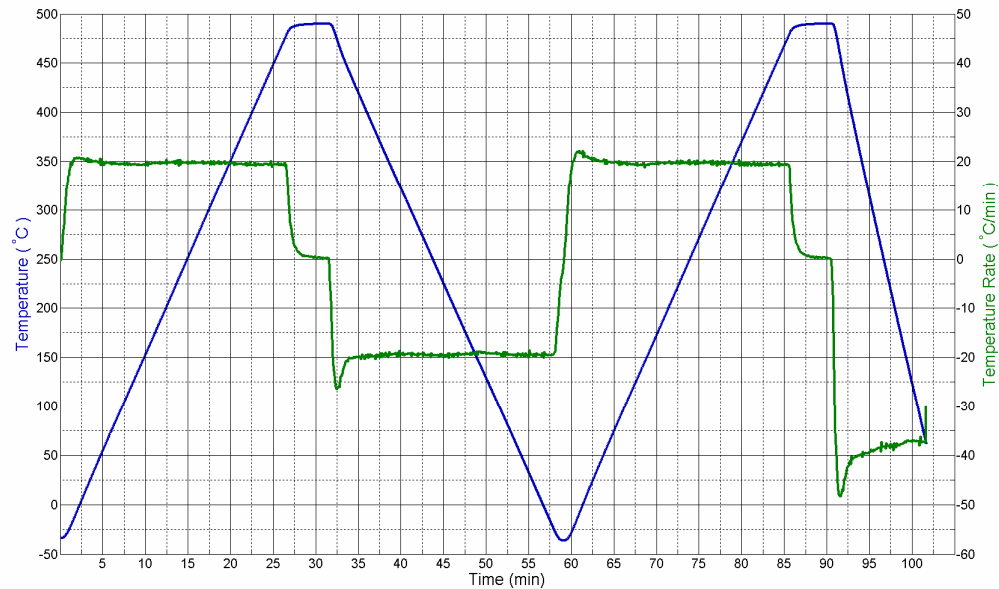


Figure 2.8: Temperature detail for second DSC test

2.2.1.3. Test results

The differential scanning calorimetry results did not provide enough information to establish a suitable bedding procedure, in fact, no significant thermal transitions were observed for either new or used brake pad friction material samples for either test set. Thermal transitions would appear in a plot of the differential scanning calorimetry output (heat flow) as a slope change, therefore they would also appear in a plot of the derivative of the output as *spikes*. No spikes were observed in the differential scanning calorimetry test results except when the DSC220C was approaching or leaving a temperature set point (see Figure 2.9; see Appendix A.2: Test results, for complete DSC test results).

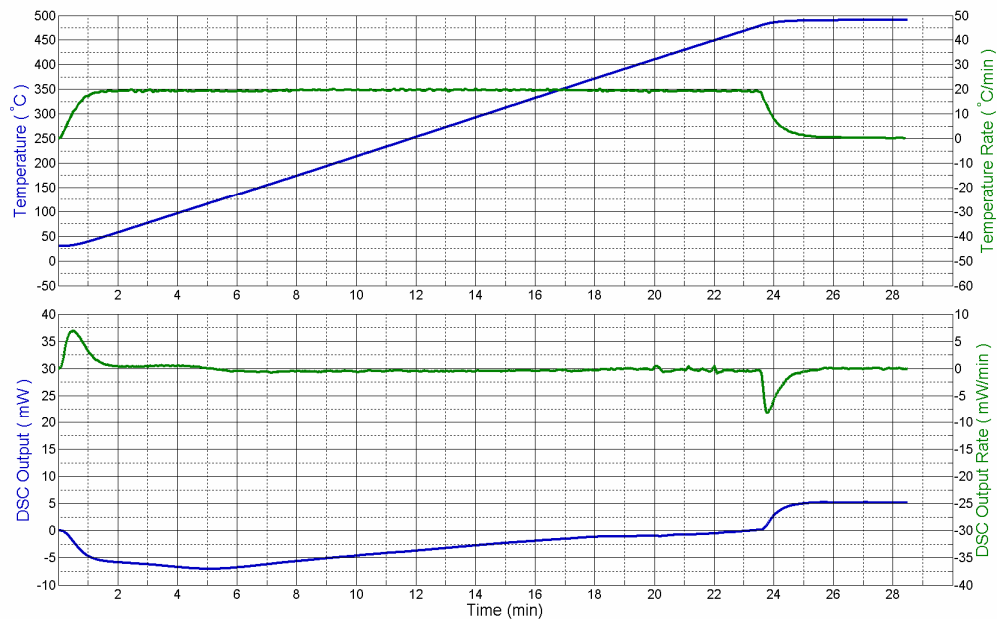


Figure 2.9: DSC test results from the first test set for the first temperature exposure of the *new* compound sample

2.2.2. SAE J2522 standard

Since a suitable brake pad bedding procedure could not be established from the differential scanning calorimetry tests, efforts shifted to investigating industry standards, in particular, those published by SAE. Several SAE standards exist relating to brake systems, but eventually standard, *SAE J2522: Dynamometer Global Brake Effectiveness* [43], was selected due to its availability and incorporation of a universal bedding procedure.

The purpose of *SAE J2522* was to define a procedure for which comparisons between brake friction materials used on motor vehicles can be established using an inertia brake dynamometer. Several portions comprise *SAE J2522* including burnish (bedding), speed and pressure sensitivity, cold application, motorway application, fade, recovery, and temperature and pressure sensitivity sections. Specifically, the burnish, or bedding, portion consists of three sections: green mu characteristic, burnish, and characteristic value. Each bedding section consists of discrete brake applications, or *snubs*, at specific brake pressures intended to decelerate the brake rotor from an initial to a final rotational velocity. Each snub is initiated only

after the rotor has cooled down below the initial temperature value. *SAE J2522* requires the use of inertia during testing equivalent to 75 percent of the gross vehicle weight. An overview of the test parameters for each of the burnish sections is given below (see Appendix B.1: *SAE J2522*):

- *Green Mu Characteristic*: 30 snubs from 80 to 30 kph at 3 000 kPa
- *Burnish*: 192 snubs (or optional 64 snubs) from 80 to 30 kph at varying brake pressures
- *Characteristic value*: 6 snubs from 80 to 30 kph at 3 000 kPa

These three portions were the basis for creating a suitable brake pad bedding procedure for the current study; however, since *SAE J2522* required the use of inertia to perform any testing, a method of simulating the appropriate amount of inertia was required. Ultimately, a plan was put into place to implement inertia on the experimental apparatus which resulted in the need to scale the *SAE J2522* test parameters for specific vehicle applications.

2.3. Wear procedure development

The purpose of the wear procedure was to provide a repeatable method to test brake rotors and pads to study wear mechanisms and rates. The wear procedure was based upon two specific industry standards, one published by ASTM International and the other by the Society of Automotive Engineers (SAE).

2.3.1. ASTM G99-05 standard

Several test specifications were adopted for use in the wear procedure from the ASTM International standard, *G99-05: Standard Test Method for Wear Testing with a Pin-on-Disk Apparatus* [28] (see Section 1.2.3: Testing and measurement). The pin-on-disk apparatus is representative of a very simplified brake dynamometer, where the pin is representative of the brake pads, while the disk is representative of the brake rotor. As such, the need to specify values for load, speed, sliding distance and temperature (the specification of the atmosphere parameter was not considered) was adopted for use in the wear procedure in order to be implemented on the experimental apparatus. Additionally, the wear procedure was structured

such that the load test parameter would be varied across test specimen sets, while speed and sliding distance parameters would be held constant.

The exact specifications described in *ASTM G99-05* for wear testing were not fully adopted for use in the wear procedure due to concerns over controlling brake system temperatures at reasonable levels while still generating measurable rotor mass loss during continuous brake application. Additionally, disk specimen diameters are specified in *ASTM G99-05* to range between 30 to 100 mm, while the sensitivity specification for wear measuring systems is 0.1 mg or better for any balance used to measure the mass loss of a specimen. Since the brake disk diameter used for this study measured approximately 228.6 mm, its mass would be considerably greater than the disk specimens specified in *ASTM G99-05*. Thus, the sensitivity specification for wear measuring systems would be extremely difficult to obtain considering scales with large mass capacities and small mass resolutions are extremely expensive and rare.

2.3.2. SAE J2522 standard

The SAE standard, *J2522: Dynamometer Global Brake Effectiveness* [43], had already been used to determine a suitable bedding procedure. Since *SAE J2522* is based on the use of snubs and since a plan to implement inertia on the experimental apparatus was in place, using the general test section layout from *SAE J2522* allowed a straightforward wear procedure to be created that incorporated the several test specifications adopted from *ASTM G99-05*.

The wear procedure was structured to apply a finite number of *wear snubs* at a consistent brake pressure for a given rotor rotational velocity. Each wear snub would be applied when the rotor surface temperature fell below a given initial value and would be removed once the rotor surface temperature increase reached the value specified by the energy equivalent inertia simulation.

3. EXPERIMENTAL APPARATUS DEVELOPMENT

3.1. Objectives

An experimental apparatus was developed to implement both procedures of the wear simulation. As such, it was necessary for the experimental apparatus to control and monitor the functionality of several systems including temperature, pressure, drive, power, measurement and control, and safety.

3.2. Layout overview

In its basic configuration the experimental apparatus consisted of an electric motor supplying torque to the brake rotor through a clutch and power transmission, two electric linear actuators coupled to separate hydraulic systems controlling the clutch and brake caliper, an environmental chamber housing the brake system, and various power supplies, a computer, data acquisition unit and various sensors to power, control and monitor each system. The frame of the experimental apparatus was constructed from extruded aluminum and hardware manufactured by 80/20, Inc., and built prior to the current study by others. All components of the experimental apparatus were located in a single test cell with an adjoining control room where the operation of the experimental apparatus could be observed.

3.3. Temperature system

Thermocouples monitor the temperature of several components on the experimental apparatus and an exhaust system draws in fresh air through the environmental chamber to help regulate the temperature of the brake system components housed within (see Figure 3.1).

Thermocouples monitor the temperature at eight different locations within the power transmission and brake system of the experimental apparatus: the four pillow block bearings, the two brake pads, one of the caliper mount bushings, and the brake rotor surface.



Figure 3.1: Environmental chamber exhaust system as-installed in the experimental apparatus

The four pillow block bearings and the caliper mount bushing temperatures were measured using Omega Engineering, Inc. grounded, K-type (chromel-alumel), six in. long, $\frac{1}{8}$ in. diameter, 304 stainless steel thermocouple probes with quick disconnect miniature connectors (model no.: KMQSS-125G-6; see Figure 3.2). Each thermocouple probe was installed using a brass, $\frac{1}{8}$ in. compression, tube to $\frac{1}{8}$ in. NPT male, adapter (see Figure 4.6).

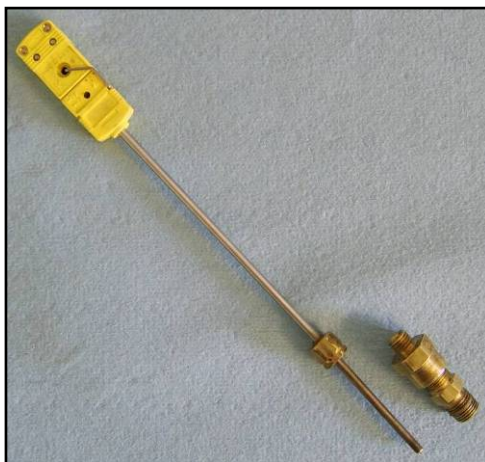


Figure 3.2: Omega K-type thermocouple probe shown with brass adapter

The two brake pad temperatures were measured using k-type thermocouples constructed from bulk thermocouple wire with quick disconnect miniature connectors and welded in-house.

The brake rotor surface temperature was measured using an Exergen non-contact, infrared thermocouple (model no.: IRTc.3x; see Figure 3.3). The non-contact thermocouple was positioned $\frac{1}{2}$ in. above the rotor surface at the approximate location of the rotor effective radius and measured the surface temperature at the *nine o'clock* position, where the caliper was positioned at the *three o'clock* position; however, the IRTc.3x model was only suitable for measuring non-metal surfaces, therefore a calibration was required to accurately measure the brake rotor surface temperature.

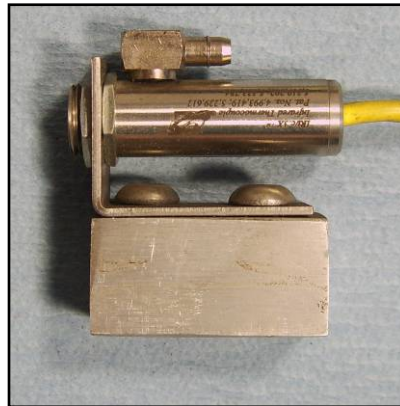


Figure 3.3: Exergen IRTc.3x non-contact, infrared thermocouple and mount

3.3.1. Exergen non-contact, infrared thermocouple calibration

To calibrate the output from the Exergen IRTc.3x non-contact, infrared thermocouple to the correct temperature, a steel rotor was heated in an oven between 600 and 700 °F and held at this temperature for 30 min. The rotor was removed from the oven and simultaneously measured with the Exergen IRTc.3x and a k-type thermocouple while cooling down. A third-order polynomial was fitted to the data, using the temperature from the k-type thermocouple as the dependent variable, and using the temperature from the IRTc.3x as the independent variable. The resulting third-order polynomial calibration equation, in °F, was (see Figure 3.4):

$$T_{cal} = (2.531 \times 10^{-7}) T_{IRTc}^3 + (-6.365 \times 10^{-4}) T_{IRTc}^2 + (0.812) T_{IRTc} + (12.655) \quad (3.3)$$

Equation 3.3 was used to convert the temperature measurement produced from the Exergen IRTc.3x to the actual temperature of the brake rotor surface as it would be measured using a k-type thermocouple in contact with the rotor surface (see Figure 3.5).

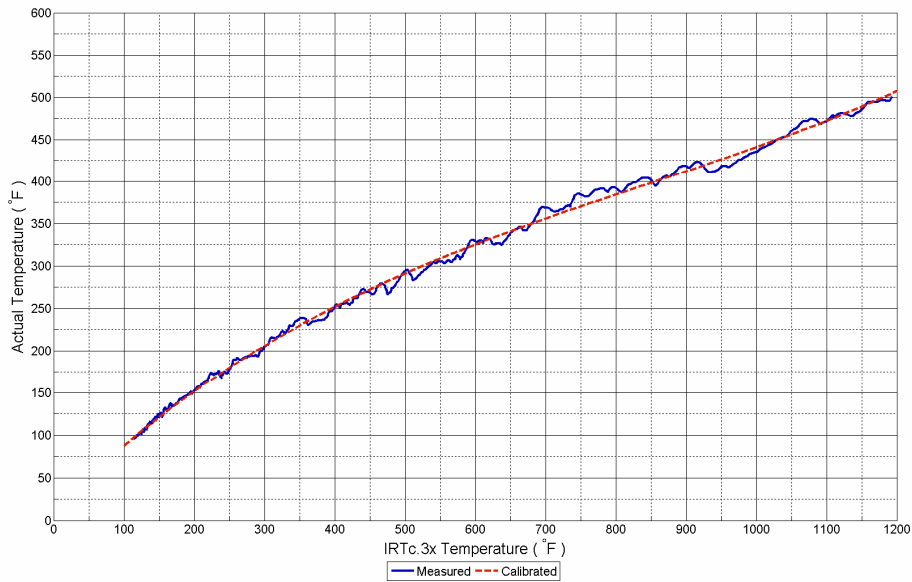


Figure 3.4: Third-order calibration polynomial fitted to the measured rotor surface temperature data

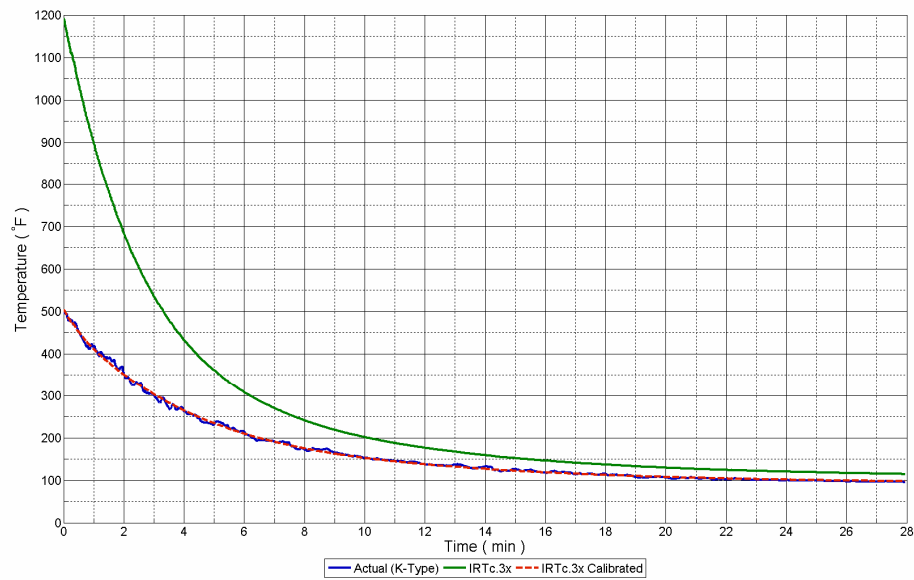


Figure 3.5: Rotor surface temperature as measured by a k-type thermocouple, Exergen IRTc.3x (raw), and Exergen IRTc.3x (as-calibrated)

3.4. Pressure system

The purpose of the pressure system was to generate and transfer pressure to the brake system, based upon the use of a hydraulic system using incompressible fluid as the powering medium, to force the brake pads to contact the brake rotor. The pressure system consisted of an electric linear actuator, master cylinder, hydraulic system and pressure transducer. Pressure in the hydraulic system was generated by the electric linear actuator coupled to the master cylinder and monitored by the pressure transducer installed in the plumbing.

3.4.1. Hydraulic system

The purpose of the hydraulic system was to transfer pressure to the brake system and consisted of the required plumbing to connect the master cylinder and brake caliper (see Figure 3.6). The hydraulic pressure generated at the master cylinder from electric linear actuator was transferred to the brake system where it would extend the brake caliper pistons and force the brake pads against the brake rotor. The hydraulic pressure was transferred through the plumbing using ATE Super Blue Racing brake fluid with the following specifications:

- DOT designation 4 automotive brake fluid
- Dry boiling point: 280 °C
- Wet boiling point: 202 °C

ATE Super Blue Racing brake fluid, like all DOT 4 fluids, is polyethylene glycol-based and therefore hygroscopic. Hygroscopic fluids have the ability to absorb water and as such, DOT requires a wet boiling point rating defined as the boiling point of a brake fluid containing 3.7 percent water by volume.

Hydraulic plumbing consisted of three flexible lines and various steel fittings. Two of the hydraulic lines were manufactured by Earl's Performance Plumbing and constructed using a tightly braided stainless steel sheath surrounding an extruded Teflon™ tube with dash three female AN steel hose fittings of lengths 26 inch and 36 inch (part nos.: 63010126ERL and 63010136ERL, respectively). The third hydraulic line was custom built by Tubes 'N hoses of Loveland, Colorado, and served two purposes. The first purpose was to adapt the $\frac{1}{8}$ in. NPT

port on the tee fitting to the 1/4 in. NPT port on the pressure transducer. The second purpose was to electrically isolate the body of the pressure transducer from the frame of experimental apparatus by using a small length of rubber hose. Various steel fittings connected the hydraulic lines to the master cylinder, pressure transducer and brake caliper. The various steel fittings were all manufactured by Earl's Performance Plumbing and included:

- Dash three AN male to dash three AN male coupler fitting (part no.: 961503ERL)
- Dash three AN male to 1/8 in. NPT male tee fitting (part no.: 962603ERL)
- Dash three AN male to 10 mm banjo fitting (part no.: 9978031ERL)
- 3/8 in. - 24 banjo bolt with washer gaskets (part no.: 977503ERL)

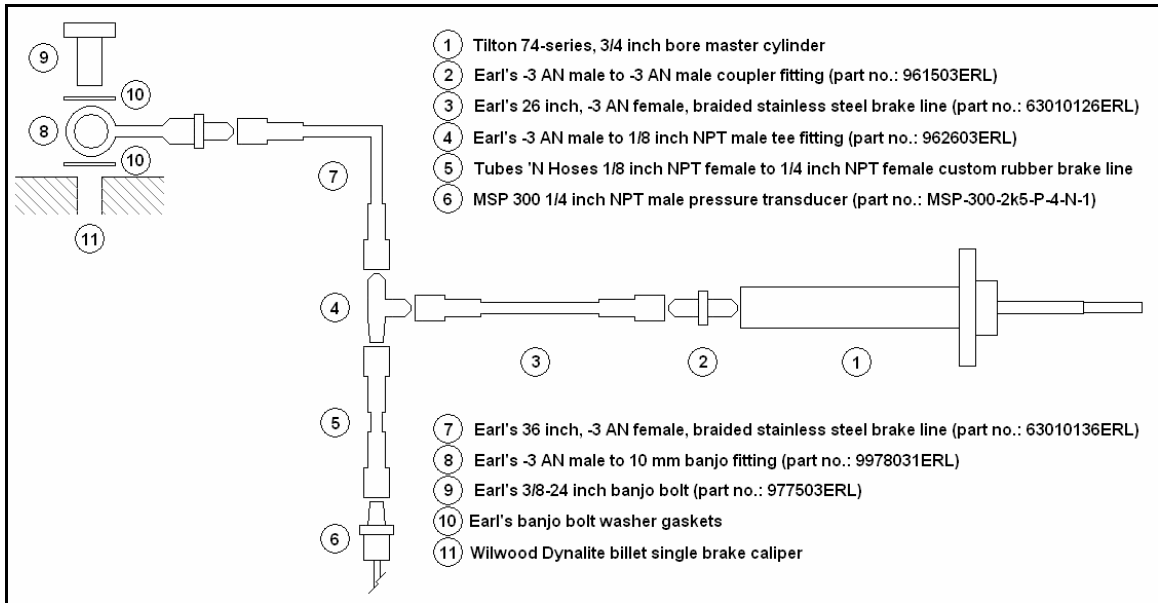


Figure 3.6: Hydraulic system schematic

3.4.2. Electric linear actuator and master cylinder

The purpose of the electric linear actuator and master cylinder was to generate pressure in the hydraulic system and consisted of a Haydon Series 87000 Size 34 hybrid electric linear actuator (part no.: 87H43-2.85-925ENG) coupled to a Tilton Engineering 74-series master cylinder with a 3/4 in. bore and a remote large reservoir (part no.: 74-750U) (see Figure 3.7). The

Haydon hybrid electric linear actuator was chosen because it incorporates a stepper motor to provide the linear driving force. This stepper motor is capable of precise, repeatable control over the stroke of the actuator and thus, the brake pressure. The specifications of the Haydon hybrid electric linear actuator were:

- *Force capability:* 500 lb_f
- *Stroke:* 2.50 in.
- *Motor style:* stepper
- *Motor resolution:* 0.0005 in/step (dividable through microstep setting on driver)

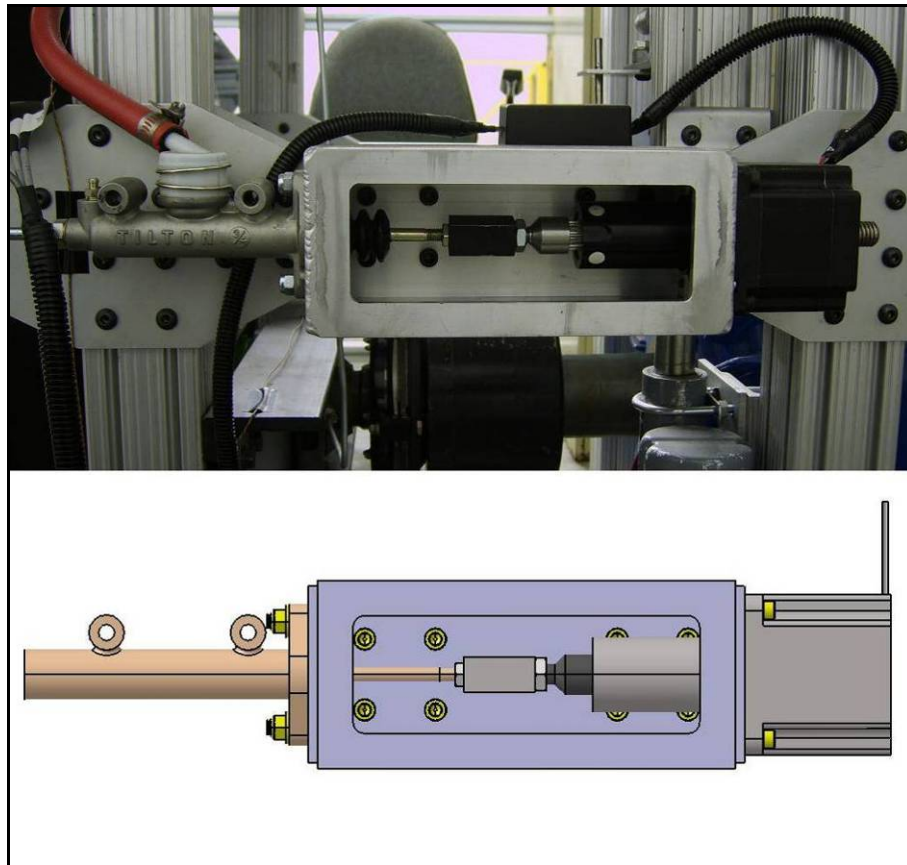


Figure 3.7: Linear actuator coupled to Tilton master cylinder as-installed (top) and as-designed (bottom)

The Haydon 87000 hybrid linear actuator was driven using a Haydon DCM8055 high performance microstepping chopping driver with the following specifications (see Figure 3.8):

- *Maximum supply voltage: +80 VDC*
- *Maximum supply current: 5.5 A*
- *Microstep resolution: 2, 4, 8, 16, 32, 64, 128 or 256*
- *Microstep resolution (alternate): 5, 10, 25, 50, 125, 250*

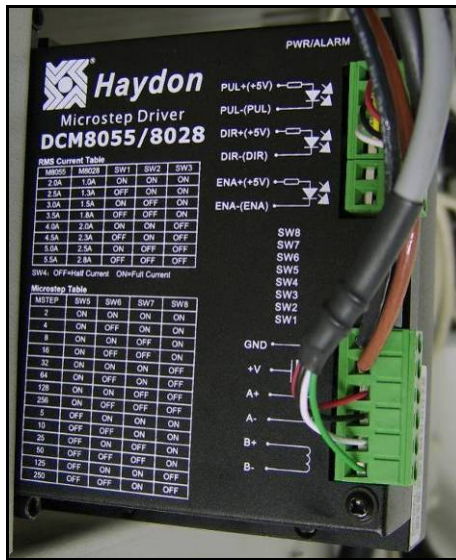


Figure 3.8: Haydon DCM8055 high performance microstepping chopping driver as-installed in the experimental apparatus

The Haydon DCM8055 microstepping chopping driver was powered by a programmable, direct current power supply system. Channels 3, 4, and 5 containing 20 V, 10 A power modules were wired in series and programmed to supply the Haydon DCM8055 chopping driver with 60 V with a current limit of 10 A.

The Haydon microstepping chopping driver was controlled through the use of a National Instruments data acquisition card and I/O connector block using TTL signal outputs to send direction and pulse information to the Haydon DCM8055 chopping driver (see Figure 3.9).

The electric linear actuator and master cylinder were attached to the experimental apparatus using a single, 4 in. by 4 in. by 1/4 in. aluminum square tube with two, 1/4 in. aluminum plates machined and welded to the ends and eight, 5/16 in. – 18 thread, 5/8 in. length socket head cap screws. The electric linear actuator and master cylinder were mounted to the end plates

using four, $\frac{1}{4}$ in. – 20 thread, $\frac{3}{4}$ in. length and two, $\frac{5}{16}$ in. – 24 thread, 1 $\frac{1}{4}$ in. length socket head cap screws, respectively. A steel, square coupling nut was machined to join the electric linear actuator and master cylinder with a $\frac{7}{16}$ in. – 14 thread and a $\frac{5}{16}$ in. – 24 thread jam nuts (see Appendix E.1: Brake actuator mount, for design drawing; see Appendix F.1: Brake actuator mount, for exploded view of assembly).

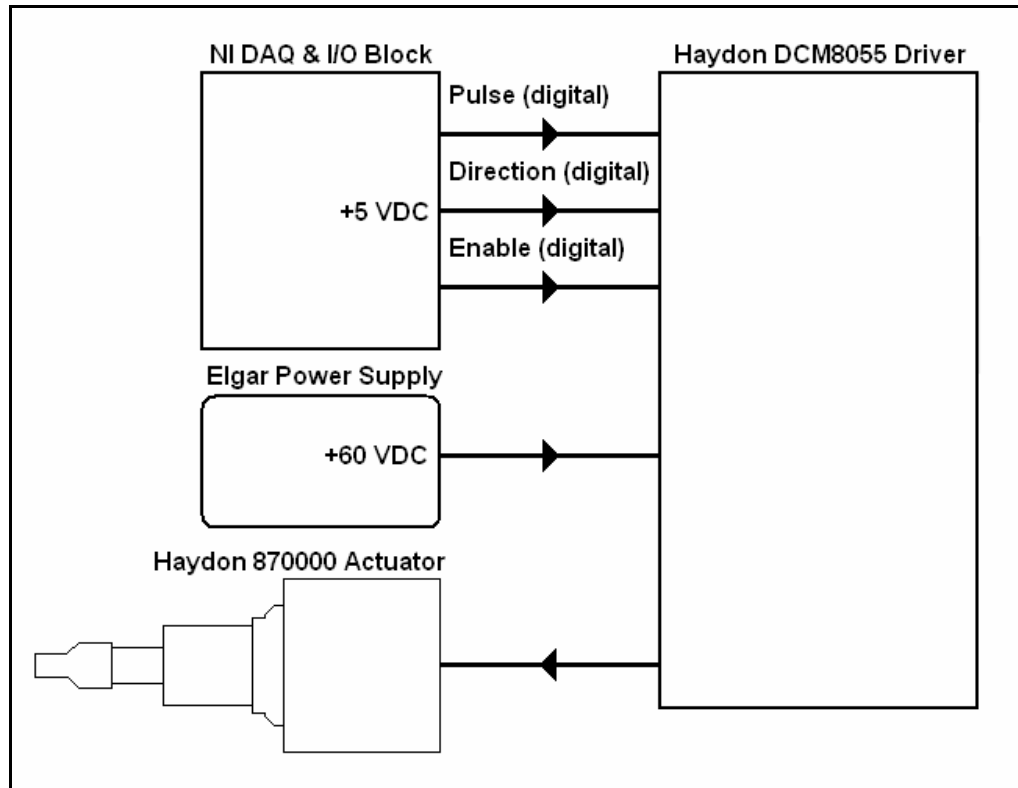


Figure 3.9: Schematic of electric linear actuator, driver, power supply, and controller

3.4.3. Pressure transducer

Pressure in the hydraulic system was measured by a MSI Sensors MSP 300 stainless steel isolated pressure transducer (model no.: MSP-300-2K5-P-4-N-1) with the following specifications (see Figure 3.10):

- *Pressure range:* 0 to 2500 psi (gauge)
- *Pressure port:* $\frac{1}{4}$ in. NPT

- *Electrical output:* 1.0 to 5.0 VDC fixed, single ended analog, amplified, 3 wire
- *Electrical connection:* 2 ft. cable
- *Power Supply:* 10 to 30 VDC



Figure 3.10: MSP 300 pressure transducer as-installed in the experimental apparatus

The MSP 300 pressure transducer was installed in the hydraulic plumbing using a steel, male tee fitting configured with a single, $\frac{1}{8}$ in. NPT port and two, dash 3 AN ports manufactured by Earl's Performance Plumbing (part no.: 962603ERL). A hydraulic line, custom built by Tubes 'N Hoses of Loveland, Colorado, connected the $\frac{1}{8}$ in. NPT port of the tee fitting to the $\frac{1}{4}$ in. NPT port of the pressure transducer. In addition, to reduce signal noise, the custom hydraulic line served to electrically isolate the body of the pressure transducer from the frame of experimental apparatus through the use of a small length of rubber brake hose (see Figure 3.11).

3.5. Drive system

The purpose of the drive system was to provide torque to the brake system to power the brake rotor to a particular rotational velocity. The drive system consisted of an electric motor, a clutch system, a power transmission and a shaft encoder. Torque generated from the electric motor is transmitted through the clutch system and power transmission to reach the brake system; the shaft encoder measures the rotational velocity of the brake rotor (see Figure 3.12).



Figure 3.11: Tubes 'N Hoses custom rubber hydraulic line

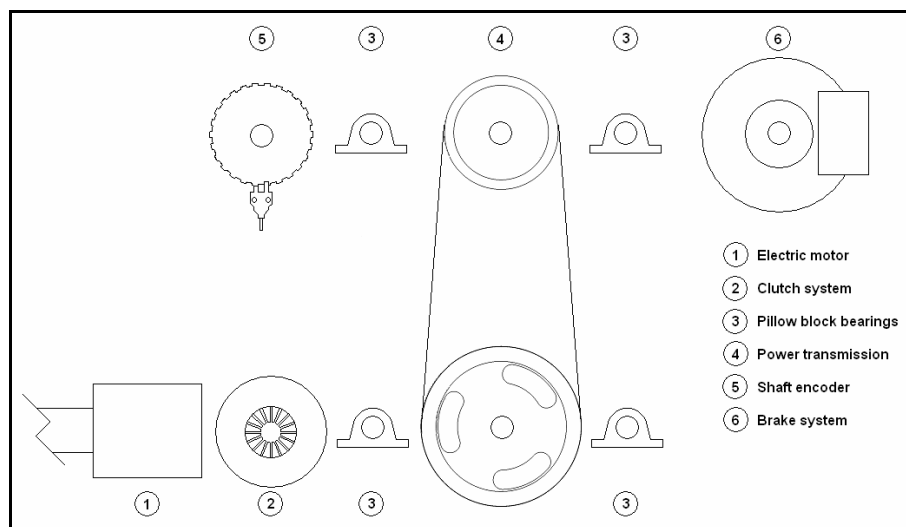


Figure 3.12: Drive system schematic

3.5.1. Electric motor

Torque was produced from a three phase, alternating current, induction motor manufactured by Toshiba Corporation (model no.: B1006YLF4A0) with the following specifications (see Figure 3.13):

- *Voltage:* 230/460 VAC
- *Current:* 240/120 A
- *Frequency:* 60 Hz
- *Rotational speed:* 1175 rpm
- *Power:* 100 hp

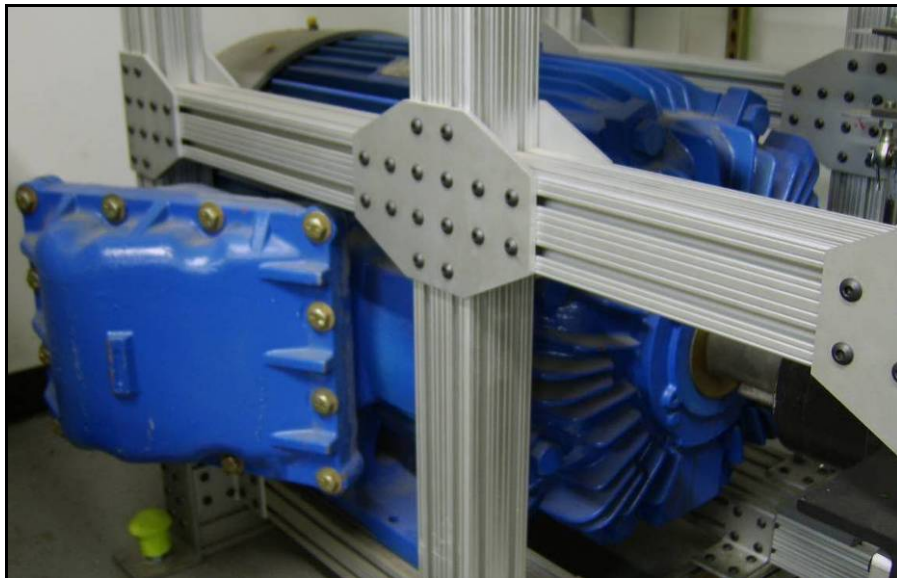


Figure 3.13: Toshiba Corporation electric, 3 phase induction motor as-installed in the experimental apparatus

The rotational speed of the electric motor was controlled by adjusting the frequency of the electrical power supplied to it through the use of a VFD manufactured by Cutler-Hammer (model no.: SV9125AN-5M0A00; see Figure 3.14).



Figure 3.14: Cutler-Hammer VFD as-installed in the experimental apparatus

3.5.2. Clutch system

The purpose of the clutch system was not only to transmit the electric motor torque, but to interrupt it when necessary by physically disconnecting the electric motor from the brake system. The clutch system consisted of (see Figure 3.15):

- Flywheel (unknown make and model)
- Tilton Engineering OT-II 7.25 in., 2 plate, sintered metallic racing clutch and pressure plate (part no.: 66-002UORA)
- Tilton Engineering hydraulic, self-centering release bearing with 44 mm contact diameter (part no.: 61-402)
- Tilton Engineering 74-series master cylinder with a $\frac{3}{4}$ in. bore and a remote large reservoir (part no.: 74-750U)
- Duff-Norton 12 VDC, 4 in. stroke electromechanical linear actuator with limit switches (part no.: LSPD2775-4)

- Hydraulic plumbing consisting of a $\frac{3}{8}$ in. – 24 SAE inverted flare male, steel hard line with required coupler fittings

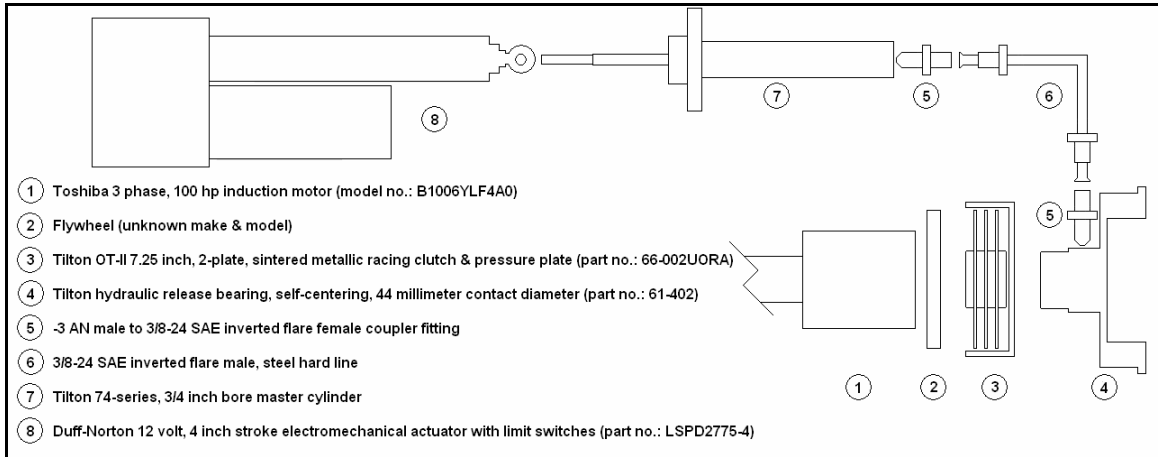


Figure 3.15: Clutch system schematic

Pressure in the hydraulic system was generated by the electromechanical linear actuator coupled to the master cylinder and used to force the hydraulic release bearing against the pressure plate to pull the clutch disk out of contact with the flywheel, thus *disengaging* the clutch. Once hydraulic pressure was removed, the pressure plate would force the clutch back into contact with the flywheel, thus *engaging* the clutch, and allow the electric motor torque to reach the brake system.

3.5.3. Power transmission

The purpose of the power transmission was not only to transmit the electric motor torque, but to provide a rotational velocity increase to the brake system at the cost of a torque reduction.

The power transmission consisted of (see Figure 3.17):

- Gates PowerGrip® GT®2 14 mm pitch, 80 tooth drive sprocket (part no.: P80-14MGT-85)
- Gates PowerGrip® GT®2 14 mm pitch, 56 tooth driven sprocket (part no.: P56-14MGT-85)

- Gates PowerGrip® GT®2 14 mm pitch, belt (part no.: 2310-14MGT-40)
- INA pillow block bearings for 2.0 in. shaft diameter (part no.: RAKY2)
- Upper and lower 2.0 in. steel shafts of 28 in. and 20 in. lengths, respectively and various features (keyways, threaded ends, etc.)

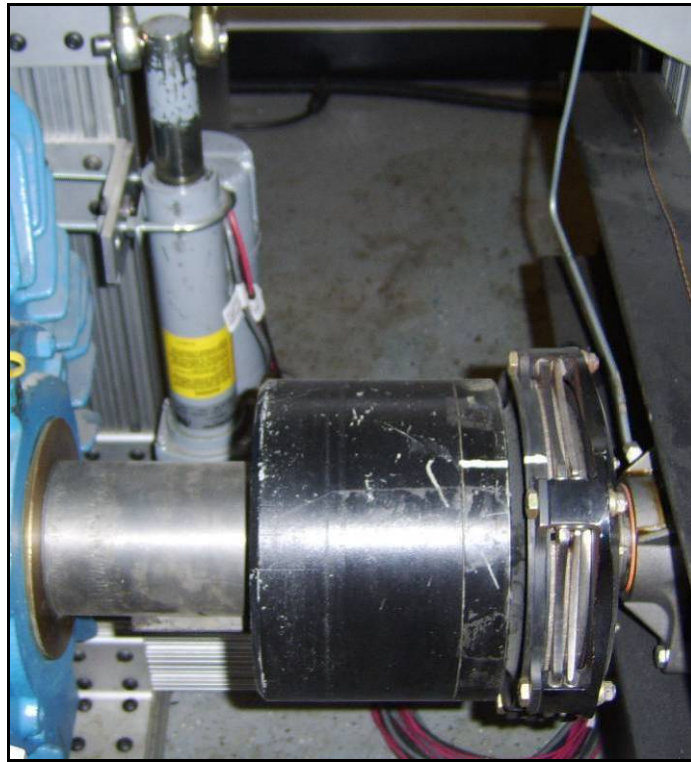


Figure 3.16: Clutch system showing flywheel, clutch, pressure plate, hydraulic release bearing, hydraulic plumbing, and electromechanical linear actuator

The drive and driven sprocket combination resulted in a rotational velocity increase, or power transmission ratio, of $^{80}/_{56}$ (1.4286). If the electric motor was operating at its rated rotational velocity of 1175 rpm, the power transmission ratio would result in the brake rotor spinning at approximately 1678 rpm. The power transmission ratio allowed for the following various vehicle speeds to be reproduced in the brake system:

- Chevrolet Corvette Z06 sports car: 133.2 mph
- Ford F150 Super Crew truck: 160.2 mph
- Generic lightweight, single seat, open wheel racecar: 99.9 mph

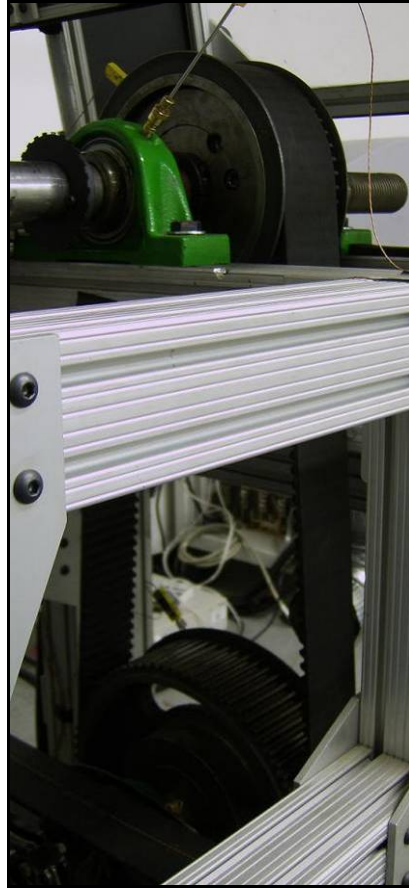


Figure 3.17: Power Transmission as-installed in the experimental apparatus

The Gates PowerGrip® GT®2 belt running between the drive and driven sprockets had a specification range for static tension during installation. Concerns existed that excessive center-to-center distance of the sprockets had resulted in excessive static tension in the belt. Mr. Terry Jensen of Colorado State University Facilities donated time and the use of a Gates Sonic Tension Meter to determine the belt static tension. The Gates Sonic Tension Meter measures the *plucked* frequency of the belt and correlates the measurement back to the belt static tension. It was determined that the Gates belt had an eleven percent higher static tension value than the maximum value of the specification range. Although the belt was measured to be installed excessively *tight*, Mr. Jensen advised that in his experience he routinely installs Gates PowerGrip® GT®2 belts excessively tight and still expects the belt to run continuously for at least six years with no problems. Since the scope of the experimental apparatus was to run for very

much less than six years continuously, no adjustments were carried out to lower the belt static tension within the specification range due to the difficulty in adjusting the center-to-center distance of the two sprockets.

Concerns existed over the type and amount of grease contained within the INA pillow block bearings. It was believed that an excessive amount of an incompatible grease formulation was introduced into the bearings which might potentially lead to catastrophic bearing failure due to temperature build up. The only realistic way to deal with incompatible grease was to replace the entire bearing. Since all four pillow block bearings were already installed in the experimental apparatus, replacing them would have required disassembly of the entire drive system. Thus, it was decided to forgo replacement and instead monitor the bearing temperatures of all four pillow blocks using thermocouple probes to ensure excessive temperatures, an indication that bearing failure is imminent, were not reached (see Section 3.3: Temperature system).

3.5.4. Shaft encoder

The purpose of the shaft encoder was to measure the rotational velocity of the brake rotor. The shaft encoder consisted of (see Figure 3.18; see Appendix F.2: Shaft encoder mount, for exploded view of assembly):

- Omron photomicrosensor with NPN output configuration (part no.: EE-SX770)
- Toothed wheel with 26 teeth (optional 52-toothed wheel also available)

The Omron SX770 photomicrosensor is an optical sensor based upon the transmission of an optical beam to detect objects through the use of an emitter (light emitting diode) and collector (phototransistor). The collector can detect when an object has interrupted the optical beam because of the reduced transmitted optical energy. [48] This principle was utilized to construct a shaft encoder using the Omron SX770 photomicrosensor and a toothed wheel.

The Omron SX770 photomicrosensor used a transistor with NPN configuration to output a signal. Difficulties were encountered when attempting to measure the NPN configured output signal. This difficulty was overcome when a 4.7 k Ω resistor was installed between the power and output terminals of the SX770 (see Figure 3.19).

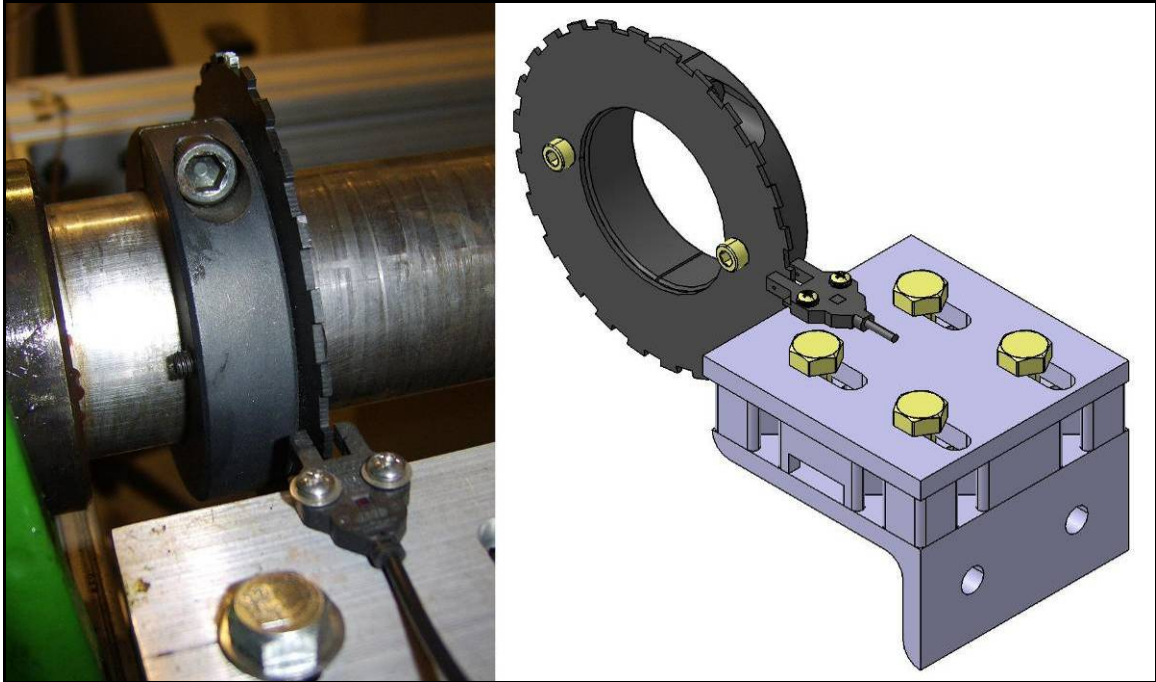


Figure 3.18: Shaft encoder with 26-toothed wheel as-installed (left) and as-designed (right)

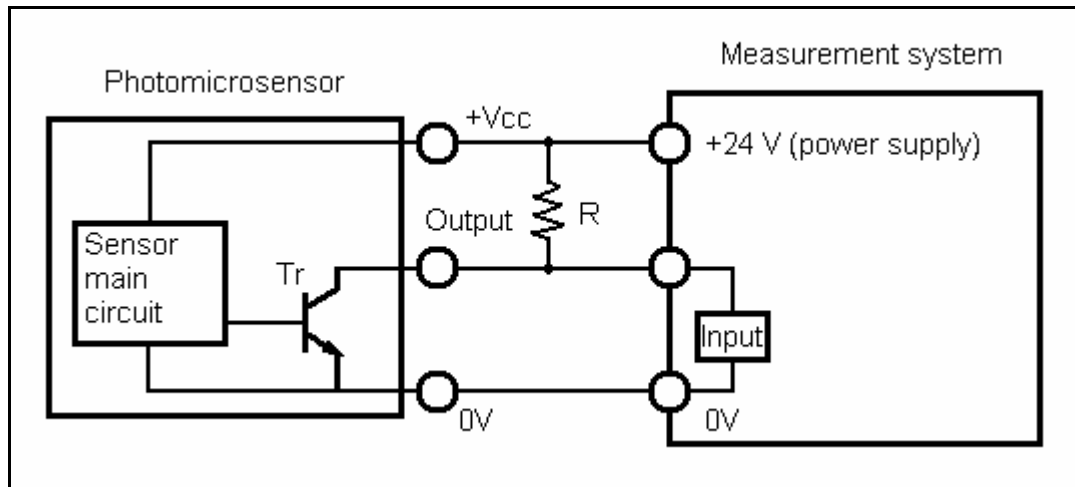


Figure 3.19: Circuit diagram of Omron SX770 photomicrosensor and measurement system showing placement of necessary resistor (R) to successfully measure output

Once the 4.7 k Ω resistor was installed between the power and output terminals of the SX770, it would output a *high* state (5 VDC) when the optical beam was transmitted and would output a *low* state (0 VDC) when the optical beam was interrupted forming a TTL based digital signal. The toothed wheel allowed the state of the SX770 to switch between high and low states

multiple times per revolution of the brake rotor. By measuring the frequency of the TTL digital signal produced from the SX770 due to the toothed wheel, the rotational velocity of the brake rotor could be calculated by equation 3.1:

$$\omega_{brake} = \frac{60 * f_{TTL}}{N_{teeth}} \quad (3.1)$$

Two toothed wheels were designed around the Omron SX770 photomicrosensor response (change of state: either *high* to *low*, or *low* to *high*) frequency limit specification of 1.0 kilohertz according to equation 3.2:

$$1 \text{ kHz} \geq f_{teeth} = \frac{2 * N_{teeth} * V_{rot}}{60} \quad (3.2)$$

26-toothed and 52-toothed wheels were designed to cover different rotational velocity ranges of the brake rotor with adequate resolution (see Appendix E.3: Shaft encoder toothed wheels, for design drawing). The maximum measurable rotational velocity was 1154 and 577 rpm for the 26-toothed and 52-toothed wheels, respectively. Although neither toothed wheel would be able to measure the maximum rotational velocity of the brake rotor (1678 rpm, see Section 3.5.3: Power transmission), the electric motor was never intended to be operated above 50 percent of its rotational velocity capability for this study.

The 26-toothed wheel was mounted to the upper power transmission shaft using a 2.0 in., one piece steel shaft collar from McMaster-Carr (part no.: 6435K27) drilled and tapped to accept ¼ in. – 20, by ¾ in. length socket head cap screws. The shaft collar used a 5/16 in. – 24 socket head cap screw to tighten and clamp to the shaft.

3.6. Power system

The purpose of the power system was to supply electrical power to the various electrical actuators and sensors installed on the experimental apparatus. Four different direct current power supplies formed the power system (see Figure 3.20):

- Elgar AT 8000A remote programmable, six channel output supply (clutch actuator and brake actuator driver)

- Philips PM2812 remote programmable, two channel output supply (shaft encoder photomicrosensor)
- Custom built, 9 VDC battery based supply (pressure transducer)
- Custom built, 12 VDC battery based supply (load cell transducer amplifier)

3.6.1. Elgar programmable power supply

The Elgar AT8000A was configured with six channels, each independently based upon a power module. There were four, 20 VDC, 10 A (200 W) and two, 10 VDC, 12 A (120 W) power modules installed in the AT8000A. These modules supplied power to the Duff-Norton electromechanical linear actuator that controlled the clutch (see Section 3.5.2: Clutch system) and to the Haydon hybrid electric linear actuator that controlled the brake (see Section 3.4.2: Electric linear actuator and master cylinder). Three, 20 VDC, 10 A modules were wired in series and programmed to supply the Haydon DCM8055 chopping driver with 60 VDC and a current limit of 10 A. A single, 10 VDC, 12 A ampere module was programmed to supply the Duff-Norton electromechanical linear actuator with 10 VDC and a current limit of 12 A. The remaining 20 VDC, 10 A and 10 VDC, 12 A power modules were not utilized. The AT8000A was programmed using National Instruments LabVIEW (version no.: 8.5), a National Instruments GPIB PCI card (part no.: 778032-01), and a National Instruments general purpose interface bus cable (part no.:763061-02). The AT8000A required re-programming of the voltage and current limit values for all channels each time the unit was turned on.

3.6.2. Philips programmable power supply

The Philips PM2812 contained two separate channels, one with a 30 VDC, 10 A, 60 W maximum rating, the other with a 60 VDC, 5 A, 60 W maximum rating. The PM2812 powered the Omron SX770 photomicrosensor utilized in the shaft encoder (see Section 3.5.4: Shaft encoder). The single, 60 VDC, 5 A, channel was programmed to supply the SX770 with 20 VDC and a current limit of 0.5 A. The remaining 30 VDC, 10 A, channel was not utilized. The PM2812 was programmed using National Instruments LabVIEW (version no.: 8.5), a National Instruments GPIB PCI card (part no.: 778032-01), and a National Instruments GPIB cable (part no.:763061-

02). The voltage and current limit values programmed into the PM2812 were saved as the power-on settings. This avoided the need to re-program all channels each time the unit was turned on.

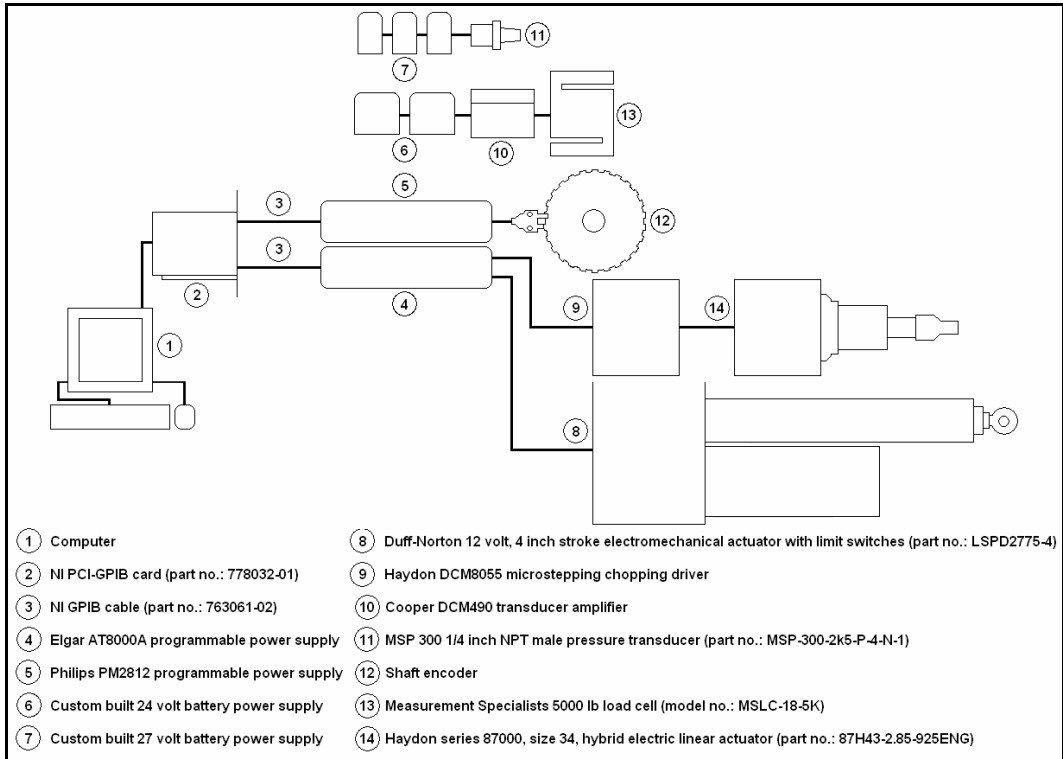


Figure 3.20: Power system schematic



Figure 3.21: Elgar AT8000A programmable power supply



Figure 3.22: Philips PM2812 programmable power supply

3.6.3. Battery-based power supplies

Two power supplies were custom built using batteries to help minimize the noise interference disrupting the pressure and load cell transducer signals. The first custom built power supply used three common nine volt batteries wired in series to generate 27 VDC to power the MSP 300 pressure transducer (see Section 3.4.3: Pressure transducer). The relatively low current draw of the MSP 300 allowed the use of common nine volt batteries; however, the Cooper DCM 490 amplifier (see Section 3.7.4: Load cell transducer) powering the load cell transducer would drain nine volt batteries within an unacceptably short time period. Therefore, the second custom power supply was built using two Werker 12 VDC, 7.5 Ah, AGM, sealed, non-spillable batteries from an UPS wired in series to generate 24 VDC to power the Cooper DCM490.



Figure 3.23: Custom built 27 VDC battery power supply

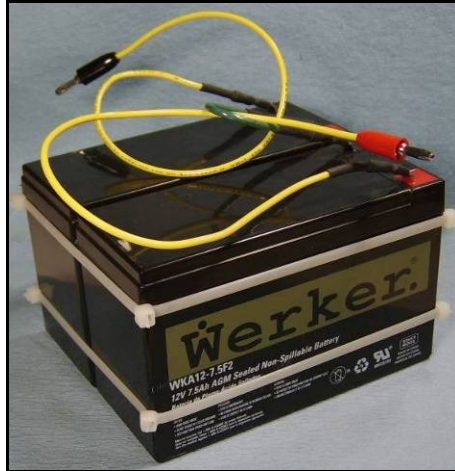


Figure 3.24: Custom built 24 VDC battery power supply

3.7. Measurement and control system

The purpose of the measurement and control system was to monitor and control the temperature, pressure, and drive systems installed on the experimental apparatus. The measurement and control system consisted of various hardware and software components.

3.7.1. Hardware connections

The various hardware components in the measurement and control system were (see Figure 3.25):

- Computer powered by a AMD Athlon™ 64 3800+ 2.4 GHz processor with 2.0 GB of RAM
- NI PCI-6221 68-pin multifunction DAQ card (part no.: 779066-01); 16-bit, 250 kHz, 16 single-ended analog inputs, two 16-bit analog outputs, 24 digital I/O and 2, 32-bit counters
- NI SCB-68 shielded I/O connector block (part no.: 776844-01)
- NI SHC68-68-EPM extended performance shielded cable, 1 m (part no.: 192061-01)
- NI USB-9211A 24-bit thermocouple DAQ units (part no.: 779436-01)
- NI PCI-GPIB high performance card (part no.: 778032-01)

- NI high quality, double-shielded GPIB cable, shielded plug and receptacles, 2 m (part no.:763061-02)

The PCI-GPIB card was installed in the computer and connected to the two programmable power supplies using the GPIB cables.

The PCI-6221 DAQ card was installed in the computer and connected to the SCB-68 I/O connector block using the SHC68-68-EPM cable. The various actuators and sensors were connected to the SCB-68 using the built in screw terminals (see Figure 3.26); however, the temperature sensors connected through separate USB-9211A thermocouple DAQ units which connected to the computer through USB ports with USB cables (see Figure 3.27). The various temperature sensors were connected to the USB-9211A using quick disconnect miniature connectors wired to the built in screw terminals.

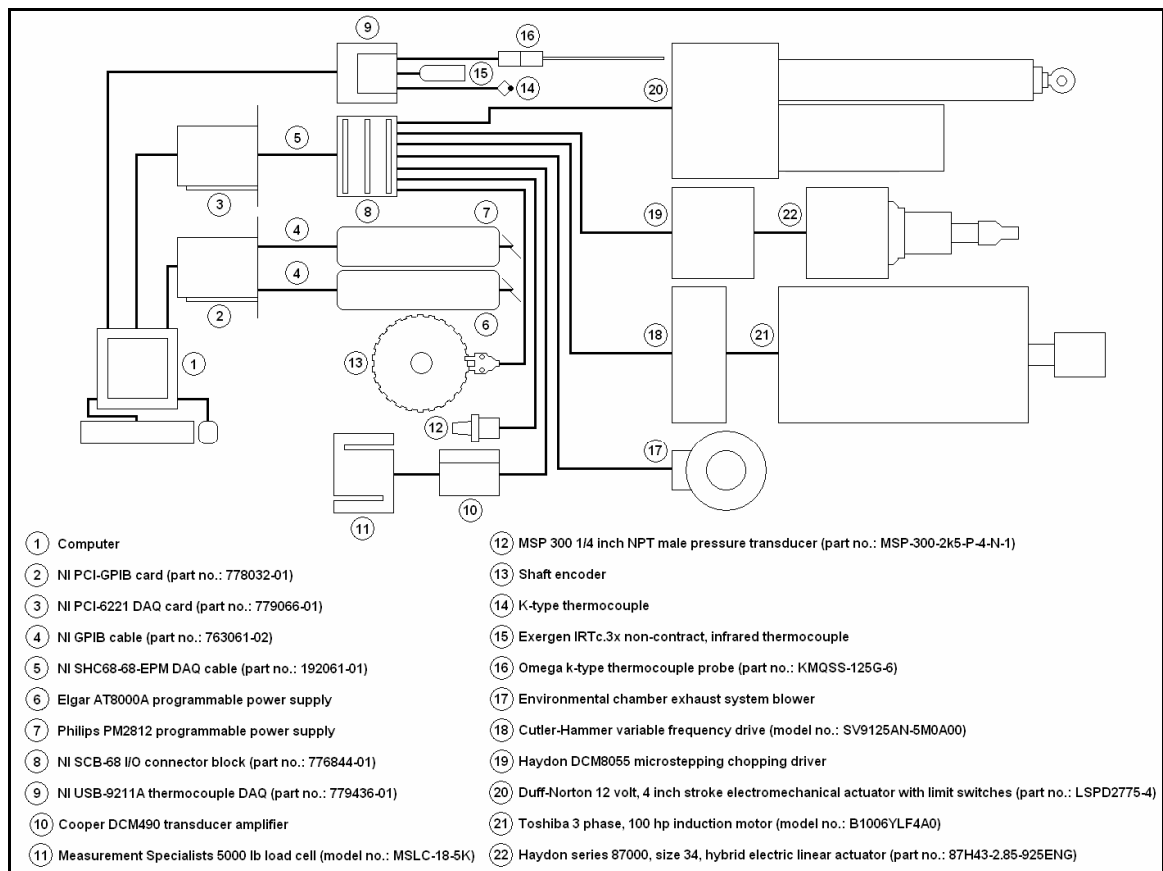


Figure 3.25: Measurement and control system hardware components

The following measurement, control and supply connections were made to the PCI-6221 DAQ card through the SCB-68 I/O connector block (see Appendix D.1: Shielded connector block):

Analog inputs (± 10 VDC):

- Pressure transducer (measurement)
- Load cell transducer (measurement)

Analog outputs (± 10 VDC):

- Electric motor speed (control)

Digital outputs (TTL: 0 or +5 VDC):

- Environmental chamber exhaust system blower on/off (control)
- Electric motor on/off (control)
- Brake actuator movement/speed (control)
- Brake actuator direction (control)

Digital inputs (TTL: 0 or +5 VDC):

- Clutch actuator limit switches (measurement)

Counter/timer inputs (TTL: 0 or +5 VDC):

- Shaft encoder (measurement)

Power supply (+ 5 VDC)

- Clutch actuator limit switches (supply)

The two analog inputs connected to the PCI-6221 DAQ card provided the pressure and load cell transducer signals. The respective signals varied between +1 to +5 VDC, and ± 5 VDC. The LabVIEW software scaled each signal to produce a measurement of the brake pressure (+1 VDC corresponded to 0 *psi*, +5 VDC corresponded to 2500 *psi*) and brake force (± 5 VDC corresponded to ± 5000 *lb_f*). Each of the analog inputs were connected to the SCB-68 in differential configuration and both required a single-pole, low pass filter.

The single analog output connected to the PCI-6221 data acquisition card controlled the electric motor speed by providing a 0 to +10 VDC signal directly to the VFD representing 0 to 100 percent of the electric motor speed (100 percent, or 10 VDC, corresponded to *1175 rpm*). By adjusting the analog output voltage, the electric motor speed was controlled.

The digital outputs connected to the PCI-6221 data acquisition card controlled the environmental chamber exhaust system blower on/off state, electric motor on/off state, and brake actuator speed and direction by providing a TTL signal. The blower state is controlled by providing AC power to the blower through a Crydom SSR (model no.: D2410, input-DC, output-AC) switched by the TTL signal output from the PCI-6221 (0 VDC corresponded to *off*, +5 VDC corresponded to *on*). The electric motor state is controlled by providing +24 VDC to the VFD through a Dayton SSR (model no.: 5Z950, input-DC, output-DC) switched by the TTL signal output from the PCI-6221 (0 VDC corresponded to *off*, +5 VDC corresponded to *on*). The brake actuator speed is controlled by providing a TTL signal from the PCI-6221 to the Haydon DCM8055 chopping driver. Each time the DCM8055 received a digital pulse the brake actuator would extend or retract a single step in the current programmed direction. By sending the DCM8055 a digital pulse train, the brake actuator would extend or retract at the pulse train frequency in the current programmed direction. This allowed the PCI-6221 TTL signal output to control the movement and speed at which the brake actuator extended or retracted. The brake actuator direction is controlled by providing a TTL signal from the PCI-6221 to the Haydon DCM8055 chopping driver (0 VDC corresponded to *retract*, +5 VDC corresponded to *extend*).

The single counter/timer input connected to the PCI-6221 DAQ card provided the shaft encoder TTL signal. The time interval between rising edges of this signal was measured and inverted by the PCI-6221 to produce a measurement of the TTL signal frequency. The LabVIEW software utilized equation 4.1 to produce a measurement of the brake rotor rotational velocity. The shaft encoder TTL signal required a debounce filter.

The single power supply output connected to the PCI-6221 DAQ card powered the clutch actuator limit switches with +5 VDC.

The following measurement connections were made to the USB-9211A thermocouple DAQ units:

No. 1 USB-9211A:

- Channel 1: Exergen IRTc.3x non-contact, infrared thermocouple
- Channel 2: Inner brake pad thermocouple
- Channel 3: Outer brake pad thermocouple
- Channel 4: Brake arm bushing thermocouple probe

No. 2 USB-9211A:

- Channel 1: Upper front pillow block bearing thermocouple probe
- Channel 2: Lower front pillow block bearing thermocouple probe
- Channel 3: Upper rear pillow block bearing thermocouple probe
- Channel 4: Lower rear pillow block bearing thermocouple probe

3.7.2. Hardware noise interference

To minimize noise interference on all input and output signals connected to the PCI-6221 DAQ card, shielded, twisted-pair wires were used and the shield was connected only to measurement ground.

In addition to the use of twisted-pair wires, several further steps were taken to specifically minimize the noise interference disrupting the pressure and load cell transducer signals. One such step, as previously mentioned, was the construction of custom built battery-based power supplies for both transducers (see Section 3.6.3: Battery-based power supplies). When powered from a supply plugged into an AC wall outlet, it was observed that the quality of the transducer signals was extremely poor; however, the signal quality would vastly improve if the transducer was powered by an isolated supply, such as a battery. It was believed that the electric motor, the major source of all noise interference for the experimental apparatus, was causing *building ground* fluctuations and therefore, affecting anything connected to the AC wall outlets, including the power, and measurement and control systems. A possible solution was proposed, but never implemented, to install an isolation transformer to effectively neutralize the *building ground*

fluctuations. Another step taken to minimize the noise interference disrupting the pressure and load cell transducer signals was to install single-pole, low-pass filters to the SCB-68 at the screw terminal connections of both signals. Single-pole, low-pass filters attenuate signals with frequencies greater than the *cut-off frequency* using a single resistor and capacitor according to equation 3.3:

$$f_c = \frac{1}{2\pi R_{lp} C_{lp}} \quad (3.3)$$

Two single-pole, low-pass filters were constructed from a 10 kΩ resistor and 1.5 μF capacitor with a cut-off frequency of 10.6 Hz and soldered to the SCB-68 to filter the pressure and load cell transducer signals (see Figure 3.28).

To further reduce noise interference, the pressure and load cell transducer signals were connected to the SCB-68 in differential mode, where neither the positive or negative inputs from the sensor were connected directly to the measurement system ground; however, both signals required a 10 kΩ bias resistor connected between the negative input from the sensor and the measurement system ground to avoid erroneous readings that can occur when *floating signal sources*, or those signals not connected to “building” ground, are connected in differential mode to the SCB-68 (see Figure 3.28). The pressure and load cell transducer signals were floating signal sources since they were both powered from battery supplies.

As previously mentioned, the battery-based power supplies were constructed to help reduce noise interference with the pressure and load cell transducer signals.

Due to noise interference issues with the shaft encoder signal, an internal programmable debounce filter was enabled and configured on the PCI-6221 DAQ card. The debounce filter only allows a transistor-transistor logic state change to be measured if the state change was sustained for a certain period of time, thus removing any quick state changes due to noise interference. The programmable debounce filter had three selectable settings: 125 ns (8.0 MHz), 6.425 μs (155.6 kHz), and 2.56 ms (390 Hz). Since the shaft encoder photomicrosensor had a response frequency limit specification of 1.0 kHz, the 6.425 ms debounce filter setting was selected.

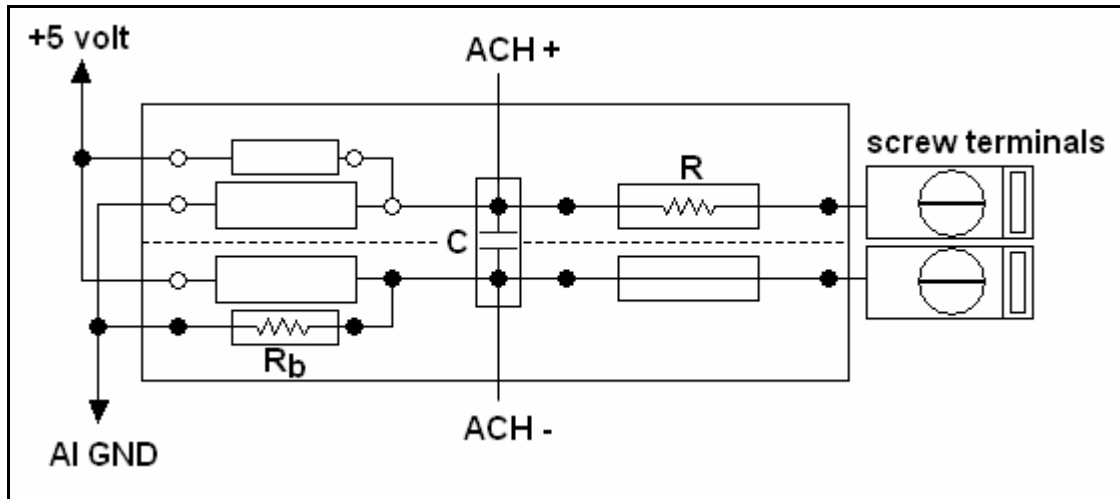


Figure 3.28: Circuit schematic of a single SCB-68 analog input channel with single-pole, low-pass filter components (R, C) and bias resistor (R_b)

3.7.3. Software programs

The various software components in the measurement and control system were:

- NI LabVIEW (version: 8.5) core programming software
- NI DAQmx (version: 8.6.1) DAQ driver software
- NI NI-488.2 (version: 2.40) GPIB controller software
- NI NI-VISA (version: 4.0) universal I/O interface software
- NI LabVIEW PID control toolkit (version: 8.2) software

The various National Instruments software packages were used to create two different measurement and control programs based upon manual or automated operation of the experimental apparatus. The manual program allowed the user to adjust the values for the various controlled components *on-the-fly* as the user was operating the experimental apparatus. This meant the user could, through the front panel of the program, turn the electric motor on or off, adjust the electric motor speed, adjust the brake pressure, turn the environmental chamber blower on or off, and disengage or engage the clutch at will (see Figure 3.29). In contrast, the automated program required the user to construct a test sequence before operating the experimental apparatus. A test sequence contained any number of cycles for which values for

each controlled component were defined for each cycle. Once submitted, the test sequence would be interpreted by the automated program and the experimental apparatus would be operated, without user inputs, through each cycle according to the defined values for each controlled component (see Figure 3.30).

The overall structure of both programs was based upon a standard state machine consisting of multiple states that execute code and determine the state transitions.

The manual operation program contained three states: *initialize*, *run* and *shutdown* (see Figure 3.31). The *initialize* state zeroed or reset all outputs from the PCI-6221 data acquisition card and programmed the Elgar power supply to the required power-up settings of the brake actuator. The *initialize* state transitioned to the *run* state where the measurement and control of the various actuators and sensors occurred. The *run* state read all eight temperature sensors, pressure and load cell transducers, and the shaft encoder. The *run* state controlled the brake actuator based upon target brake pressure user input, the electric motor based upon on/off state user input, the electric motor speed based upon target brake rotor rotational velocity user input, and the environmental chamber exhaust blower based upon on/off state user input. The manual operation program would continue to execute the *run* state until the user pressed the *abort test* button, upon which the program would transition to the *shutdown* state. The *shutdown* state zeroed or reset all outputs from the PCI-6221 DAQ card and zeroed the Elgar power supply.

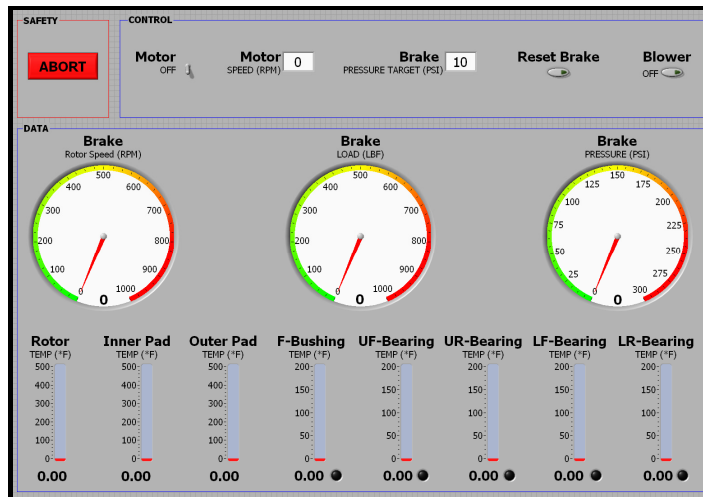


Figure 3.29: Manual operation program front panel

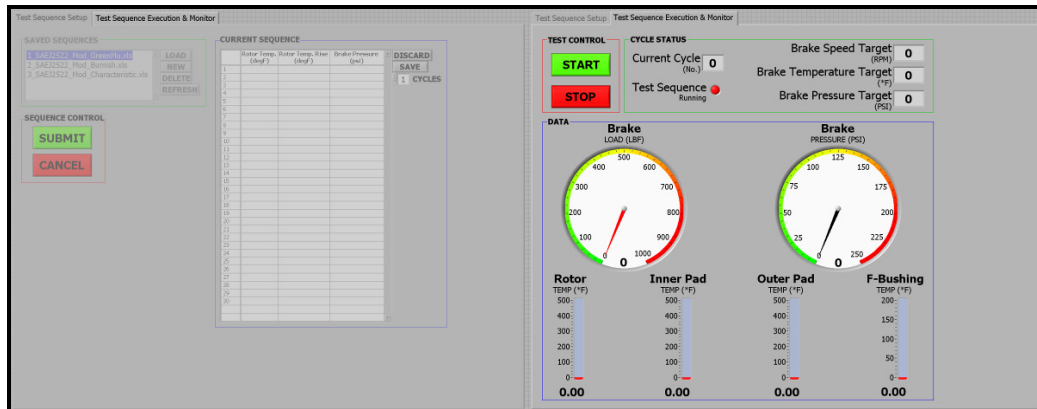


Figure 3.30: Automated operation program front panel

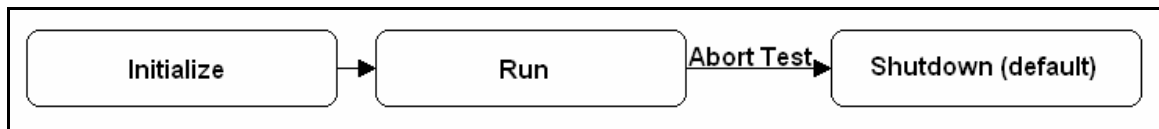


Figure 3.31: Manual operation program state machine diagram

The automated operation program contained seven states: initialize front panels, initialize test sequence, load/new/delete, construct test sequence, initialize Elgar & DAQmx, run, and shutdown (see Figure 3.32). The initialize front panels state zeroed or reset all user controlled inputs found on the program's front panel and transitioned to the initialize test sequence state, where the test sequence display on the program's front panel was reset. The load/new/delete state allowed the user to load, create, delete, or cancel a test sequence or refresh the list of available test sequences. If the user desired to load or create a test sequence, the state would transition to the construct test sequence state. The construct test sequence state allowed the user to adjust the number of cycles of, save, submit, discard or cancel the current sequence. If the user desired to discard the current sequence, the state would transition to the initialize test sequence state. If the user desires to submit the current sequence to run on the experimental apparatus the state would transition to the initialize Elgar & DAQmx state. If the user desired to cancel the sequence and abort the program, the state would transition to the shutdown state.

The initialize Elgar & DAQmx, run and shutdown states were functionally the same to the initialize, run and shutdown states from the manual operation program, respectively.

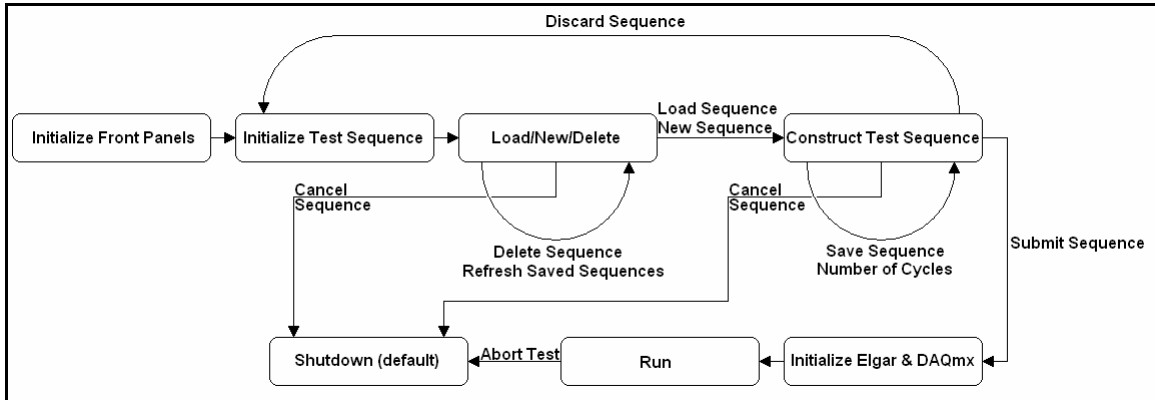


Figure 3.32: Automated operation program state machine diagram

3.7.4. Load cell transducer

Torque generated by the brake system during a brake application was measured by a Measurement Specialists s-type, tension-compression load cell transducer (model no.: MSLC-18-5K) powered by a Cooper Instruments and Systems universal inline transducer amplifier (model no.: DCM 490) with the following specifications:

- *Load cell range:* $\pm 5\,000\text{ lb}_f$
- *Load cell power supply:* 10 VDC
- *Load cell output:* 3 mV/V
- *Transducer power supply:* 24 to 32 VDC
- *Transducer output:* $\pm 5.0\text{ VDC}$, 2.5 mA, analog

The Cooper DCM 490 supplies a regulated voltage to power the load cell and amplifies the millivolt output from the load cell into a $\pm 5.0\text{ VDC}$ analog signal measured by the PCI-6221 DAQ card.

The load cell was secured to the frame of the experimental apparatus and attached to the brake caliper through the use of two mounts custom built from 6061-T6 aluminum and

appropriate hardware (see F.5: Load cell, for exploded view of assembly). The lower mount secured the load cell to the frame of the experimental apparatus and was compatible with the extruded aluminum and hardware manufactured by 80/20, Inc used to construct the frame (see Appendix E.7: Load cell lower mount, for design drawing). The upper mount attached the load cell to the brake caliper using an existing threaded feature at the base of the caliper (see Appendix E.8: Load cell upper mount, for design drawing).

3.8. Equations

3.8.1. Coefficient of friction

The coefficient of friction was calculated during the post-processing of the experimental apparatus test data from the measured values of brake pressure and force according to equation 3.4:

$$\mu = \frac{F_{lc} L_{lc}}{N_p A_p P_b R_e} \quad (3.4)$$

Where:

- $L_{lc} = 5.0$ in.
- $N_p = 2$
- $A_p = 2.41$ in²
- $R_e = 3.82$ in.

The values of brake pressure and force were measured by the pressure and load cell transducers, respectively.

3.8.2. Sliding distance

The sliding distance of the brake pad during brake application was calculated during the post-processing of the experimental apparatus test data from the measured time of brake application according to equation 3.5:

$$L_{sliding} = 2\pi R_e \omega_{brake} t_{brake} \quad (3.5)$$

Where:

- $Re = 3.82$ in.
- $\omega_{brake} = 836$ rpm

The time of brake application was extracted from the experimental apparatus test data as the cumulative time for which the brake pressure was above a threshold of 25 psi.

3.8.3. Wear rate

The brake rotor and pad wear rates were calculated during the post-processing of the test specimen mass data from the measured mass loss and calculated sliding distance according to equations 3.6 and 3.7, respectively:

$$W'_{rotor} = \frac{\Delta m_{rotor}}{L_{sliding}} \quad (3.6)$$

$$W'_{pad} = \frac{\Delta m_{pad}}{L_{sliding}} \quad (3.7)$$

3.9. Safety system

The purpose of the safety system was to provide a way to neutralize the experimental apparatus in case of an emergency. The safety system consisted of two, Eaton Cutler-Hammer twist release maintained, 40 mm red mushroom pushbuttons (part no.: E22LLB2B), with two normally open contacts per pushbutton, wired in series. Both pushbuttons were wired to the Elgar programmable power supply and the Cutler-Hammer VFD (see Figure 3.33).

The Elgar AT8000A programmable power supply provided an emergency shutdown input which was wired to normally open contacts located in both pushbuttons. When the emergency shutdown input was triggered by the engagement of either pushbutton, the Elgar would zero power output on all channels therefore, as configured in the experimental apparatus, would stop supplying power to the clutch and brake actuators rendering both components motionless. To resume operation of the actuators, both pushbuttons would need to be disengaged and the LabVIEW measurement and control program restarted.

The Cutler-Hammer VFD provided a fault input which was wired to normally open contacts located in both pushbuttons. When the fault input was triggered by the engagement of either pushbutton, the variable frequency drive would interrupt any power being sent to the electric motor, rendering it motionless. To resume operation of the motor, both pushbuttons would need to be disengaged and the fault input would need to be reset on the VFD front panel.

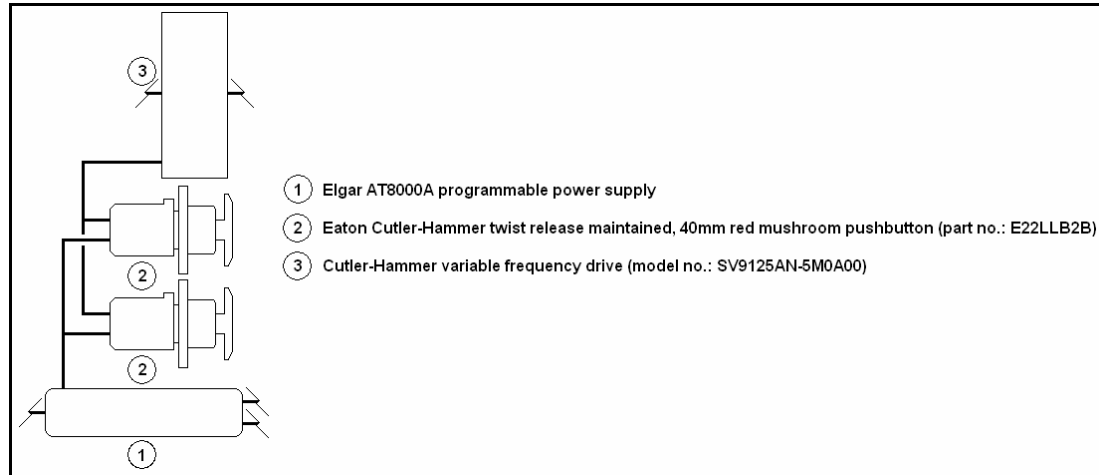


Figure 3.33: Safety system schematic

One mushroom pushbutton was mounted to the door frame opening to the experimental apparatus test cell, while the other was mounted on a mobile chassis which could be carried around the experimental apparatus and into the control room (see Figure 3.34).



Figure 3.34: Eaton Cutler-Hammer mushroom pushbuttons as-installed on the door frame (left) and on a mobile chassis (right)

3.10. Implementation of Inertia

Since the wear simulation was based, at least in part, on *SAE J2522: Dynamometer Global Brake Effectiveness* [43], which required the use of inertia to perform testing, inertia was implemented on the experimental apparatus.

The amount of kinetic energy converted during a brake application is given by equation 3.8:

$$KE_{brake} = \frac{1}{2} m (V_f^2 - V_i^2) \quad (3.8)$$

Specific vehicle applications require different amounts of inertia to simulate the correct amount of converted kinetic energy. Several possible solutions existed for simulating inertia: mechanical, electrical, energy compensation, or energy equivalent. Although all three solutions possessed specific advantages and disadvantages, ultimately, the energy equivalent method was adopted for inertia simulation for the current study.

3.10.1. Mechanical

Mechanical inertia simulation uses discrete mechanical flywheels [44] attached to the driven shaft of a brake dynamometer to store energy in the form of rotational kinetic energy based upon angular velocity and moment of inertia according to equation 3.9:

$$KE_{rot} = \frac{1}{2} I \omega^2 \quad (3.9)$$

Moment of inertia varies for objects based upon mass and geometrical distribution of mass. Most commonly used shape for discrete flywheels are cylinders whose moment of inertia is described by equation 3.10:

$$I_{flywheel} = I_{cyc} = \frac{1}{2} m_{cyc} r_{cyc}^2 \quad (3.10)$$

Thus, mechanical inertia simulation attempts to simulate the correct amount of kinetic energy converted during a brake application by equating it to the rotational kinetic energy of the flywheels as given by equation 3.11:

$$KE_{brake} = KE_{rot} = \frac{1}{2} I_{flywheel} (\omega_f^2 - \omega_i^2) \quad (3.11)$$

The biggest advantage for using mechanical inertia simulation is the ease of implementation. Although the cylinder mass can be quite large, giving rise to potential manufacturing and handling problems, inertia values can be readily modified by changing flywheels; however, several disadvantages exist. If inertia to cover a wide range of vehicle applications is needed, numerous flywheels must be readily available and, due to the discrete nature, flywheels of differing moment of inertia values must also be readily available [44]. The discrete nature means a concession between number of flywheels, inertia increment, and total range of inertia simulation [45]. Additionally, speed dependent inertia effects, such as aerodynamic drag, can only be approximated using mechanical inertia simulation [45].

3.10.2. Electrical

Electrical inertia simulation uses careful control of the electric motor powering a brake dynamometer to add or remove energy to simulate inertia [46], as such, two solutions exist based upon torque or speed feedback [45].

In a torque feedback based simulation, feedback to a motor controller of measured shaft torque is used to maintain the proper amount of torque during a particular braking situation [45]. The advantages in implementing a speed feedback based simulation, such as the elimination of the need for a rotating torque cell transducer, the ability to adapt to changing losses (i.e. parasitic drag) from by the dynamometer, and the small magnitude of maximum possible error (less than one percent of full scale inertia capability), make it the preferred approach over a torque feedback based simulation [45].

In a speed feedback based simulation, changes in motor speed are calculated based upon required deceleration rates over very small time intervals and implemented using fast reacting control over the motor armature current [45]. Fast reacting control uses a PID strategy (closed-loop) with a fast feed-forward (open-loop) strategy operating at a rate of 100 Hz [45]. The open-loop control allows instant response of the motor to changes in required current, while

closed-loop control removes any error from the open-loop *guess* based on calculated required motor torque converted to estimation of equivalent motor current [45].

The biggest advantage for using either electrical inertia simulation technique is the ability to accurately represent the exact inertia for a given vehicle application, including inertia effects encountered on a real vehicle such as aerodynamic drag and parasitic losses; electrical simulation can even account for the potential losses (i.e. parasitic drag) created by the dynamometer itself [45]. One disadvantage of using electrical inertia simulation is the implementation which requires appropriate control hardware, software, and algorithms to be designed and developed potentially costing excessive money, time and inevitably becoming too complicated [46]. The range of electrical inertia simulation is determined by the available power that can be generated from the electric motor, if it is underpowered then certain inertia values will not be able to be simulated using electrical inertia simulation [45], [46].

3.10.3. Energy compensation

Energy compensation-based inertia simulation is a hybrid of mechanical and electrical inertia simulations. Flywheels are used as the primary source of inertia, while the electric motor is used as the secondary source of inertia to adjust (compensate) the inertia to the correct value [44], [46]. This hybrid simulation combines the advantages of, while minimizing or all together eliminating the disadvantages of the mechanical and electrical inertia simulations; however, the need for appropriate control hardware, software, and algorithms to be designed and developed still exists prohibiting the implementation of a hybrid simulation for the current study.

3.10.4. Energy equivalent

Energy equivalent inertia simulation uses a measurement of the brake rotor surface temperature increase to control the duration of a brake application during dynamometer testing. For a specific *real-world* braking event, the rotor surface temperature increase could be estimated as a measure of the thermal energy absorbed by the rotor. Measuring rotor surface temperature and controlling the duration of the brake application by enforcing the estimated rotor surface temperature increase would result in equal amounts of energy conversion, kinetic to thermal, on

the dynamometer brake application as on the *real-world* braking event. This allows different parameters to be used during dynamometer testing than those during a specific *real-world* braking event such as rotor rotational velocity and brake pressure, while the rate of rotor surface temperature increase could differ. Since energy equivalent inertia simulation does not add energy to the brake system, the dynamometer testing must be conducted with the electric motor continuously providing torque to maintain a constant brake rotor rotational velocity during the brake application. Failing to do so would result in prompt brake system lock up due to the brake application, potentially causing catastrophic damage to the dynamometer.

The following set of brake application parameters were used to estimate the rotor surface temperature increase during a *real-world* braking event:

- Vehicle mass, deceleration rate, initial and final velocities
- Brake front-rear distribution percentage
- Rotor thermal energy distribution, swept area, density, specific heat and thermal conductivity

Equations presented in *Brake Design and Safety*, by Rudolf Limpert [47], were used to estimate the rotor surface temperature increase from the given brake application parameters (see Appendix C.2: Brake rotor surface temperature). Specifically, equation 3.12 defined the rotor surface temperature increase [47]:

$$\Delta T_b = \sqrt{\frac{5}{18}} \left(\frac{q''_{(o)} \sqrt{t_f}}{\sqrt{\rho_r c_r k_r}} \right) \quad (3.12)$$

Equation 3.12 was used to calculate the rotor surface temperature increase for various brake pressures and subsequent vehicle deceleration rates for a lightweight, single seat racecar.

4. VERIFICATION

4.1. Objectives

A lightweight, single seat, open wheel racecar powered with a small displacement engine was selected as the vehicle application for the verification testing. Brake system components were selected or manufactured based upon their suitability for use as part of the front brake system on a lightweight racecar.

Testing was performed to verify the logic of the wear simulation and the functionality of the experimental apparatus. Specifically, brake rotor and pad wear rates were determined at various brake pressures to investigate the possibility of wear rate differences due to the application of a cryogenic treatment process to a small set of brake rotors.

4.2. Brake system components

Several components were either purchased or manufactured in order to install a brake system on the experimental apparatus based upon a lightweight, single seat, open wheel racecar powered with a small displacement engine. The brake system components included: caliper, pads, rotor, rotor hat, and caliper mount.

4.2.1. Caliper

The Wilwood Dynalite billet single caliper (DLS) was selected due to its availability and suitability as a front brake caliper for a lightweight racecar. The DLS is a compact, high performance, two-piston fixed, two-piece caliper accommodating a range of brake rotor diameters and thicknesses. In addition, Wilwood offers a vast selection of brake pads for use with the DLS, which are retained in the caliper by quick clips. The specific details of the DLS used are as follows (see Figure 4.1) [49]:

- *Body material:* aluminum
- *Piston material:* stainless steel

- *Piston diameter:* 1.75 in.
- *Rotor diameter range:* 6.0 in. to 13.0 in.
- *Rotor thickness range:* 0.25 in. to 0.375 in.
- *Mount spacing:* 3.25 in.



Figure 4.1: Wilwood Dynalite billet single caliper

4.2.2. Pads

Wilwood offers several options of brake pad compounds for use with the Wilwood Dynalite billet single caliper [50]:

- PolyMatrix A, H, B, C, E, Q
- Composite Metallic
- SmartPad BP-10, BP-20, BP-30
- ProMatrix

The selection of suitable pad compound was driven by the coefficient of friction profile provided by Wilwood (see Figure 4.7). Ultimately, the PolyMatrix A compound was selected for its peak coefficient of friction, approximately 0.68, and ability to sustain a high coefficient of friction through out the temperature range when compared to the other compounds. Wilwood describes the PolyMatrix A compound as [50]:

- Ultimate high friction compound with aggressive initial response
- Long wear rate for severe duty and sustained high temperature braking
- Immediate low temperature response for applications requiring high response at low temperatures
- Compatible with iron, steel, and titanium rotors
- Race only compound for use in severe duty applications requiring an aggressive response and durability in the highest temperature ranges
- For steel plate rotors requiring fast response at low temperatures with resistance to fade during periodic or temporary high temperature spikes

Six sets of Wilwood PolyMatrix A brake pads (two pads per set) were purchased from Neal Products, Inc. of San Diego, California, for \$42.00 per set. A portion of the pad backing plate was machined away and drilled to allow insertion of a k-type thermocouple wire to measure the brake pad temperature (see Figure 4.2).



Figure 4.2: Wilwood PolyMatrix A brake pads

4.2.3. Rotors

The use of the Wilwood Dynalite billet single caliper constrained the rotor geometry between 6.0 in. and 13.0 in. in diameter, and 0.25 in. to 0.375 in. in thickness. Additionally, another constraint was imposed by the need to mount the rotor to the brake hat and a criteria was

imposed by the need to have an inner portion of the rotor surface be unworn by the brake pads. This criteria was imposed for two reasons: optical microscopy, rotor thickness measurements.

To sufficiently meet the constraints and criteria of the design, a rotor geometry of 9.0 in. diameter and 0.25 in. thickness was designed with appropriate rotor hat design details (see Appendix E.4: Brake rotor, for design drawing). The rotor design resulted in a predicted mass of 1.675 kg. It is noted that although previous design efforts, specifically for a lightweight, single seat racecar, have resulted in a rotor geometry of 8.375 in. diameter and 0.125 in. thickness, these efforts have been driven by weight efficiency and packaging constraints and criteria which are not imposed for the current study.

Six rotors were manufactured based upon the design (see Figure 4.3; see Appendix E.4: Brake rotor, for design drawing). A single rotor was designated as a “test” rotor to help develop the functionality of several of the experimental apparatus’ systems, including feedback control of the pressure system. Two of the remaining rotors were set aside as *control* rotors, while the final three rotors were cryogenically treated by International Cryogenic Engineering, Inc.

4.2.3.1. Effective radius

The effective brake rotor radius is the distance from the center of the brake rotor to the point where the brake force imposed from the brake pads can be concentrated, measured radially. Ideally, the concentration of brake force at the effective radius will produce the same value for brake torque as that produced from the brake force distributed over the brake pad area. In the current study, the interpretation of the effective brake radius was not to place it at the geometric center of the brake pad, but to place it at the distance where equal rotor surface areas under the brake pad are swept in a single revolution on the inside and outside of the effective radius (see Appendix C.3: Effective brake rotor radius).

Using equation C.29 in Appendix C.3, the effective radius of the rotors designed for the current study was 3.82 in., for the following brake system parameter values:

- $D_r = 9.0$ in.
- $L_p = 1.5$ in.

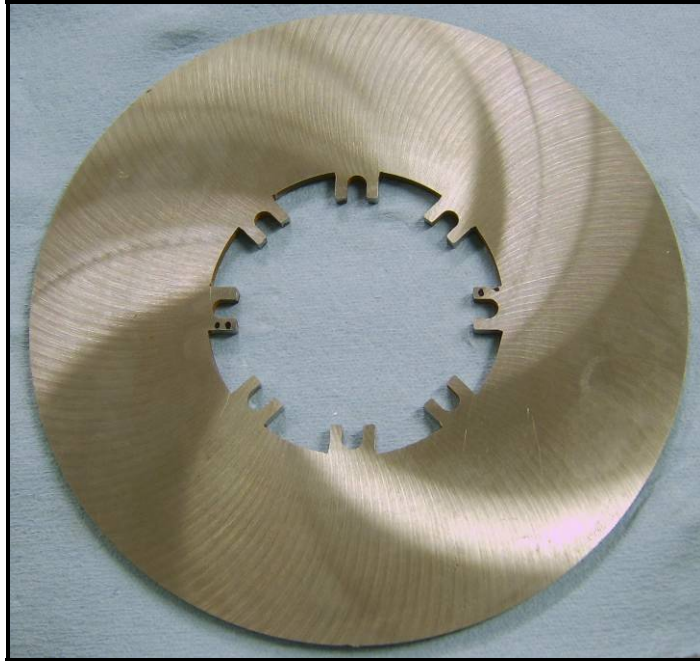


Figure 4.3: As manufactured ASTM A36 steel rotor

4.2.3.2. Material

Preliminary discussions with International Cryogenic Engineering Inc. (ICE) concerning preferred material for cryogenic treatment resulted in two potential solutions: SAE G3000 gray cast iron and SAE 1018 carbon steel. Initial problems in locating SAE G3000 in plate form eliminated the possibility of its use.

According to ICE, SAE 1018 carbon steel demonstrated very positive results in their laboratory and real-world testing. Although ICE had not conducted any tests specifically relating to frictional wear properties, they believed SAE 1018 used as a brake rotor material would yield similar positive results; however, working with a local metal supplier it was determined that a 2 ft. x 2 ft. x $\frac{1}{4}$ in. plate of SAE 1018 would cost \$462 and was not stocked locally.

With the raw material being cost prohibitive for the current study, SAE 1018 carbon steel was discarded in favor of a more cost effective material. The local metal supplier stocked ASTM A36, a common structural steel. The price of a 2 ft. x 2 ft. x $\frac{1}{4}$ in. plate of ASTM A36 was \$33, a mere 7 percent of the cost of a SAE 1018 plate of the same dimensions. Feedback from ICE

indicated their cryogenic treatment would impart roughly the same benefits on a brake rotor manufactured from ASTM A36 compared with one manufactured from SAE 1018. Thus concluded to proceed with the manufacture of brake rotors using ASTM A36 steel.

4.2.3.3. Manufacture

Six rotors were manufactured from ¼ in. thick ASTM A36 steel plate using a water jet cutter at Colorado WaterJet Company of Berthoud, Colorado. To insure flatness of and parallelism between surfaces, as well as exposing a fresh friction surface beneficial for rotor-pad interaction, the rotors were surface ground by ACME Machine, Inc. of Fort Collins, Colorado to 0.240 in. thickness. The material and manufacturing price breakdown was:

- \$ 4.75 – material price per rotor (ASTM A36 steel), CO WaterJet
- \$30.00 – water jet time price per rotor, CO WaterJet
- \$15.00 – surface grinding price per rotor, ACME Machine
- \$49.75 – total price per rotor for material and manufacture

4.2.3.4. Cryogenic treatment

Cryogenic treatment of three rotors was carried out by ICE at their facility in Denver, Colorado, where a propriety oven was constructed to facilitate cryogenic treatment using liquid nitrogen, as the cooling medium, and a heat exchanger to control oven temperature without subjecting samples to direct contact with liquid nitrogen. The three rotors were subjected to the following cryogenic process parameters [51] (see Figure 4.4):

- Ramp from room temperature (16 °C) to -192 °C at a rate of approximately -0.175 °C/min
- Soak at -192 °C for approximately 15 hr.
- Warm from -192 °C to room temperature in oven at natural rate

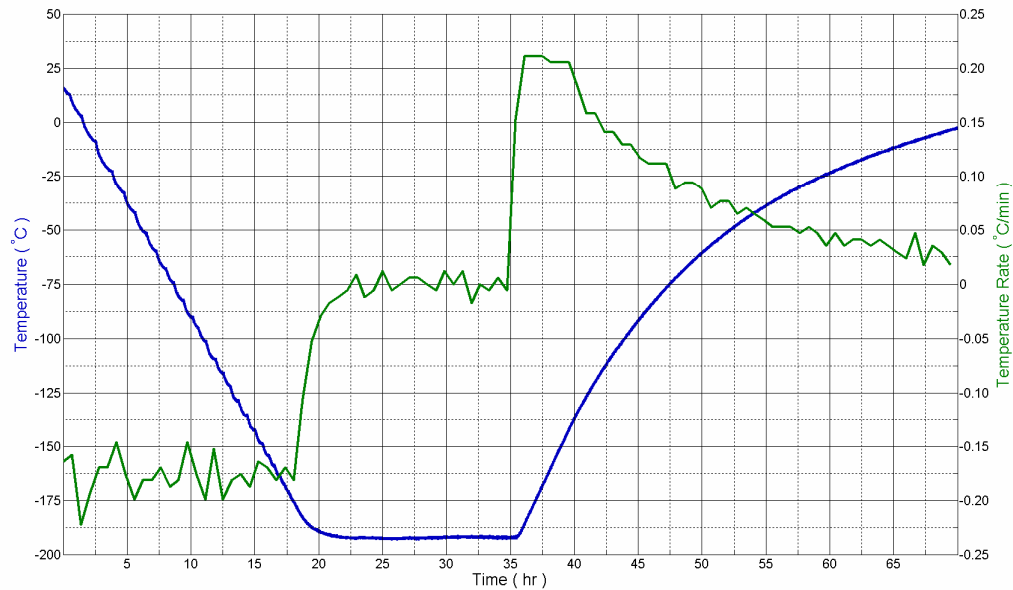


Figure 4.4: ICE cryogenic treatment process profile [51]

Following the cryogenic treatment, a mild temper was applied to the three rotors using the following process parameters [51]:

- Ramp from room temperature (16 °C) to 160 °C at a rate of +4.0 °C/min
- Soak at 160 °C for 1 hr.
- Cool from 160 °C to room temperature in oven at natural rate

4.2.4. Brake hat

To locate each brake rotor on the upper driven shaft of the experimental apparatus, a rotor hat was designed and manufactured. Due to material availability constraints, the rotor hat was designed to be manufactured from a 4.0 in. diameter round of 6061-T6 aluminum readily available. Additional constraints included the need for a keyway to allow the upper driven shaft to power the rotor, and for the rotor hat to be located axially on the driven shaft by a nut and collar. The idea behind using a nut and collar to axially locate the rotor hat, and therefore the rotor itself, was to use the collar to clamp onto the shaft and locate the back of the hat while the nut would tighten down against the front of the hat securing it (see Appendix F.3: Brake rotor and hat, for

exploded view of assembly). Design criteria included interfacing with the brake rotor, allowance for differences in thermal expansion between the hat and rotor, minimizing pad knock back and ease of manufacture.

Pad knock back occurs when the rotor no longer runs parallel between the pads, due to undesirable deflections in the suspension. This results in the rotor forcing the pistons to retract into the caliper body and thus requiring excessive pedal travel to re-extend the pistons to establish braking force through rotor-pad contact [52]. Although pad knock back is a condition encountered by racecars under strong cornering forces, pad knock back could occur on the experimental apparatus due to slight misalignment of any component and should be avoided to help ensure reliable, repeatable operation of the experimental apparatus.

A single rotor hat was designed and manufactured from 6061-T6 aluminum (see Figure 4.5; see Appendix E.5: Brake hat, for design drawing). Alloy steel standard shoulder screws (10-24 thread, $\frac{1}{4}$ in. shoulder diameter, $\frac{1}{4}$ in. shoulder length) were used to secure the brake rotor to the hat and to minimize pad knock back by allowing a minimal amount of axial movement (approximately 0.013 in.) between the rotor and hat.

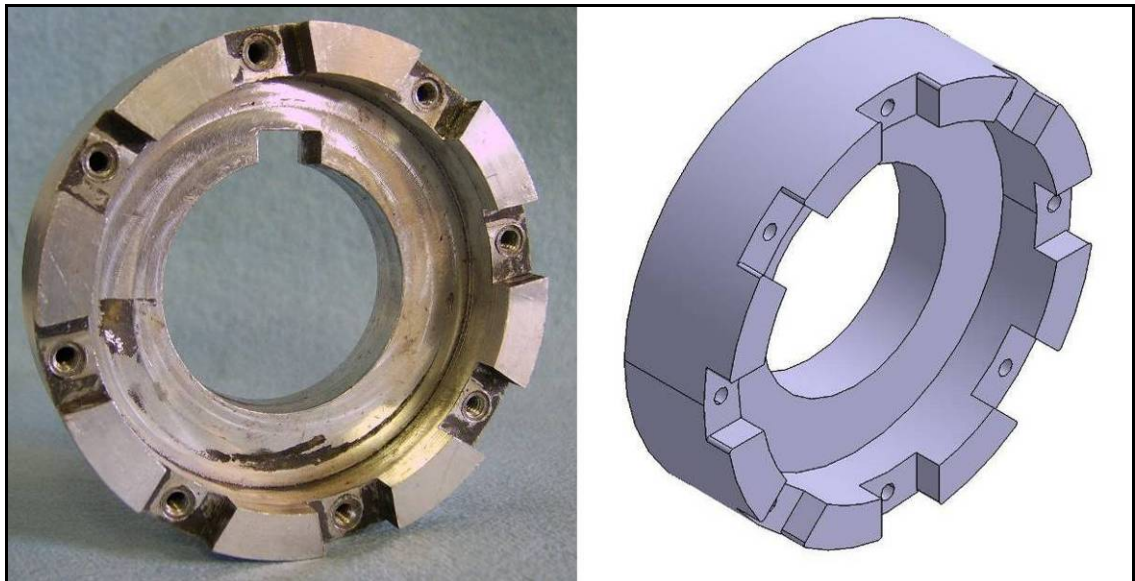


Figure 4.5: Brake hat as-manufactured (left) and as-designed (right)

4.2.5. Caliper mount

To locate the brake caliper on the upper driven shaft of the experimental apparatus, a caliper mount was designed and manufactured. The mount needed to accommodate either a 9.0 in. or an 8.375 in. rotor diameter as used for the current study and as typically used on a lightweight racecar, respectively. The mount was also required to locate the caliper such that the outside rotor diameter was matched to the furthest outboard edge of the pads, radially and such that the rotor was located equally between the two caliper pistons, axially. To allow the load cell to measure the brake force generated by the rotor-pad contact, the upper driven shaft needed to rotate freely within the mount, while the load cell prevented rotation of the mount by fixing it to the experimental apparatus. When the brake application occurs, the rotor will try to revolve the caliper, and thus the mount, around with it; however, the load cell will resist this rotation and in the process develop a tensile force which the load cell can measure. From this tensile force the brake torque can be calculated. The mount was required to be a modular component to allow different brake systems to be installed on the experimental apparatus.

A single caliper mount was designed and manufactured from 6061-T6 aluminum (see Figure 4.6; see Appendix E.6: Caliper mount, for design drawing). The mount was manufactured in three pieces, one caliper flange and two bushing rings, and bolted together using four, $\frac{1}{4}$ in. – 20 thread, 1 $\frac{1}{4}$ in. length socket head cap screws. Two flanged, SAE 841 oil-impregnated sintered bronze bushings (nominal ID: 2.00 in., nominal OD: 2.25 in., nominal length: 0.75 in.), manufactured by Bunting Bearings (part no.: FF2203-2), were used to allow the upper driven shaft to rotate freely within the mount. Due to the relatively low maximum use temperature of the bronze bushings (approximately 220 °F), a thermocouple probe was installed in the mount to monitor the temperature of the bushing nearest to the brake rotor. To assist in the press-fit installation of the bronze bushings, a $\frac{5}{64}$ in. x 45° chamfer was machined into each bushing ring on the outer face at the inner diameter edge. The bronze bushings were originally intended to be press-fit into the bushing rings, but installation problems required a different solution using Loctite 638 retaining compound to *glue* the bushings securely into the rings. The caliper was bolted to the mount using two, $\frac{3}{8}$ in. – 24 thread, 1 $\frac{1}{4}$ in. length socket head cap screws and two, $\frac{3}{8}$ in. –

24 thread distorted-thread locknuts. (see Appendix F.4: Caliper mount, for exploded view of assembly).

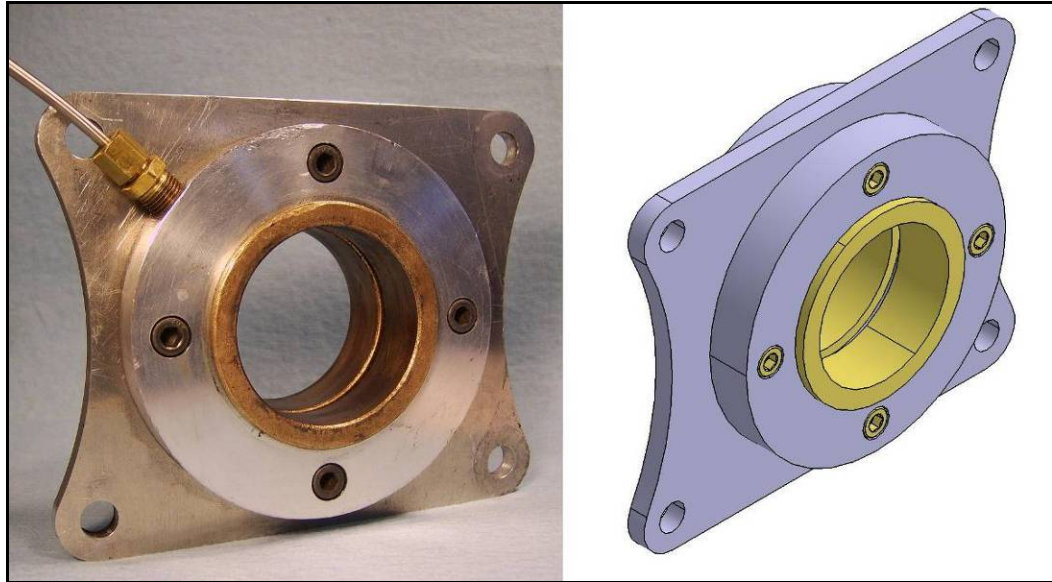


Figure 4.6: Caliper mount as-manufactured with thermocouple probe and bushings installed (left) and as-designed (right)

4.3. Procedure

Wear simulation of five test samples was conducted using the experimental apparatus. Each test sample consisted of a brake rotor and two brake pads. Two of the test samples were designated as controls, no additional processing of the rotors or pads was carried out after manufacture (rotors) or purchase (pads). The remaining three test samples, specifically the rotors, were cryogenically treated; the corresponding pads underwent no additional processing after purchase. All five test samples were subjected to the same bedding test procedure in an attempt to maximize the coefficient of friction between the rotor and pads. Some of the test samples were subjected to different wear test procedures to study the influence of pressure on wear rates, and to investigate the initial brake applications on wear rate. Thus, three test specimen groups were formed of a single control and a single cryogenically treated sample, with the last treated sample having no corresponding control sample:

- Test specimen group 1: control 1 + treated 1
- Test specimen group 2: control 2 + treated 2
- Test specimen group 3: treated 3

The mass of each specimen was measured before and after bedding, and after each repetition of the wear test procedure. Mass data was collected to determine the wear rates of each sample using the calculated mass loss versus measured sliding distance. The brake rotors were weighed on a Mettler Toledo scale with a 3100 g capacity and a 10 mg resolution (model no.: PB3002-S). The brake pads were weighed on a Scientech laboratory scale set to a 200 g capacity and a 1.0 mg resolution (model no.: SA 210D).

Optical microscopy was performed on each sample before and after bedding, and after each application of the wear test procedure at three different magnifications for a number of locations on the surface of each sample. Images from the optical microscopy were captured to help determine possible wear mechanisms which might relate back to differences in measured wear rates between samples. Optical microscopy was conducted using a Leica Wild M3C Stereozoom Microscope and images were captured using a Samsung Digimax A7 7.0 MP digital camera.

4.3.1. Bedding test procedure

The green mu characteristic, burnish, and characteristic value sections, comprising the bedding sections of the SAE standard: *J2522: Dynamometer Global Brake Effectiveness* [43], were used to create the bedding test procedure run on the experiment apparatus. Five parameters were specified for the bedding test procedure: brake rotor rotational velocity, brake rotor initial surface temperature, brake rotor surface temperature increase, brake pressure and number of brake applications. The bedding test procedure was structured such that the values for each parameter were held constant across all test specimen groups (see Appendix B.2: Bedding test procedure).

4.3.1.1. Rotational velocity specification

SAE J2522 specifies each snub of the three bedding sections to take place from an initial brake velocity of 80 kph to a final brake velocity of 30 kph; however, since energy equivalent inertia simulation was used for the bedding test procedure, the electric motor was required to maintain a constant brake velocity during the brake application. Therefore, a fixed brake velocity equivalent to 80 kph was selected. This resulted in a brake rotor rotational velocity of 836 rpm based upon a front tire rolling radius of 254.0 mm according to equation 4.1:

$$\omega_{brake} = \frac{80kph}{2\pi R_{ft}} \quad (4.1)$$

4.3.1.2. Temperature specifications

The temperature parameter consisted of an initial rotor surface temperature and a rotor surface temperature increase specification. The initial rotor surface temperature is a direct adaptation from SAE J2522; the brake application would only occur if the rotor surface was below this initial temperature. The brake rotor surface temperature increase was a result of the use of energy equivalent inertia simulation.

The initial rotor surface temperature was determined during preliminary trials of the bedding test procedure. It was believed that the brake pad temperature should be cycled about the specified temperature at which the peak coefficient of friction occurs. For the Wilwood PolyMatrix A brake pad compound selected for the current study, the peak coefficient of friction occurs between 400 and 500 °F (see Figure 4.7). Preliminary trials of the bedding procedure revealed that, with an initial rotor temperature of 340 °F, the peak pad temperature after each brake application would range between 400 and 500 °F. Thus, for the bedding test procedure, the initial rotor temperature was specified at 340 °F.

The brake rotor surface temperature increase was estimated using equations based on those presented in, *Brake Design and Safety*, by Rudolf Limpert [47], to estimate the brake rotor surface temperature during a single stop from simplified temperature analysis (see Appendix C.2: Brake rotor surface temperature). This simplified temperature analysis required the vehicle

deceleration to be known. Several equations were developed to estimate the deceleration for any vehicle application based upon the various brake system components under an applied brake pressure. This vehicle deceleration calculation was subjected to braking limits imposed by the tire coefficient of friction and vehicle longitudinal weight transfer (see Appendix C.1: Vehicle deceleration). Combining calculations, the pressure specification for each cycle of the bedding test procedure was used to estimate the deceleration of a lightweight racecar, and in turn, the deceleration was used to estimate the brake rotor surface temperature increase. The surface temperature increase was therefore a function of the pressure specification.

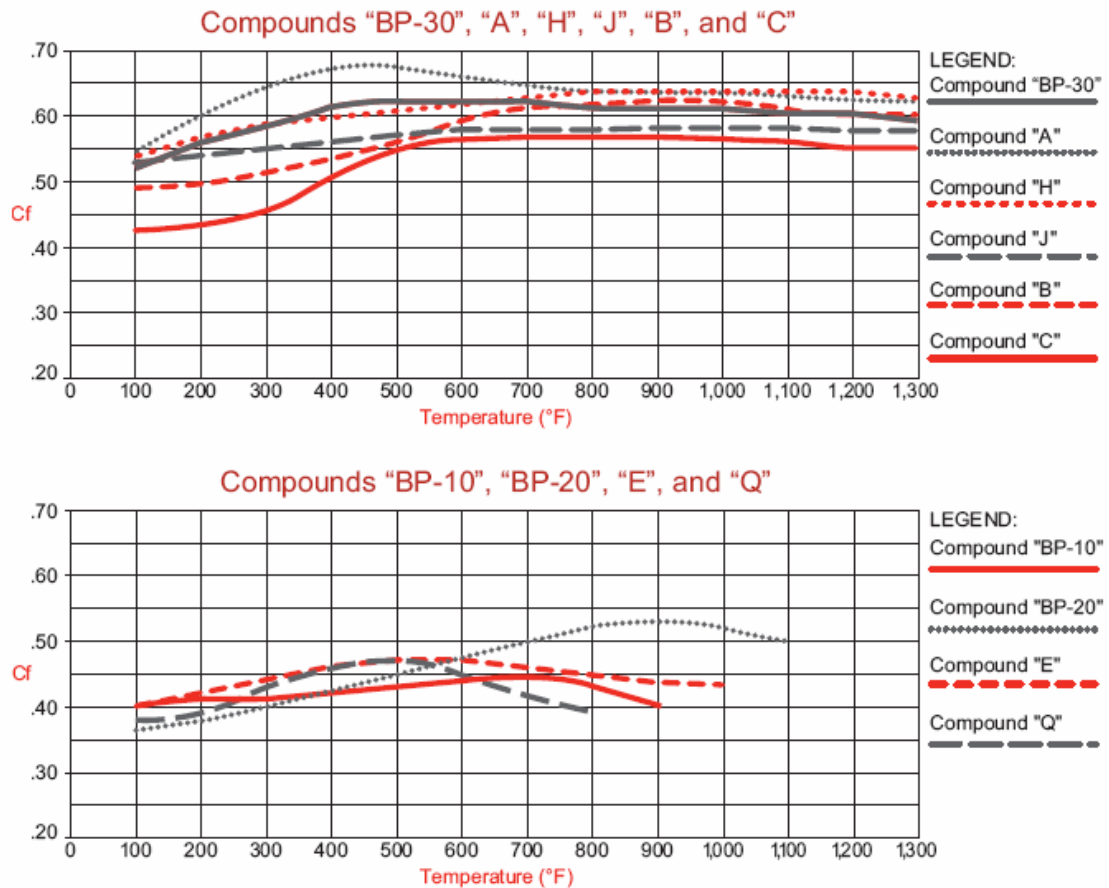


Figure 4.7: Wilwood brake pad compound coefficient of friction versus temperature profiles [50]

4.3.1.3. Pressure specification

Although SAE J2522 was designed as a generalized standard to cover a wide range of vehicle applications, it was believed that a lightweight racecar might not be able to generate the brake pressures specified in SAE J2522. Therefore, an effort was undertaken to scale the brake pressure specifications to realistic values for any vehicle application.

Several equations were developed to estimate the deceleration for any vehicle application based upon the various brake system components under an applied brake pressure. This vehicle deceleration calculation was subjected to braking limits imposed by the tire coefficient of friction and vehicle longitudinal weight transfer (see Appendix C.1: Vehicle deceleration). From this derivation, a single equation was formed to estimate the maximum brake pressure for a given vehicle application based upon the maximum vehicle deceleration being equated to the tire coefficient of friction value:

$$P_{f-\max} = \frac{4m\mu_t}{\pi \left[\mu_{fb} N_{fc} N_{fp} R_{fe} R_{ft} D_{fp}^2 + \mu_{rb} N_{rc} N_{rp} R_{re} R_{rt} D_{rp}^2 \left(\frac{100}{\%_{fb}} - 1 \right) \right]} \quad (4.2)$$

Equation 4.2 can be slightly simplified using parameters values typical to a lightweight racecar brake system:

$$P_{f-\max} = \frac{2m\mu_t}{\pi\mu_b \left[N_{fp} R_{fe} R_{ft} D_{fp}^2 + N_{rp} R_{re} R_{rt} D_{rp}^2 \left(\frac{100}{\%_{fb}} - 1 \right) \right]} \quad (4.3)$$

Where:

- $\mu_{fb} = \mu_{rb} = \mu_b$
- $N_{fc} = N_{rc} = 2$

According to equation 4.3, the lightweight racecar used for verification testing had an estimated maximum front brake pressure of 1.63 MPa, for the following brake system parameters values:

- $m = 306.2 \text{ kg}$
- $\mu_t = 1.35$

- $\mu_b = 0.68$
- $N_{fp} = N_{rp} = 2$
- $R_{fe} = R_{re} = 97.1$ mm
- $R_{ft} = R_{rt} = 248.7$ mm
- $D_{fp} = D_{rp} = 44.5$ mm
- $\%f_b = 66.4$ percent

The brake pressure specifications in *SAE J2522* were modified such that the maximum specification of the three bedding sections, 5.10 MPa, was equated to the estimated maximum front brake pressure of the lightweight racecar, 1.63 MPa. The remaining pressure specifications were scaled by the ratio of: 1.63 to 5.10.

4.3.1.4. Brake application number specification

The number of brake applications parameter was determined by the cumulative number of snubs, 100, across the three *SAE J2522* bedding sections (see Appendix B.1: *SAE J2522*).

4.3.2. Wear test procedure

The ASTM International standard, *G99-05: Standard Test Method for Wear Testing with a Pin-on-Disk Apparatus* [28], along with the SAE standard, *J2522: Dynamometer Global Brake Effectiveness* [43], were used to create the wear test procedure run on the experiment apparatus. Five parameters were specified for the wear test procedure: brake rotor rotational velocity, brake rotor initial surface temperature, brake rotor surface temperature increase, brake pressure and number of brake applications. The wear test procedure was structured such that the brake pressure parameter was varied across the three test specimen groups, while rotational velocity parameter was held constant.

4.3.2.1. Rotational velocity specification

The brake rotor rotational velocity parameter was set at 836 rpm, consistent with the bedding test procedure (see Section 4.3.1.1: Rotational velocity specification).

4.3.2.2. Temperature specifications

The temperature parameter consisted of an initial rotor surface temperature and a rotor surface temperature increase specification. The initial rotor surface temperature is a direct adaptation from *SAE J2522*; the brake application would only occur if the rotor surface was below this initial temperature. The brake rotor surface temperature increase was a result of the use of energy equivalent inertia simulation.

The initial rotor surface temperature was increased over the initial temperature specified for the bedding test procedure. During the bedding tests, it was observed that an initial rotor temperature of 340 °F was not high enough to fully cycle the brake pad temperature between 400 and 500 °F, believed to be necessary to obtain the maximum coefficient of friction from the pad compound. Thus, the initial rotor surface temperature was set at 400 °F to ensure the pad temperature cycled fully between 400 and 500 °F.

The brake rotor surface temperature increase was estimated using the same method outlined for the bedding test procedure, that is, the pressure specification for each cycle of the bedding test procedure was used to estimate the deceleration of a lightweight racecar, and in turn, the deceleration was used to estimate the brake rotor surface temperature increase (see Section 4.3.1.2: Temperature specifications). The brake rotor surface temperature increase parameter was specified as 46.5, 56.9, and 65.7 degree Fahrenheit for the three test specimen groups 1, 2 and 3, respectively. The surface temperature increase was therefore a function of the pressure specification.

4.3.2.3. Pressure specification

The brake pressure parameter was specified as 1.63, 3.26, and 2.44 MPa for the three test specimen groups 1, 2 and 3, respectively. The brake pressure parameter for test specimen group 1 was determined from the estimated maximum front brake pressure for a lightweight racecar (see Section 4.3.1.3: Pressure specification). The brake pressure parameter for test specimen groups 2 and 3 were scaled values of the brake pressure parameter for test specimen group one by factors of 2.0 and 1.5, respectively. It was believed that the specifying the brake

pressure parameter based on a realistic value for a particular vehicle application would allow predictions to be made of the wear rate measurement to the *real world*; however, this idea required balancing against the need to produce measurable mass loss over short wear test procedure durations. After test specimen group 1 had been exercised through all wear test procedure repetitions at the specified brake pressure parameter of 1.63 MPa, it was observed that the wear rate, and thus the mass loss, was not very significant in comparison to the readability of the scale used to weigh the brake rotors. Thus, the brake pressure parameter for test specimen groups 2 and 3 were increased in hopes of producing more significant mass loss.

4.3.2.4. Brake application number specification

The number of brake applications, or *cycles*, per repetition was varied for test specimen group 1 to investigate possible non-linearity in the mass loss, and therefore wear rate, during brake applications following the bedding test procedure. The number of cycles per repetition was held constant across test specimen groups 2 and 3; however, each test specimen group had been subjected to the same *total* number of cycles by the conclusion of all wear test procedure repetitions (see Table 4.1). If a particular repetition contained more than 100 cycles, the repetition would be conducted in sets of 100 cycles with a 30 to 60 minute break between sets.

Table 4.1: Number of brake applications per wear test procedure repetition for the three test specimen groups

Test Specimen Group →	1	2	3
Repetition 1	25	300	300
Repetition 2	25	300	300
Repetition 3	50	300	300
Repetition 4	100	300	300
Repetition 5	100	--	--
Repetition 6	100	--	--
Repetition 7	400	--	--
Repetition 8	400	--	--
Total Brake Applications →	1200	1200	1200

5. RESULTS AND DISCUSSION

5.1. Results

The results obtained from the inertia laboratory brake dynamometer testing to verify the logic of the wear simulation and the functionality of the dynamometer are presented for the five brake material test sets. The results are organized into experimental apparatus test data, mass loss, wear rate, and optical microscopy sections and include the results from both bedding and wear procedures. The experimental apparatus test data section presents the data collected from the dynamometer including the sliding distance and coefficient of friction results. The mass loss section presents the data collected from the mass measurement devices, while the wear rate section presents the results calculated from the sliding distance and mass loss data. The optical microscopy section presents the images of the brake rotor visible surface wear progression.

5.1.1. Experimental apparatus test data

5.1.1.1. Bedding procedure

The data obtained during the bedding portion of the dynamometer testing, specifically the coefficient of friction, and brake rotor surface temperature maximum and minimum, for control test specimen 1 is shown in Figure 5.1, where the green mu characteristic, burnish, and characteristic value sections have been labeled.

Figure 5.1 shows the number of brake applications, or cycles, for each of the three bedding procedure sections: 30 for the green mu characteristic, 64 for the burnish and 6 for the characteristic value sections totally 100 cycles in all. The initial rotor surface temperature, labeled *Rotor Temp. Min.*, is maintained for each cycle at the specified value of 340 °F while the rotor surface temperature increase, and therefore final rotor surface temperature, labeled *Rotor Temp. Max.*, varies in response to the brake application pressure (not shown). During the green mu

characteristic section, the final rotor surface temperature remains relatively constant, once the initial rotor surface temperature is reached at approximately cycle number 7, due to the constant brake application pressure for each of the 30 cycles. During the burnish section, the final rotor surface temperature variation is noticeably larger due to the large variation in brake application pressure for each of the 64 cycles. Once the bedding procedure reaches the characteristic value section, where the brake application pressure is once again constant for each cycle, the final rotor surface temperature variation decreases. The average coefficient of friction for each cycle, labeled *Average μ* , initially increases steadily for the first 5 cycles at which point it sharply peaks, decreases slightly and goes through a broader peak before decreasing to a relative steady value of approximately 0.43. The cycle-to-cycle variation in the coefficient during the green mu characteristic and characteristic value sections is minimal while the variation in the coefficient during the burnish section is noticeably larger. This difference in variation is again due to the brake application pressure variation for each cycle and results from the sensitivity of the coefficient of friction to changes in brake application pressure.

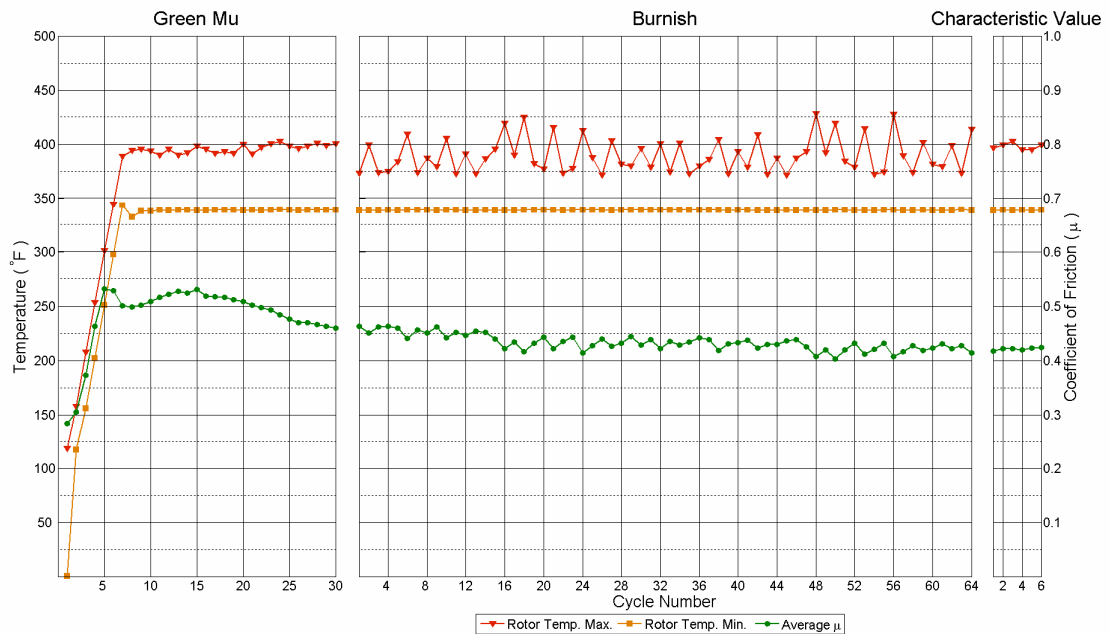


Figure 5.1: Bedding test data for control test specimen 1

Although the data acquired during the bedding portion of the dynamometer testing is significant in demonstrating the capabilities of the dynamometer, it is considered more of secondary importance for the current study, which does not use this data directly, but manipulates select portions to help determine the wear rates of each test specimen during the bedding portion of the dynamometer testing. The data for the remaining test specimens is contained in Appendix G.1: Bedding test procedure.

5.1.1.2. Wear procedure

The data obtained during the wear portion of the dynamometer testing, specifically the coefficient of friction, brake rotor surface temperature, and brake pressure, for control test specimen 1 is shown in Figure 5.2

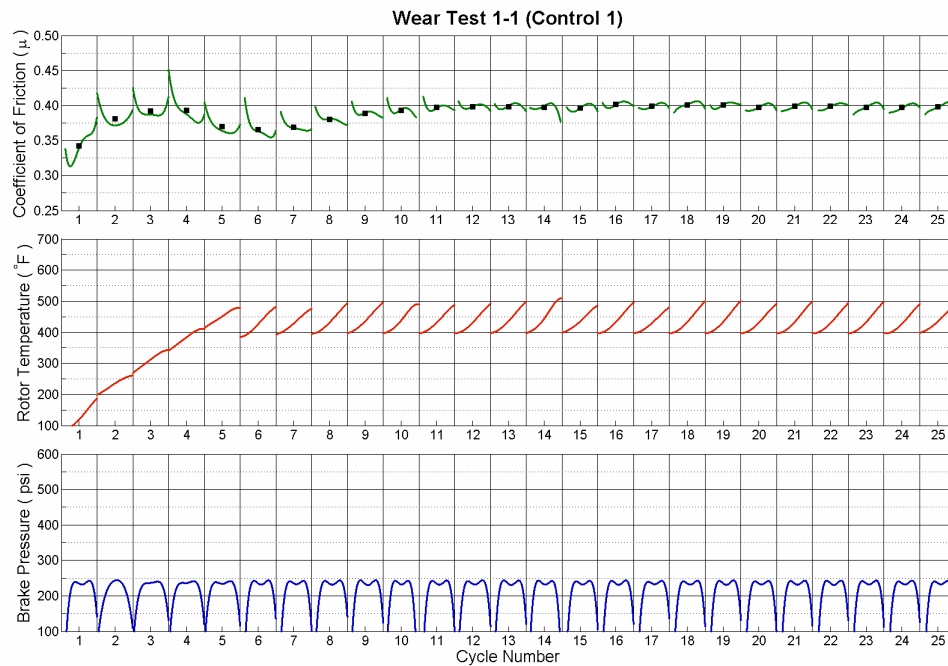


Figure 5.2: Wear test data for control test specimen 1, repetition 1

Figure 5.2 shows the 25 cycles of the first wear repetition for control test specimen 1. The coefficient of friction profile (green trace), along with the average value (black rectangle), is shown for each cycle. The rotor surface temperature profile (red trace) and the brake application

pressure (blue trace) is also shown. The average coefficient of friction initially increases for the first 3 cycles at which point it peaks, decreases slightly, and steadily increases to a steady value of approximately 0.40. The rotor surface temperature profile is plotted only during the brake application; the cool-down of the rotor surface to the initial temperature is not shown. The initial rotor surface temperature is maintained for each cycle at the specified value of 400 °F, while the variation in the rotor surface temperature increase is relatively minimal due to the constant brake application pressure for each cycle, which is maintained at the specified value of 1.63 MPa (236 psi).

Although the data acquired during the wear portion of the dynamometer testing is significant in demonstrating the capabilities of the dynamometer, it is considered more of secondary importance for the current study, which does not use this data directly, but manipulates select portions to help determine the wear rates of each test specimen during the wear portion of the dynamometer testing. The data for the remaining test specimens is contained in Appendix G.2: Wear test procedure.

5.1.1.3. Sliding distance

Although each test specimen group had been subjected to the same *total* number of cycles by the conclusion of all wear test procedure repetitions, differences in sliding distance between test specimen groups occurred (see Table 5.1). Increases in sliding distance were related to increases in brake application pressure due to the hardware, software, and control strategy used to operate the brake actuator. The brake application would only occur if the rotor surface was below a specified initial temperature and if the rotor surface had not yet met or exceeded the specified temperature increase. The Exergen IRTc.3x non-contact, infrared thermocouple was used to measure the rotor surface temperature in conjunction with a USB-9211A thermocouple DAQ unit, which could only sample across all four channels simultaneously at 2.0 Hz. This sample rate was not high enough to capture a sufficient number of data points during a brake application, where the rate of temperature increase was very large. Changes in the brake pressure as a response to changes in the rotor surface temperature as related to the temperature increase specification could only be made every half-second at best. This resulted

in the rotor surface temperature consistently overshooting the target temperature increase because the brake pressure was still being applied, and since the rotor surface temperature increase rate is related to the brake application pressure, an increase in pressure increased the overshoot of the rotor surface temperature. The amount of overshoot was inconsistent, varying for each brake application but, for example, the final rotor surface temperature was approximately 11 % greater than expected at a brake application pressure of 1.63 MPa. Since the brake pressure was maintained for longer durations as the pressure increased, the calculated sliding distance subsequently increased (see Section 3.8.2: Sliding distance). Therefore, it was expected that test specimen group 1 would have the shortest sliding distance, while test specimen group 2 would have the longest sliding distance, and test specimen group 3 would be somewhere in between based upon their respective brake application pressures.

Table 5.1: Individual test specimen sliding distance (km) verses test procedure

Test Specimen → Test Procedure ↓	Control 1	Treated 1	Control 2	Treated 2	Treated 3
Bedding	3.20	3.22	4.68	3.35	4.18
Repetition 1	0.73	0.69	11.08	10.45	9.42
Repetition 2	0.70	0.70	10.96	10.66	10.61
Repetition 3	1.50	1.43	11.17	10.82	9.62
Repetition 4	2.93	2.87	11.16	10.78	8.68
Repetition 5	2.99	2.87	--	--	--
Repetition 6	3.03	2.99	--	--	--
Repetition 7	12.03	11.79	--	--	--
Repetition 8	12.06	11.75	--	--	--
Totals →	39.17	38.31	49.05	46.06	42.51

5.1.1.4. Coefficient of friction

The average coefficient of friction from the experimental apparatus test data for both bedding and wear procedures is shown in Figure 5.3 against sliding distance. The highest average coefficient of friction for all five test specimens occurs during the bedding test procedure and immediately drops to the lowest average value during the first wear test procedure repetition. Overall, the average value increases during the remainder of the repetitions for all five samples.

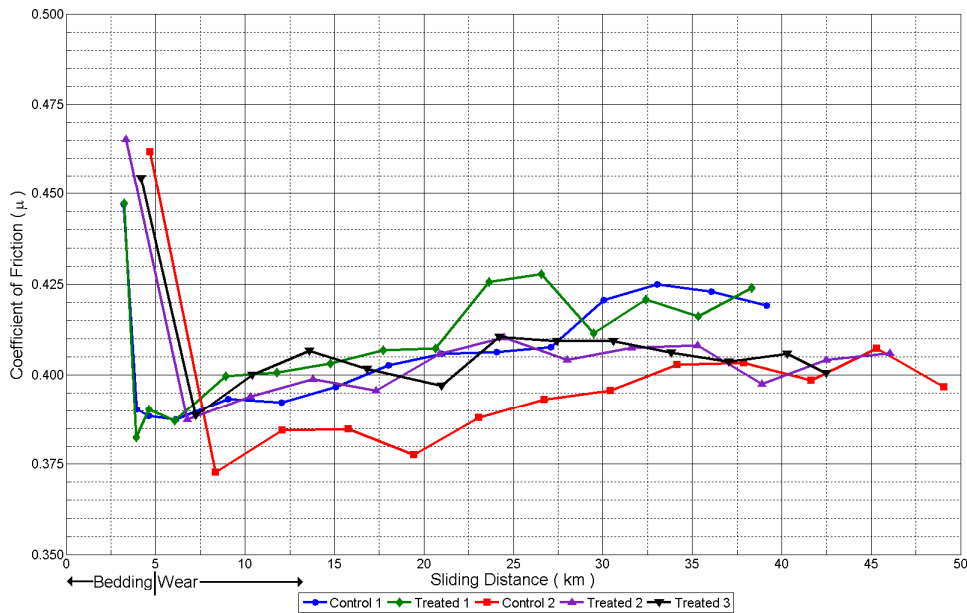


Figure 5.3: Average coefficient of friction verses sliding distance (km)

5.1.2. Mass loss

5.1.2.1. Rotor

The cumulative brake rotor mass loss, as a percentage of the initial rotor mass, during the bedding and wear test procedures for each test specimen is shown in Figure 5.4 and Table 5.2 (see Appendix G.3: Brake rotor and pad mass loss, for full listing of individual and cumulative brake rotor mass loss expressed in grams). The progression of rotor wear across the bedding and wear test procedures is shown in Figure 5.5, using treated test specimen 3 as an example.

Based on to Figure 5.4 and Table 5.2, the treated test specimens do not appear to hold a significant advantage in terms of rotor mass loss over their control test specimen counterparts, although the treated test specimens do show less cumulative rotor mass loss for the majority of the sliding distance. At approximately 35 km of sliding distance, however, test specimen group 1 shows equal cumulative rotor mass losses, with the treated test specimen exhibiting a slightly higher cumulative rotor mass loss for increasing sliding distance beyond 35 km. Treated test specimen 3 initially shows less cumulative rotor mass loss than control test specimen 1 even

though treated test specimen 3 was exposed to brake application pressures 50 percent greater than those applied to control test specimen 1, although this relation disappears beyond approximately 16 km of sliding distance.

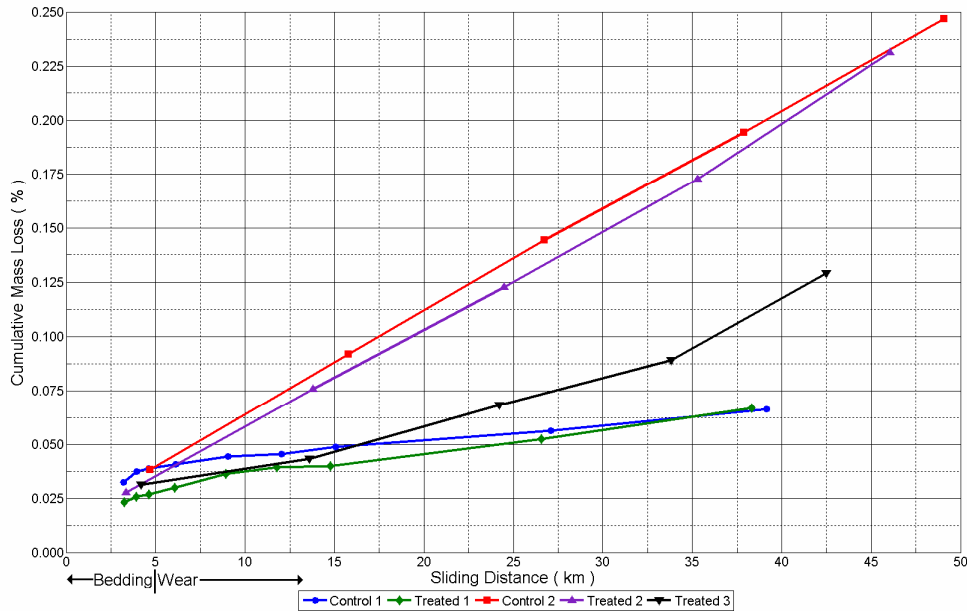


Figure 5.4: Cumulative brake rotor mass loss (%) versus sliding distance (km)

Table 5.2: Cumulative brake rotor mass loss (%)

Test Procedure	Control 1	Treated 1	Control 2	Treated 2	Treated 3
Bedding	0.033	0.023	*0.038*	0.028	0.031
Repetition 1	0.038	0.026	0.092	0.076	0.043
Repetition 2	0.039	0.027	0.144	0.123	0.068
Repetition 3	0.041	0.030	0.194	0.173	0.089
Repetition 4	*0.044*	*0.036*	0.247	0.231	*0.129*
Repetition 5	0.046	0.039	--	--	--
Repetition 6	0.049	0.040	--	--	--
Repetition 7	0.056	0.052	--	--	--
Repetition 8	0.066	0.067	--	--	--

The greatest rotor mass loss during the bedding test procedure occurred in the two control test specimens with control test specimen 2 having the higher loss. Although the three treated test specimens had the least rotor mass loss, treated test specimen 3 had a comparable mass loss to control test specimen 1.

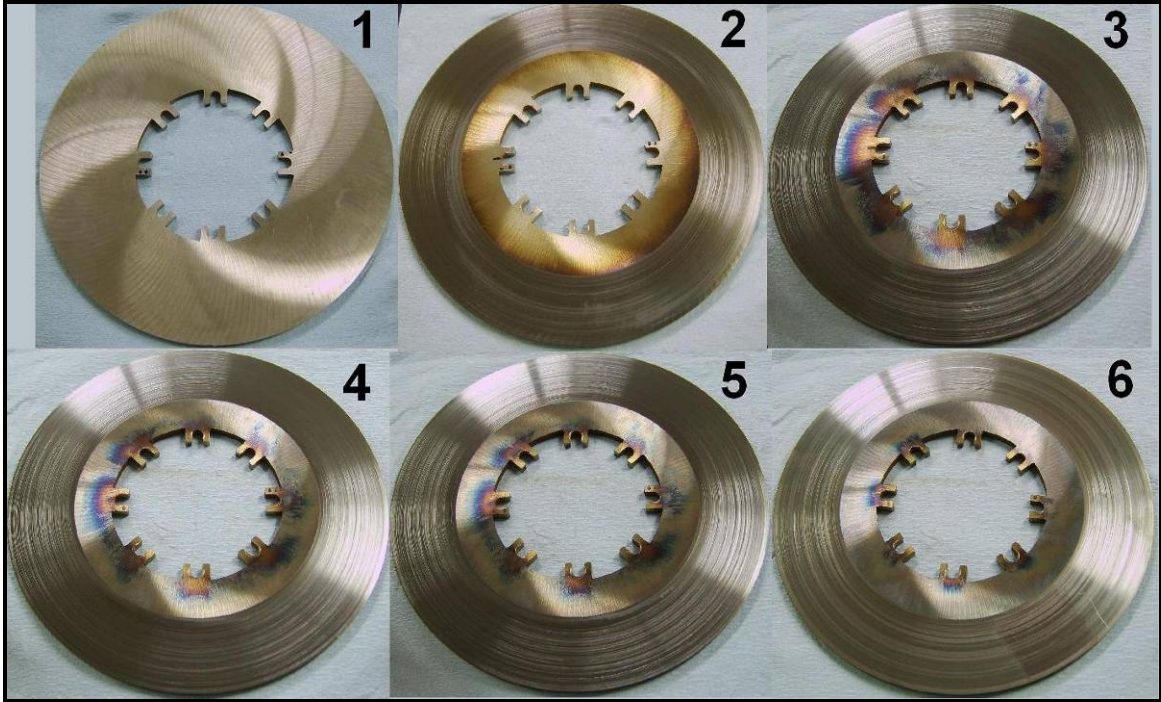


Figure 5.5: Progression of brake rotor wear for treated test specimen 3

The number of cycles per repetition was varied during the wear test procedure for test specimen group 1 to investigate possible non-linearity in the mass loss during brake applications following the bedding test procedure (see Table 4.1). The data shown in Figure 5.4 and Table 5.2 does not clearly show significant differences in rotor mass loss during repetitions 1 through 3 for test specimen group 1. The majority of the rotor mass loss for test specimen group 1 occurred during the bedding test procedure and therefore it is believed that any non-linear results would occur from the initial brake applications during the bedding test procedure.

Initial rotor mass measurements from the wear test procedure repetition number 4 for test specimen group 1 were rendered invalid due to erroneous results stemming from inconsistencies in measuring the rotor mass. It was discovered after repetition number 4 that the scale used to measure the rotor mass required an adjustment which changed the rotor mass measurement. Since the rotor mass loss is calculated between mass measurements, the scale adjustment rendered the measurement taken after repetition number 4 irrelevant to the measurement after repetition number 3, and therefore no rotor mass loss could be accurately established.

Therefore, the rotor mass loss from repetition number 4 for test specimen group 1 was linearly extrapolated using the rotor mass loss from repetitions 2 and 3.

5.1.2.2. Pad

The cumulative brake pad mass loss, as a percentage of the initial pad mass, during the bedding and wear test procedures for each test specimen is shown in Figure 5.6 and

Table 5.3 (see Appendix G.3: Brake rotor and pad mass loss, for full listing of individual and cumulative brake pad mass loss expressed in grams).

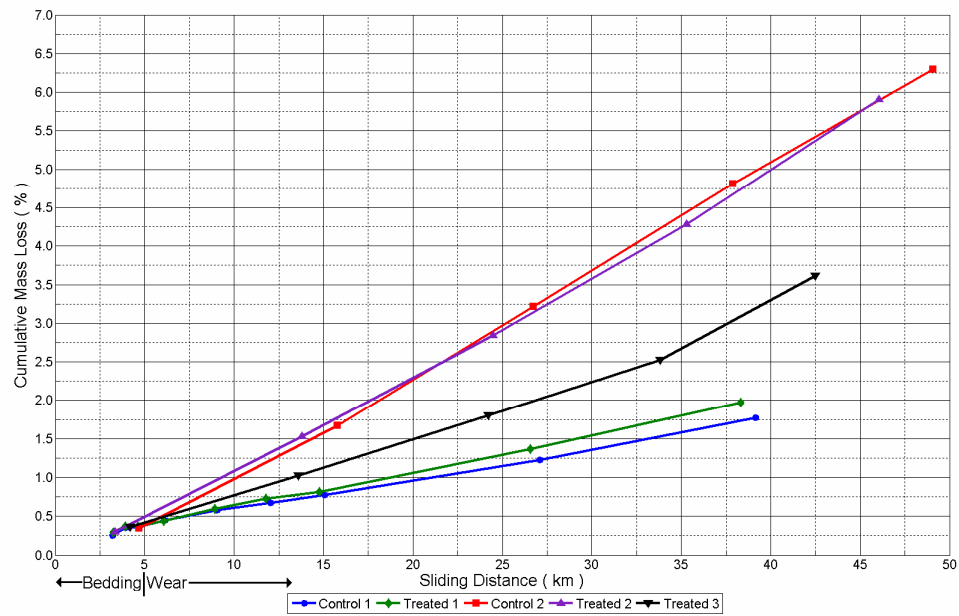


Figure 5.6: Cumulative brake pad mass loss (%) verses sliding distance (km)

Table 5.3: Cumulative brake pad mass loss (%)

Test Procedure	Control 1	Treated 1	Control 2	Treated 2	Treated 3
Bedding	0.251	0.291	0.347	0.303	0.363
Repetition 1	0.358	0.368	1.672	1.531	1.025
Repetition 2	0.364	0.372	3.219	2.843	1.797
Repetition 3	0.449	0.443	4.813	4.278	2.523
Repetition 4	0.579	0.599	6.296	5.906	*3.611*
Repetition 5	0.675	0.728	--	--	--
Repetition 6	0.777	0.815	--	--	--
Repetition 7	1.227	1.366	--	--	--
Repetition 8	1.767	1.974	--	--	--

Based on Figure 5.6 and

Table 5.3, the treated test specimens do not appear to hold a significant advantage in terms of pad mass loss over their control test specimen counterparts. The pad mass loss is greater for the treated test specimen 1 compared to the control test specimen 1, while no clear relationship can be observed for test specimen group 2. Initially, the treated test specimen 2 shows greater pad mass loss compared to control test specimen 2 until approximately 22 km of sliding distance where the relation is reversed. At approximately 44 km of sliding distance treated test specimen 2 once again shows greater pad mass loss compared to control test specimen 2. The pad mass loss for treated test specimen 3 lies between that of test specimen groups 1 and 2.

The greatest pad mass loss during the bedding test procedure occurred in the three treated test specimens, with the exception of control test specimen 2, with treated test specimen 3 having the highest measured mass loss.

The number of cycles per repetition was varied during the wear test procedure for test specimen group 1 to investigate possible non-linearity in the mass loss during brake applications following the bedding test procedure (see Table 4.1). The data shown in Figure 5.6 and

Table 5.3 shows a significant difference, almost an abnormality, in pad mass loss during repetition number 2 for test specimen group 1. No reason can be given at this time to explain the significant difference.

Unexpected brake pad mass increases were measured between wear test procedure repetitions when the pads were not installed in the caliper but set aside in plastic storage bags for test specimen groups 2 and 3 (the pads from test specimen group 1 were not measured prior to each repetition, only after). The average pad mass increase was 38 mg or approximately 0.04 percent of the total pad mass. It is believed that moisture absorption from the environment could have caused the pad mass increases.

5.1.3. Wear rate

5.1.3.1. Rotor

The brake rotor wear rates during the bedding and wear test procedures for each test specimen are shown in Figure 5.7 and Table 5.4.

The greatest rotor wear rate during the bedding test procedure occurred in control test specimen 1; however, control test specimen 2 shows a lower rotor wear rate, less than that of the treated test specimen 2 and 3, with the lowest rotor wear rate occurring in treated test specimen 1.

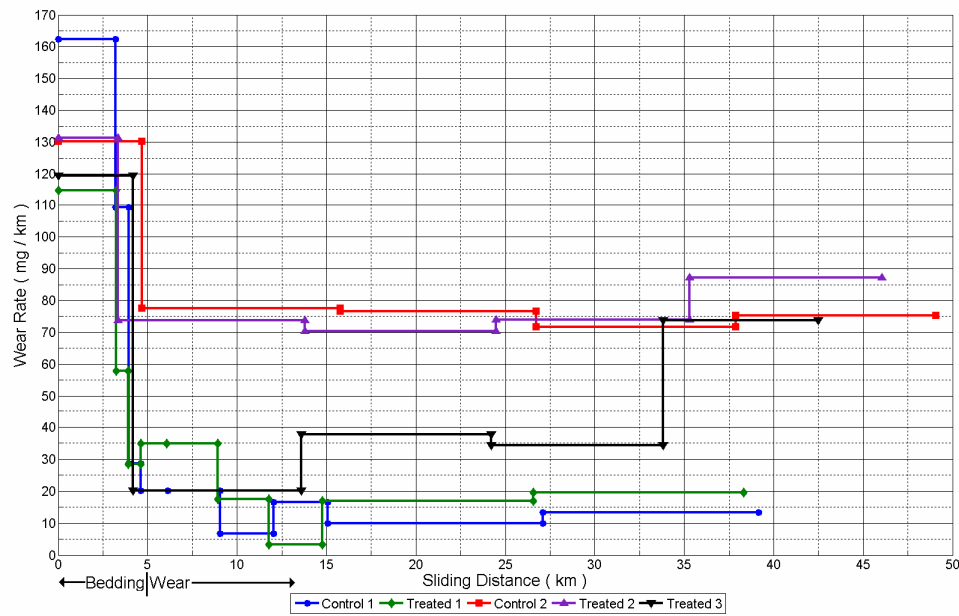


Figure 5.7: Brake rotor wear rate (mg / km) versus sliding distance (km)

Table 5.4: Brake rotor wear rate (mg / km)

Test Procedure	Control 1	Treated 1	Control 2	Treated 2	Treated 3
Bedding	162	115	*130*	131	120
Repetition 1	109	57.9	77.6	73.7	20.2
Repetition 2	28.7	28.4	76.6	70.3	37.7
Repetition 3	20.1	34.9	71.6	73.9	34.3
Repetition 4	*20.1*	*34.9*	75.2	87.2	*73.8*
Repetition 5	6.69	17.4	--	--	--
Repetition 6	16.5	3.35	--	--	--
Repetition 7	9.98	17.0	--	--	--
Repetition 8	13.3	19.6	--	--	--

The number of cycles per repetition was varied during the wear test procedure for test specimen group 1 to investigate possible non-linearity in the wear rate during brake applications following the bedding test procedure (see Table 4.1). The data shown in Figure 5.7 and Table 5.4 shows a significant decrease in rotor wear rate between wear test procedure repetitions 1 and 2. This decrease is probably a continuation of the decrease in rotor wear rate between the bedding and wear test procedures. The remaining repetitions do not show much variation compared to the decrease in rotor wear rate between repetitions 1 and 2.

As previously mentioned, the initial rotor mass measurements from the wear test procedure repetition number 4 for test specimen group 1 were rendered invalid due to erroneous results stemming from inconsistencies in measuring the rotor mass. The rotor mass loss from repetition number 4 for test specimen group 1 was linearly extrapolated using the rotor mass loss from repetitions 2 and 3 resulting in the same value for wear rate between repetitions 3 and 4 for test specimen group 1.

5.1.3.2. Pad

The brake pad wear rates during the bedding and wear test procedures for each test specimen are shown in Figure 5.8 and Table 5.5.

The greatest pad wear rate during the bedding test procedure occurred in the three treated test specimens. The lowest pad wear rate during the bedding test procedure occurred in control test specimen 2 which, along with treated test specimen 3, provides evidence to the relationship that a greater number of cycles of the bedding test procedure will lower the wear rate. Although the difference in wear rates between the three treated test specimens appears to be insignificant, the difference in wear rates between the two control test specimens appears to be significant; however the difference in wear rates between the two control test specimens is still less than the difference in wear rates between the control and treated test specimen groups.

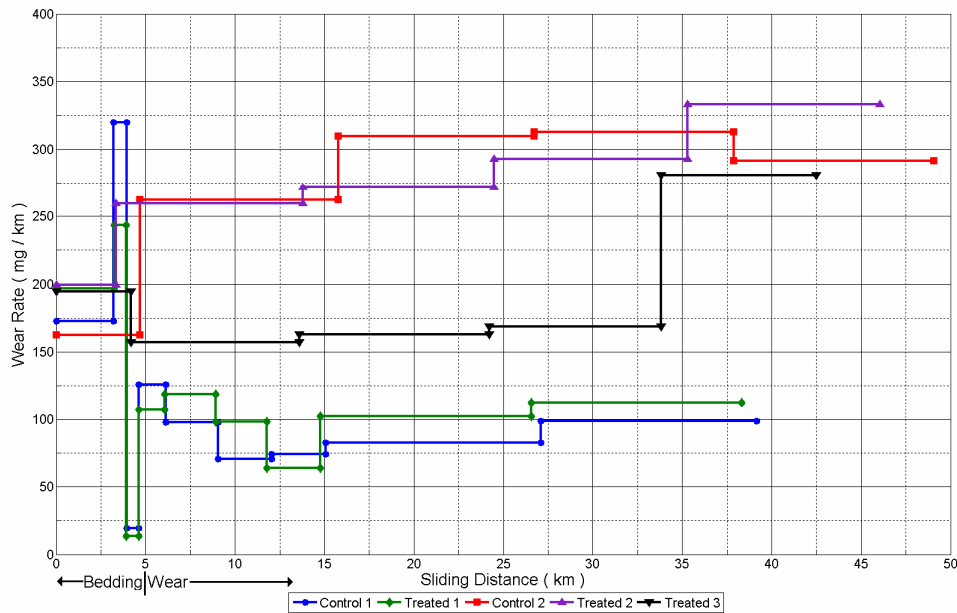


Figure 5.8: Brake pad wear rate (mg / km) verses sliding distance (km)

Table 5.5: Brake pad wear rate (mg / km)

Test Procedure	Control 1	Treated 1	Control 2	Treated 2	Treated 3
Bedding	173	197	163	199	194
Repetition 1	320	243	262	259	157
Repetition 2	19.2	13.5	309	271	163
Repetition 3	126	107	313	293	169
Repetition 4	97.8	119	291	333	*281*
Repetition 5	70.4	98.1	--	--	--
Repetition 6	74.0	63.6	--	--	--
Repetition 7	82.5	102	--	--	--
Repetition 8	98.6	113	--	--	--

The number of cycles per repetition was varied during the wear test procedure for test specimen group 1 to investigate possible non-linearity in the wear rate during brake applications following the bedding test procedure (see Table 4.1). The data shown in Figure 5.8 and Table 5.5 shows a significant decrease in pad wear rate after wear test procedure repetition number 1, which actually is an increase over the wear rate during the bedding test procedure. The remaining repetitions do not show much variation compared to the decrease in rotor wear rate after repetition number 1.

5.1.4. Optical microscopy

The brake rotor surface progression captured using optical microscopy across the bedding and wear test procedures is shown in Figure 5.9 and Figure 5.10, using control and treated test specimen 2 as examples. Each image shown in Figure 5.9 and Figure 5.10 was captured at the same circumferential and radial location on the rotor surface. Although the circumferential location was arbitrarily chosen, the radial location was approximately at the effective radius of the rotor.

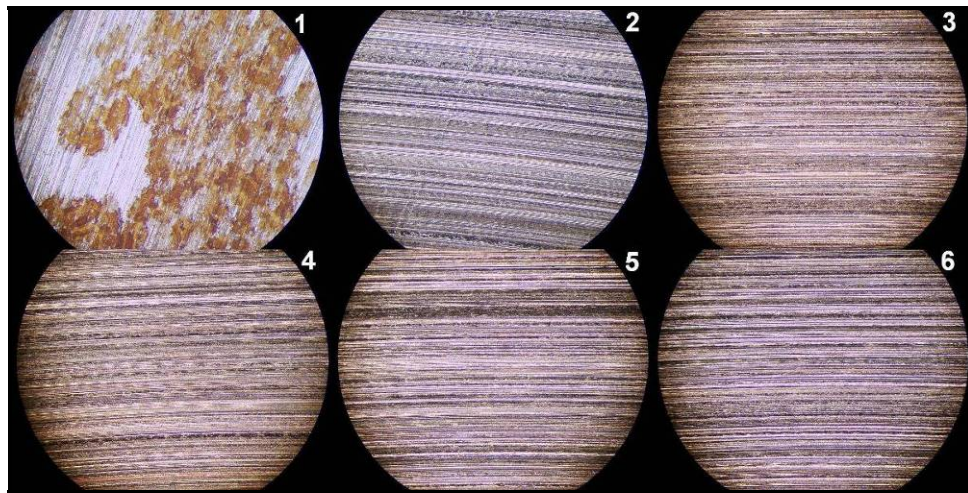


Figure 5.9: Brake rotor surface images of control test specimen 2 (magnification: 40x)

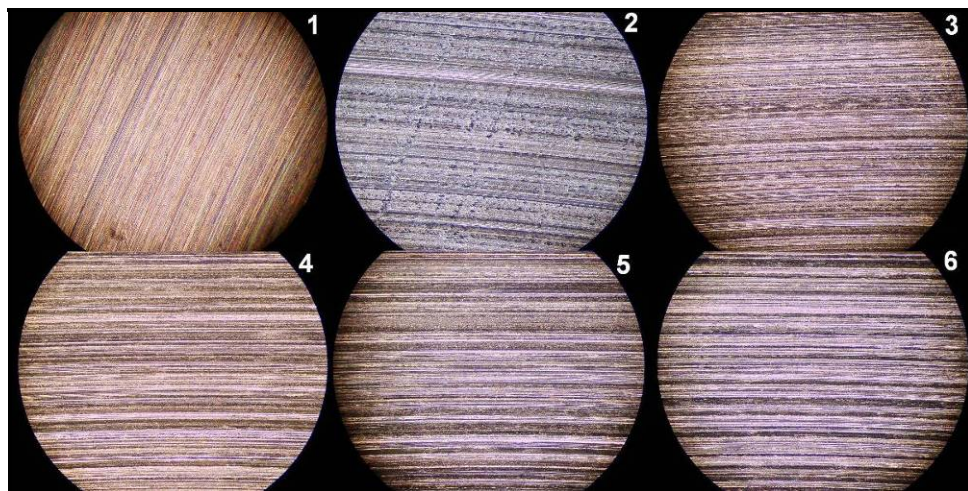


Figure 5.10: Brake rotor surface images of treated test specimen 2 (magnification: 40x)

The brake pad surface progression captured during optical microscopy across the bedding and wear test procedures is shown in Figure 5.11 and Figure 5.12, using control and treated test specimen 2 as examples. Each image shown in Figure 5.11 and Figure 5.12 was captured at the same circumferential and radial location on the rotor surface. Although the circumferential location was arbitrarily chosen, the radial location was approximately at the effective radius of the rotor.

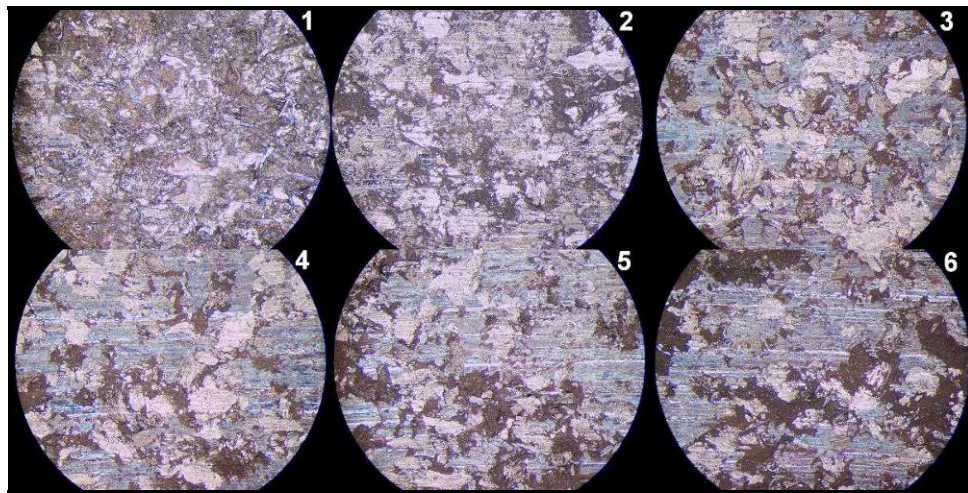


Figure 5.11: Brake pad surface images of control test specimen 2 (magnification: 40 x)

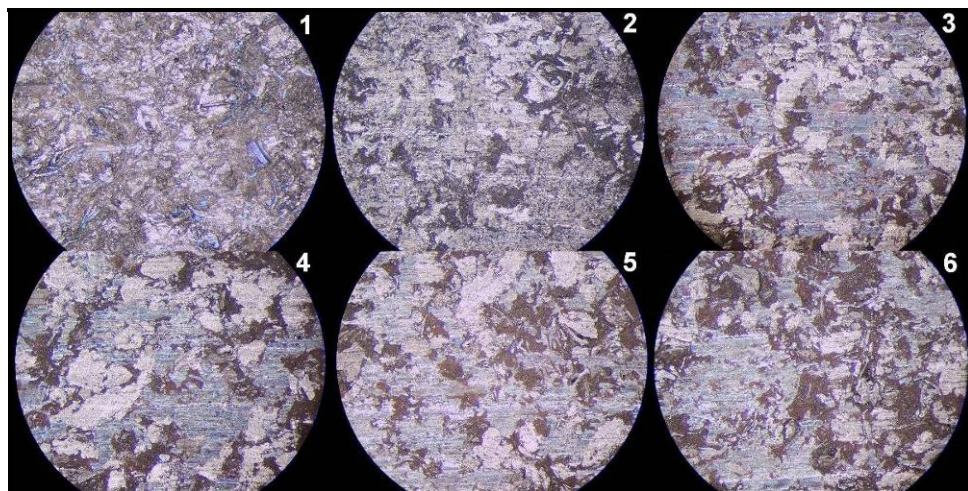


Figure 5.12: Brake pad surface images of treated test specimen 2 (magnification: 40 x)

5.2. Discussion

The discussion of the results obtained from the inertia laboratory brake dynamometer testing to verify the logic of the wear simulation and the functionality of the dynamometer are presented below for the five brake material test sets. The discussion is organized into resolved wear rates, coefficient of friction, optical microscopy and experimental apparatus failures sections. The resolved wear rates discussion examines the ability of the simulation and dynamometer to produce measurable wear rates over short test durations and across testing variations, including rotor treatment and brake application pressure variations. The coefficient of friction discussion investigates the several interesting observations made from the respective results, while the optical microscopy discussion considers the brake rotor surface progression as it relates potential differences between the control and treated test specimens. The experimental apparatus failures section discusses the several failures which occurred during dynamometer testing and the impact of each failure upon the results.

5.2.1. Resolved wear rates

One objective of the current study was to demonstrate that a wear simulation implemented on an inertia laboratory brake dynamometer had the ability to resolve differences in wear rates of brake materials. This ability depends on the capacity of the simulation to generate measurable wear rates over reasonably short test durations as limited by the resolution of the mass measurement devices. Testing was performed on five brake material test sets to verify the simulation and that the dynamometer had the ability to resolve differences in wear rates by implementing two testing variations: rotor treatment and brake application pressure.

5.2.1.1. Measurable wear rates over short test durations

The shortest test durations occurred during the initial wear repetitions of test specimen group 1, where a small number of brake applications (cycles) were specified to investigate possible non-linearity in the wear rate. For the first wear repetition, 25 cycles were specified for test specimen group 1 and the results are summarized in Table 5.6.

Table 5.6: Results for test specimen group 1, wear repetition 1

Test Specimen	Control 1	Treated 1
Brake App. Time (min)	1.44	1.35
Test Duration (min)	17.6	14.9
Sliding Distance (km)	0.73	0.69
Rotor Mass Loss (g)	0.08	0.04
Pad Mass Loss (g)	0.2343	0.1682
Rotor Wear Rate (mg / km)	109	57.9
Pad Wear Rate (mg / km)	320	243

Based on Table 5.6, wear repetition 1, consisting of 25 brake applications, resulted in approximate test durations of only 15 to 17 minutes and generated enough rotor and pad mass loss not only to register on both mass measurement devices, but to produce clearly distinct variations of the wear rates between specimens and components. Although the test duration lasted approximately 15 to 17 minutes, the brake application time lasted just under 1.5 minutes, or approximately 8.5 % of the test duration. The test duration and brake application time are not one in the same due to concerns that continuous brake applications lasting even just a couple of minutes at moderate pressure would result in a large temperature generation. Uncontrolled, the temperature generation can severely shorten component life expectancy and has the potential to influence test results and therefore the bedding and wear procedures used discrete brake applications to moderate the temperature generation.

According to the calculations performed to predict potential wear test durations based upon the experimental work of Molinari, et al. [36] in determining wear rates from disk-on-disk dry sliding tests of four samples AISI M2 tool steel (see Section 2.1.2: Generate measurable wear rates), 24 minutes of brake application time would have been required to generate 0.04 g of rotor mass loss from control test specimen 1. Likewise, 20 minutes of brake application time would have been required to generate 0.08 g of rotor mass loss from treated test specimen 1; however, the wear simulation developed for the current study resulted in much lower brake application times, a mere 6.0 and 6.8 % of the predicted brake application times, respectively. Even the test

durations, which consisted mostly of waiting for the rotor to cool down to the initial temperature specification, were shorter than the predicted brake application times. It is clear that the rotor wear rates generated in the current study are far greater than those generated by Molinari, et al., as initially expected, and believed to be a result of the sensitivity to the particular test parameters (load, sliding speed, etc.) and partially a result of the fact that the rotors were worn using two pads. For comparison, the respective test parameters for the experiment conducted by Molinari, et al. and the current study are listed in Table 5.7.

Table 5.7: Test parameters used in experimentally determining wear rates

Study	Load (kN)	Sliding Speed (m/s)	Sliding Distance (km)
Molinari, et al.	0.15	0.8	5.0
Current	2.5 to 5.1	8.5	39 to 49

5.2.1.2. Testing variations

The testing variations consisted of cryogenic and non-cryogenic (control) rotor treatments, and 1.63, 2.44, and 3.26 MPa brake application pressures. The testing variations were combined across the five brake material test sets such that each treatment was exposed to each pressure, except for the intermediate pressure where a control rotor was unavailable.

According to Figure 5.7 and Table 5.4 no clear distinction can be observed in the rotor wear rate between the control and treated test specimens for either the bedding or wear test procedures. Likewise, Figure 5.8 and Table 5.5 show no clear distinction in the pad wear rate between the control and treated test specimens for either the bedding or wear test procedures.

The brake application pressure for test specimen groups 2 and 3 were increased during the wear test procedure in hopes of producing more significant wear rates compared to test specimen group 1. According to Figure 5.7 and Table 5.4, clear differences can be observed in the rotor wear rates between pressure variations. Calculation of the average rotor wear rate during the wear test procedure, that is, the total mass loss per total sliding distance, shows the effect of increased pressure on the average rotor wear rate:

- Control test specimen 1 (1.63 MPa): 15 mg/km
- Treated test specimen 1 (1.63 MPa): 20 mg/km
- Control test specimen 2 (3.26 MPa): 75 mg/km
- Treated test specimen 2 (3.26 MPa): 76 mg/km
- Treated test specimen 3 (2.44 MPa): 41 mg/km

The calculation of the average rotor wear rate during the wear test procedure shows that doubling the brake application pressure approximately quadruples the average rotor wear rate and shows that increasing the brake application pressure by half approximately doubles the average rotor wear rate. This relationship can be approximated by equation 5.1:

$$\left(\frac{P_{bl}}{P_{bn}}\right)^2 = \left(\frac{W'_{avg-rotor1}}{W'_{avg-rotorn}}\right) \quad (5.1)$$

The calculation of the average rotor wear rate during the wear test procedure does not show significant differences between control and treated test specimens in groups 1 and 2; in fact, treated test specimen 2 had a higher average rotor wear rate compared to control test specimen 2.

As previously mentioned, Molinari, et al. [36] experimentally determined wear rates from disk-on-disk dry sliding tests of four samples AISI M2 tool steel, exposed to various combinations of quenching, tempering, and cryogenic treatments, ranging from 1.8 to 3.7 mg/km (see Section 2.1.2: Generate measurable wear rates). For comparison, the average rotor wear rate during the wear test procedure as listed above ranged from 15 to 76 mg/km , across varying brake application pressures. The wear rates generated in the current study are at least an order of magnitude greater than those generated by Molinari, et al. and, as already mentioned, the difference is likely due to the differences in test parameters (see Table 5.7).

According to Figure 5.8 and Table 5.5, clear differences can be observed in the pad wear rates between pressure variations. Calculation of the average pad wear rate during the wear test procedure, that is, the total mass loss per total sliding distance, shows the effect of increased pressure on the average pad wear rate:

- Control test specimen 1 (1.63 MPa): 93 mg/km

- Treated test specimen 1 (1.63 MPa): 105 mg/km
- Control test specimen 2 (3.26 MPa): 294 mg/km
- Treated test specimen 2 (3.26 MPa): 289 mg/km
- Treated test specimen 3 (2.44 MPa): 190 mg/km

The calculation of the average pad wear rate during the wear test procedure shows that doubling the brake application pressure approximately triples the average pad wear rate and shows that increasing the brake application pressure by half approximately doubles the average pad wear rate. This relationship can be approximated by equation 5.2:

$$\left(\frac{P_{b1}}{P_{bn}}\right)^{1.5} = \left(\frac{W'_{avg-pad1}}{W'_{avg-padn}}\right) \quad (5.2)$$

The calculation of the average pad wear rate during the wear test procedure does not show significant differences between control and treated test specimens in groups 1 and 2.

5.2.2. Coefficient of friction

Based upon the literature [15], it was expected that brake application pressure would have an inversely proportional effect on the average coefficient of friction, that is, an increase in brake application pressure would result in a decrease in the average coefficient of friction. Therefore, it was expected that test specimen group 1 (control 1 and treated 1) would have the highest average values, test specimen group 2 (control 2 and treated 2) would have the lowest average values, and test specimen group 3 (treated 3) would be somewhere in between for the wear test procedure repetitions. Although these relationships are generally true, treated test specimens 2 and 3 do not strictly adhere to these expected trends (see Figure 5.3).

Comparing Figure 4.7 and Figure 5.3, the coefficient of friction values obtained in the current study do not reach the peak value as indicated by the brake pad manufacturer, Wilwood. Many factors can influence the friction coefficient including rotor material, pad temperature, and bedding procedure. The increasing trends observed in the average coefficient during dynamometer testing may indicate that the pads were not fully bedded in, or that another unaccountable factor is in play.

An interesting observation was made concerning the coefficient of friction during wear test procedure repetitions consisting of multiple sets of 100 cycle tests, such as repetitions 7 and 8 for test specimen group 1, and each repetition for test specimen groups 2 and 3 (see Table 4.1). The coefficient of friction during the first 10 to 15 cycles for each set of 100 cycles appeared to rapidly increase, then slightly decrease before increasing again to a *steady* value for the remainder of the cycles (see Figure 5.13). This trend was consistent across all repetitions consisting of multiple sets of 100 cycle tests; however, for the first set of each repetition, the slight decrease in the coefficient of friction during the first 10 to 15 cycle *transient* stage appeared to be greater than during the following sets for the same repetition. Additionally, the coefficient of friction for the first set of 100 cycles appeared to take longer to reach a steady value than the following sets. Several possible interpretations exist to explain this coefficient of friction behavior, including a dependency of the coefficient of friction on the adjusting, or conforming, time of the pad and rotor interface each time the rotor and pads were re-installed into the experimental apparatus.

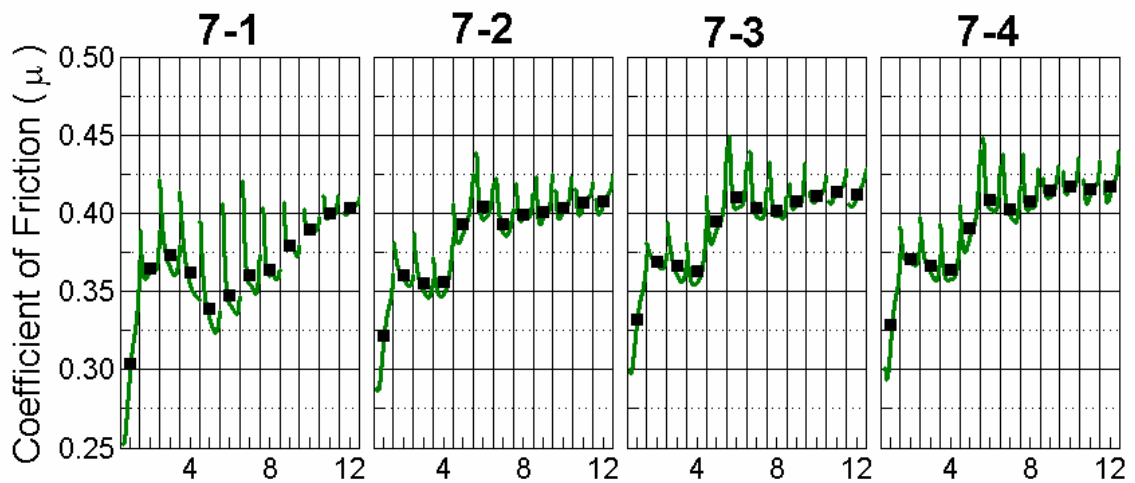


Figure 5.13: Coefficient of friction variation during the first 12 cycles for each set of 100 cycles of control test specimen 1, repetition 7

5.2.3. Optical microscopy

No clear differences were observed between the control and treated test specimen rotor surface images captured during optical microscopy when comparing Figure 5.9 and Figure 5.10. The rotor surface images do not show clear trends in wear or friction film progression; however, one can observe characteristics of abrasive wear (reflective, thin lines) and friction film (dark, thick bands) on the rotor surface. Surface corrosion and radial grooves from surface grinding are evident in the first rotor surface image (as-manufactured), but no longer appear in following images where circumferential marks are evident as a result of the rotor-pad contact interactions (see Figure 5.9 and Figure 5.10).

No clear differences were observed between the control and treated test specimen pad surface images captured during optical microscopy when comparing Figure 5.11 and Figure 5.12. The pad surface images do not show clear trends in wear or friction film progression; however, one might argue that the darker portions of the pad are occupying increasing amounts of the pad surface. No clear correlations exist between the characteristics of the pad surface and the abrasive wear and friction film observed on the rotor surface (see Figure 5.11 and Figure 5.12).

5.2.4. Experimental apparatus failures

5.2.4.1. Bedding procedure

Two of the five total test specimens experienced failures with the experimental apparatus during the bedding procedure. The first failure occurred for control test specimen 2 due to a graphics card failure in the measurement and control system computer. Approximately 40 to 45 of the required 100 cycles of the bedding test procedure had been completed when the failure occurred, which resulted in the loss of the experimental apparatus test data. Once the graphics card was replaced, all 100 cycles of the bedding test procedure were reapplied to control test specimen 2. The second failure occurred for treated test specimen 3 due to a LabVIEW data acquisition error in acquiring the analog data from the pressure and load cell transducers. Exactly 36 of the required 100 cycles of the bedding test procedure had been completed when the failure occurred. Even though the failure did not result in the loss of the experimental

apparatus test data, all 100 cycles of the bedding test procedure were reapplied to treated test specimen 3.

The experimental apparatus failure for control test specimen 2 resulted in the highest measured rotor mass loss and an increased pad mass loss. The experimental apparatus failure for treated test specimen 3 resulted in a comparable rotor mass loss to control test specimen 1, although the three treated test specimens had the least rotor mass loss, and resulted in the highest measured pad mass loss. The additional cycles applied to control test specimen 2 and treated test specimen 3 are evidenced by the increased sliding distance compared to the remaining 3 test specimens (see Table 5.1).

5.2.4.2. Wear procedure

Six of the 64 total wear repetitions across all five test specimens experienced failures with the experimental apparatus during the wear procedure. The six failures due to software issues were a result of LabVIEW data acquisition errors in acquiring the analog data from the pressure and load cell transducers. The two failures due to hardware issues occurred when the power transmission belt dislocated one of the guide flanges on the lower pulley and when the pressure transducer power supply lost power causing erroneous measurements of the brake pressure.

The four software failures occurred for the following test specimens and repetitions:

- Control test specimen 1, repetition number 5 (74 of 100 cycles)
- Treated test specimen 1, repetition number 1 (19 of 25 cycles)
- Treated test specimen 1, repetition number 7 (393 of 400 cycles)
- Treated test specimen 3, repetition number 2 (169 of 300 cycles)

After each software failure, the experimental apparatus was restarted and the number of cycles remaining for each repetition were completed.

The power transmission failure occurred for treated test specimen 1, repetition number 8 when the upper pulley was displaced rearward on the driven shaft from the belt acting against the rear guide flange of the upper pulley. In the process, the belt contacted the rear guide flange on

the lower pulley and, because of the tendency of the belt to displace rearward, eventually the rear guide flange on the lower pulley was dislocated. By the time the experimental apparatus was neutralized from the safety pushbuttons, the belt had driven itself halfway off of the lower pulley. When this hardware failure occurred approximately 222 of the required 400 cycles of the wear test procedure repetition had been completed. Once the upper pulley was properly repositioned on the driven shaft and the belt was properly repositioned in the middle of the lower pulley, the remaining 178 cycles of the wear test procedure repetition for treated test specimen 1 were completed.

The pressure transducer power supply failure occurred for treated test specimen 3, repetition number 4 when the battery supply voltage dropped below the critical level causing erroneous measurements of the brake pressure, specifically, lower than expected readings. Since the brake actuator is controlled based upon a target brake pressure, the erroneous measurements resulted in the actuator unable to fully release causing a massive temperature spike in the brake system. It was estimated that the temperatures produced during this massive spike were approximately 800 °F sustained for than a minute caused by a small amount of residual brake pressure maintained in the braking system when the control and measurement system believed no brake pressure was being applied. By the time the experimental apparatus was neutralized from the safety pushbuttons, approximately 268 of the required 300 cycles of the wear test procedure repetition had been completed. The remaining 32 cycles of the repetition for treated test specimen 3 were not completed.

The pressure transducer power supply failure resulted in a substantial rotor and pad mass loss, and therefore rotor and pad wear rates, compared to previous wear repetitions for treated test specimen 3 even though wear repetition 4 was only conducted for 268 of the required 300 cycles

5.2.5. Summary

In relation to the objectives of the current study, the dynamometer testing showed that relatively short test durations could produce clearly distinct variations of wear rates between specimens and components. Significantly lower brake application times were obtained during

dynamometer testing compared to predictions based on wear rates of similar materials measured by others using conventional tribological experiments. The rotor treatment test variations did not show conclusive evidence to suggest an advantage in subjecting the rotor materials used in the current study to cryogenic treatment to lower the rotor or pad wear rates. The brake application pressure test variations showed that increases in pressure resulted in an order of increase in the average rotor and pad wear rates of approximately 2.0 and 1.5, respectively.

6. CONCLUSIONS

A wear testing simulation and an inertia laboratory brake dynamometer were developed to demonstrate the ability of a tribological experimental apparatus to resolve differences in wear rates of brake materials. Testing was conducted on the dynamometer to verify the logic of the simulation and the functionality of the additions to the dynamometer by measuring wear rates of brake rotor material samples, some of which were subjected to cryogenic heat treatment to modify their wear rates, at varying brake application pressures.

The wear simulation consisted of a bedding and a wear procedure, both taking advantage of energy equivalent inertia simulation. Energy equivalency permitted the bedding and wear procedures to be simulated at a constant velocity and allowed representation of inertia on the full-scale laboratory brake dynamometer without the need for mechanical flywheels or electric motor feedback torque.

An inertia laboratory brake dynamometer was developed to function as a tribological experimental apparatus which required the addition of appropriate equipment and instrumentation to be capable of resolving differences in wear rates of brake materials. The dynamometer was comprised of several sub-systems to meet these requirements including temperature, pressure, drive, power, measurement and control, and safety systems.

Five brake material test sets were created for testing using the wear simulation and inertia laboratory brake dynamometer. Each test set consisted of a single brake rotor and two brake pads, from which three rotors were subjected to cryogenic heat treatment, and each functioned as integrated components of a full-scale brake system installed on the dynamometer.

Dynamometer testing consisted of exposing each brake material test set to a single application of the bedding procedure followed by repeated applications of the wear procedure. Brake application pressure was purposely varied across specific brake material test sets to investigate the wear rate sensitivity to brake application pressure. Optical microscopy and mass

loss measurements were conducted on each test set while wear rates were calculated directly from the measured mass loss with respect to the calculated sliding distance.

6.1. Significant findings

- Relatively short dynamometer test durations produced clearly distinct variations of wear rates between specimens and components.
- Dynamometer testing produced significantly lower total brake application times compared to predictions based on wear rates of similar materials as measured by others using conventional tribological experiments.
- The rotor treatment test variations did not show conclusive evidence to suggest an advantage in subjecting the rotor materials used in the current study to cryogenic treatment to lower the rotor or pad wear rates.
- The brake application pressure test variations showed that increases in pressure resulted in an order of increase in the average rotor and pad wear rates of approximately 2.0 and 1.5, respectively.

Thus, the dynamometer testing demonstrates that the wear simulation and inertia laboratory brake dynamometer developed during the current study can function together as a tribological experimental apparatus capable of resolving differences in wear rates of brake materials due to variations in brake application pressure at relatively short test durations.

6.2. Future work

The wear simulation and inertia laboratory brake dynamometer developed during the current study can be extended to investigate additional areas of research. Such areas may include:

- Investigation of the effects of cryogenic heat treatment on different brake rotor materials, which have shown promising results in the reduction of wear from other, non-brake related areas of research.
- Exhaustive brake material bedding study combining the inertia laboratory brake dynamometer capabilities with comprehensive material characterization to develop a

more thorough understanding of mechanisms during the initial contact of fresh, unworn brake materials

- Implement a different inertia simulation strategy to allow snub-based dynamometer testing to improve the ease at which comparisons are made between vehicle and dynamometer testing.

REFERENCES

- [1] Munson, Bruce Roy. *Fundamentals of Fluid Mechanics*. New York: John Wiley, 1998.
- [2] Johnston, Dan. *Drag*. U.S. Centennial of Flight Commission. Accessed 15 March 2009. <http://www.centennialofflight.gov/essay/Theories_of_Flight/drag/TH4.htm>
- [3] Rhee, Seong K. *The Role of Friction Film in Friction, Wear, and Noise of Automotive Brakes*. Society of Automotive Engineers International Congress and Exposition (1990): SAE Paper No. 900004.
- [4] Augsborg, Klaus, et al. *Comparison Between Different Investigation Methods of Quasi-Static and Dynamic Brake Pad Behaviour*. Society of Automotive Engineers 21st Annual Brake Colloquium and Exhibition (2003): SAE Paper No. 2003-01-3340.
- [5] Blau, Peter J. *Microstructure and Detachment Mechanism of Friction Layers on the Surface of Brake Shoes*. *Journal of Materials Engineering and Performance* 12.1 (2003): 56-60.
- [6] Blau, Peter J. *Tribological Investigation of Titanium-Based Materials for Brakes*. *Wear* 263.7 (2007): 1202-1211.
- [7] Coyle, J. P., and P. H. S. Tsang. *Microstructural Changes of Cast Iron Rotor Surfaces and Their Effects on Brake Performance and Wear Resistance*. Society of Automotive Engineers International Congress and Exposition (1983): SAE Paper No. 830534.
- [8] Jang, Ho, et al. *The Effect of the Composition and Microstructure of Gray Cast Iron on Preferential Wear During Parasitic Drag and on Intrinsic Damping Capacity*. Society of Automotive Engineers 21st Annual Brake Colloquium and Exhibition (2003): SAE Paper No. 2003-01-3313.
- [9] Mace, Gael, et al. *Characterisation of Material Transformation during Cast Iron Brake Disc Bedding*. Society of Automotive Engineers 24th Annual Brake Colloquium and Exhibition (2006): SAE Paper No. 2006-01-3185.
- [10] Tsang, P. H. S. et al. *Comparison of Chase and Inertial Brake Dynamometer Testing of Automotive Friction Materials*. *Wear of Materials* (1985): 129-137.
- [11] Cueva, G. et al. *Wear Resistance of Cast Irons Used in Brake Disc Rotor*. *Wear* 255.7 (2003): 1256-1260.
- [12] *Carbon-Ceramic Brake Discs*. SGL group. Accessed 14 March 2009. <http://www.sglgroup.com/cms/international/products/product-groups/bd/carbon-ceramic-brake-disks/index.html?_locale=en>
- [13] Wolf, Peter J. *Ceramic Composite Brakes: Better Braking Through Chemistry*. Edmunds.com. Accessed 14 March 2009. <<http://www.edmunds.com/ownership/techcenter/articles/130013/article.html>>

- [14] Wright, Peter G. *Formula 1 Technology*. Washington D.C.: Society of Automotive Engineers Inc, 2001.
- [15] Guipu, Xiao, et al. *Influence of Brake Condition on the Friction and Wear Properties of a Low-Metal Formulation*. Society of Automotive Engineers 21st Annual Brake Colloquium and Exhibition (2003): SAE Paper No. 2003-01-3314.
- [16] Trainor, Jim, et al. *Disc Brake Wear Debris Generation and Collection*. Society of Automotive Engineers 20th Annual Brake Colloquium and Exhibition (2002): SAE Paper No.2002-01-2595.
- [17] Loh, Wei-Yi, et al. *Dynamic Modeling of Brake Friction Coefficients*. Society of Automotive Engineers 18th Annual Brake Colloquium and Exhibition (2000): SAE Paper No. 2000-01-2753.
- [18] Ramousse, S. et al. *Thermal Characterisation of Brake Pads*. Journal of Thermal Analysis and Calorimetry 64.3 (2001): 933-943
- [19] Lawson, T. G., and F. J. Kateb. *Automated Data Acquisition and Processing for Brake Testing*. Society of Automotive Engineers Congress and Exposition (1978): SAE Paper No. 780150
- [20] Sanders, P. G. et al. *A Reduced-Scale Brake Dynamometer for Friction Characterization*. Tribology International 34.9 (2001): 609-615.
- [21] Woo, Gui-Aee et al. *Evaluation of the Friction Coefficient from the Dynamometer Test of the Aircraft*. Key Engineering Materials 277 (2005): 757-764.
- [22] Oldershaw, R. M. et al. *Brake Road Testing in the Laboratory*. Society of Automotive Engineers Automobile Engineering Meeting (1973): SAE Paper No. 730563
- [23] Hohmann, Ch. et al. *Pad Wear Simulation Model*. Society of Automotive Engineers 17th Annual Brake Colloquium and Exhibition (1999): SAE Paper No. 1999-01-3392.
- [24] Sinclair, David, and W. F. Gulick. *The Dual Brake Inertia Dynamometer-A New Tool for Brake Testing*. Society of Automotive Engineers (1963): 630464.
- [25] *Glossary of Terms*. Society of Tribologists and Lubrication Engineers. Accessed 15 March 2009. <<http://www.stle.org/resources/glossary/default.aspx>>
- [26] Kalpakjian, Serope. *Manufacturing Processes for Engineering Materials*. Upper Saddle River, N.J: Prentice Hall, 2003.
- [27] Barron, R. F. *Cryogenic Treatment of Metals to Improve Wear Resistance*. Cryogenics 22.8 (1982): 409-413.
- [28] ASTM Standard G99, 2005, *Standard Test Method for Wear Testing with a Pin-on-Disk Apparatus*. ASTM International, West Conshohocken, PA, 2005, DOI: 10.1520/G0099-05, <www.astm.org>.
- [29] Koszela, Waldemar. *The Effect of Oil Pockets Size and Distribution on Wear in Lubricated Sliding*. Wear 263.7 (2007): 1585-1592.
- [30] Boyles, Charles M. *Be Cool*. Cutting Tool Engineering 54.4 (2002): 50-54.
- [31] Paulin, Pete. *Frozen Gears*. Gear Technology 10.2 (1993): 26-29.

- [32] Reasbeck, R. B. *Improved Tool Life by the Cryotough Treatment*. Metallurgia 56.4 (1989): 178-179.
- [33] Meng, F. *Role of Eta-Carbide Precipitations in the Wear Resistance Improvements of Fe-12Cr-Mo-V-1.4C Tool Steel by Cryogenic Treatment*. ISIJ International 34.2 (1994): 205-210.
- [34] Trucks, H. E. *How Cryogenics is Used for the Treatment of Metals*. Manufacturing Engineering 91.6 (1983): 54-55.
- [35] SAE Standard J2522, *Dynamometer Global Brake Effectiveness*. Society of Automotive Engineers Inc (2003).
- [36] Molinari, A. *Effect of Deep Cryogenic Treatment on the Mechanical Properties of Tool Steels*. Journal of materials processing technology 118.1 (2001): 350-355.
- [37] Makela, K. K. *Methods and Apparatuses for Tribological and Rheological Testing*. Tribologia 17.2 (1998): 3-13.
- [38] Okamura, Toshikazu, and Manabu Ono. *Effect of Brake Disc Surface Texture on Friction Behavior during Running-in*. Society of Automotive Engineers 22nd Annual Brake Colloquium and Exhibition (2004): SAE Paper No. 2004-01-2765.
- [39] Blau, Peter J. *On the Nature of Running-In*. Tribology International 38.11 (2005): 1007-1012.
- [40] Weiss, Matt, and James Walker, Jr. *Pad and Rotor Bed-In Theory, Definitions and Procedures*. StopTech. Accessed 28 March 2009. <http://www.stoptech.com/tech_info/wp_bedincontents.shtml>
- [41] Osterle, W. et al. *Correlations Between Surface Modification and Tribological Performance of Brake Pads*. Surface Engineering 17.2 (2001): 123-125.
- [42] *DSC220C Differential Scanning Calorimeter Users Manual*. Seiko Instruments Inc, (1990).
- [43] *Dynamometer Global Brake Effectiveness*. Society of Automotive Engineers Inc, J2522 (2003).
- [44] Von Thun, Hans J. *A Double Ended Brake Test Rig with Inertia Simulation*. Society of Automotive Engineers Passenger Car Meeting (1980): SAE Paper No. 800855.
- [45] Thompson, James K. *Inertia Simulation in Brake Dynamometer Testing*. Society of Automotive Engineers 20th Annual Brake Colloquium and Exhibition (2002): SAE Paper No. 2002-01-2601.
- [46] Ma, Jijie, et al. *A New Method of Inertia Simulation in Brake Dynamometer Testing*. Society of Automotive Engineers 26th Annual Brake Colloquium and Exhibition (2008): SAE Paper No. 2008-01-2578.
- [47] Limpert, Rudolf. *Brake Design and Safety*. Warrendale, Pa: Society of Automotive Engineers, 1999.
- [48] *Technical Information: Features of Photomicrosensors*. Omron. Accessed March 10th, 2009. <http://www.omron.com/ecb/products/pdf/en-ph_micro_info.pdf>

- [49] *Dynapro Single Billet Caliper*. Wilwood Disc Brakes. Accessed 18 March 2009. <<http://www.wilwood.com/pdf/fl197.pdf>>
- [50] *Brake Pad Catalog*. 12 June 2008. Wilwood Disc Brakes. Accessed 17 March 2009. <http://catalogs.wilwood.com/_pdf/_pads/BrakePadCatalog.pdf>
- [51] Cooke, Benjamin T. *ICE cryogenic treatment process profile data*. International Cryogenic Engineering, Inc., CD-ROM. 2007.
- [52] Walker, James Jr. *Pad Knock back: A Common Racing Phenomenon*. StopTech. Accessed 24 March 2009. <http://www.stoptech.com/tech_info/wp_knockback.shtml>

APPENDICES

A. Differential scanning calorimetry

A.1. Measurement principle

The following is an excerpt from the Seiko Instruments Inc. DSC220C Differential Scanning Calorimeter Operation Manual [42]:

The DSC220C measurement chamber is designed for heat flux DSC measurement. The basic structure of the chamber is shown below.

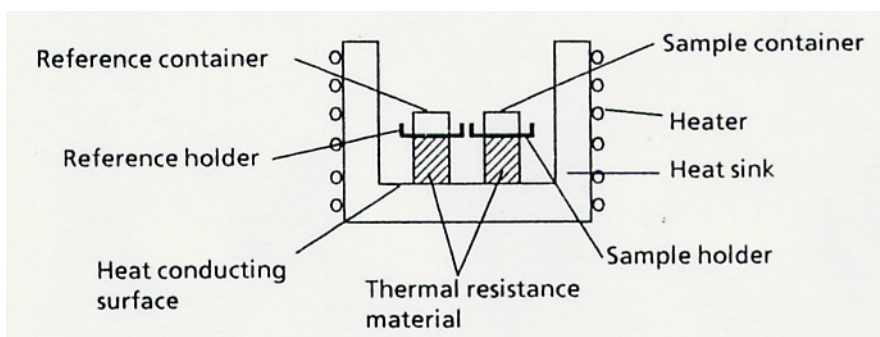


Figure A.1: Seiko Instruments Inc. DSC220C chamber structure [42]

The temperature of the high conductance heat sink is accurately controlled by the heater in accordance with the temperature program. The heat from the heat sink is conducted from the heat conducting surface through the thermal resistance material into the sample and reference holders and containers. This changes the temperature of the sample and reference. The heat flow passing through the thermal resistance material is proportional to the temperature difference between the heat conducting surface on one end and the sample holder on the other end. The specially designed heat sink is controlled precisely to maintain a uniform temperature at the heat conducting surface. Therefore, the measured difference in heat flow through the sample holder and reference holder is proportional to the sample and reference temperature differences. In this way, a heat flux type DSC detects the temperature difference signal and outputs it as a DSC signal.

A.2. Test results

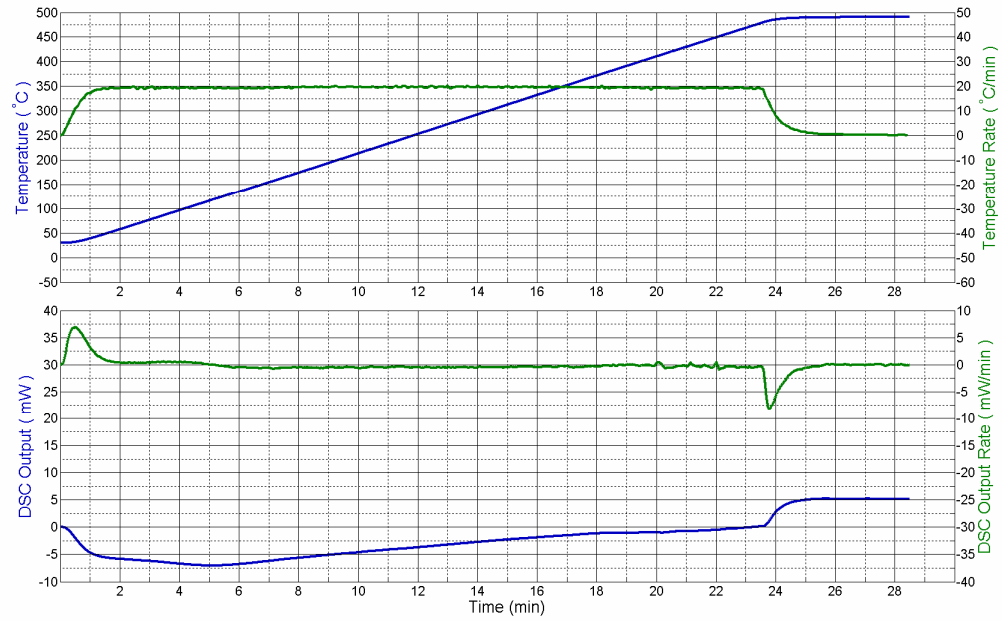


Figure A.2: DSC test results from the first test set for the first temperature exposure of the new compound sample

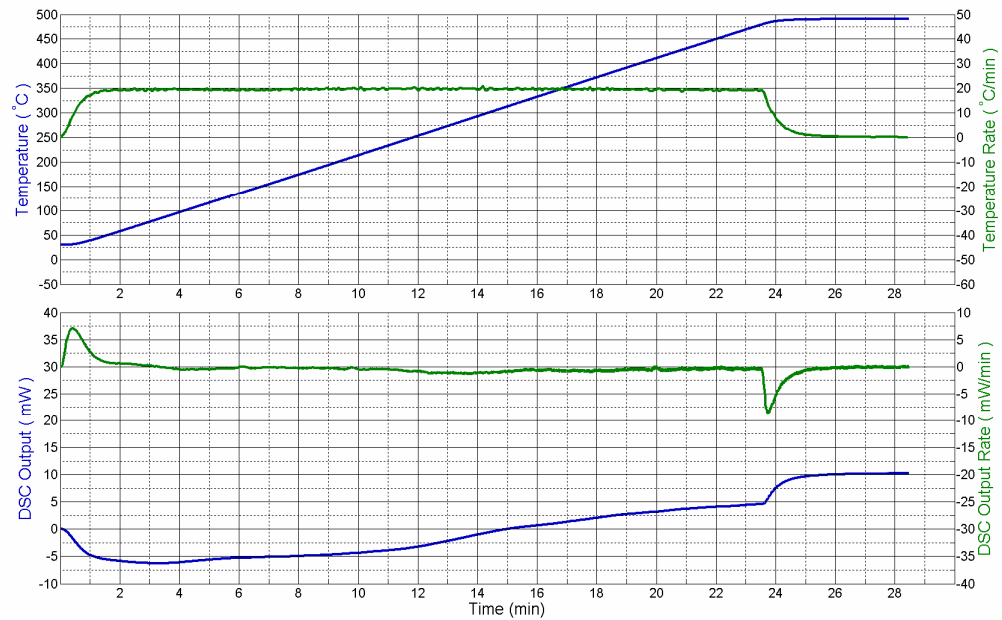


Figure A.3: DSC test results from the first test set for the first temperature exposure of the used compound sample

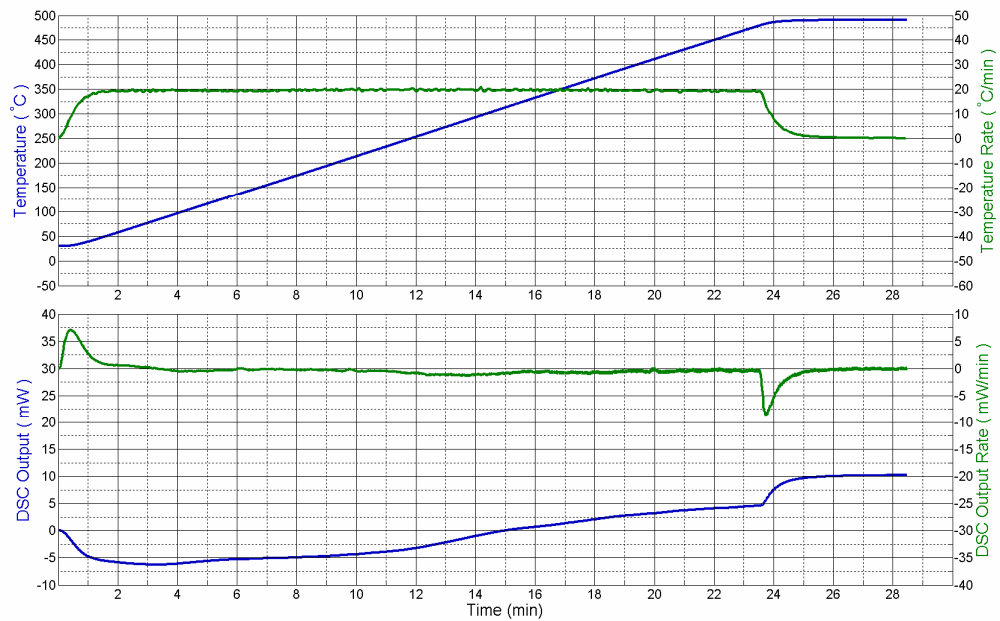


Figure A.4: DSC test results from the first test set for the second temperature exposure of the new compound sample

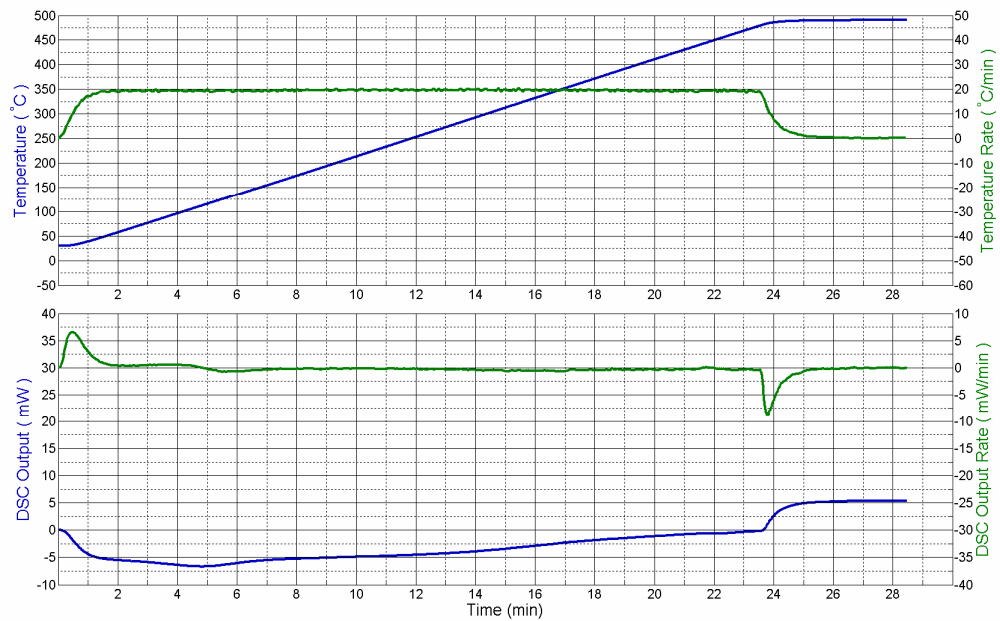


Figure A.5: DSC test results from the first test set for the third temperature exposure of the new compound sample

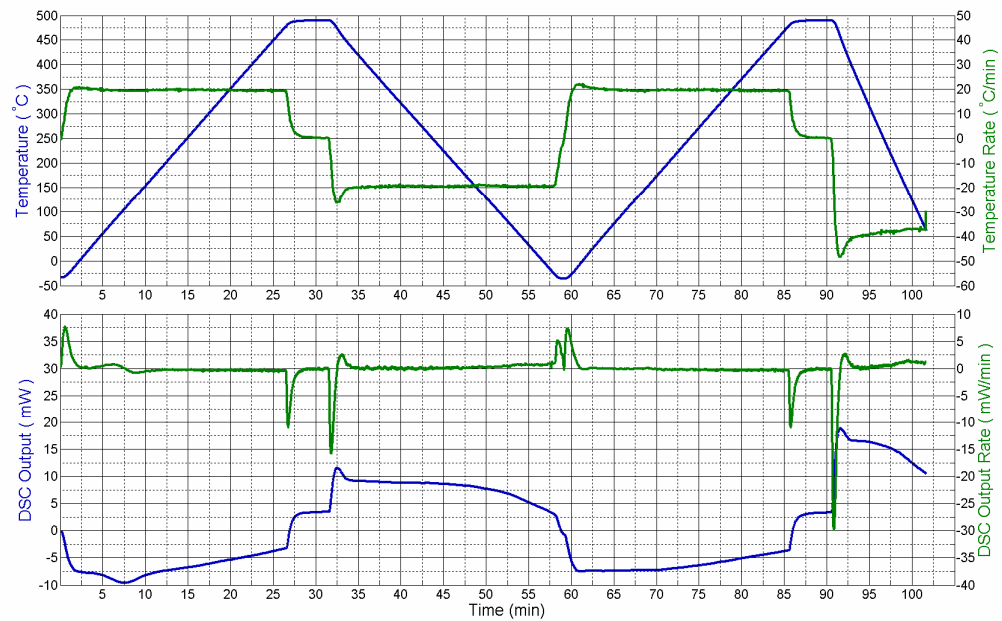


Figure A.6: DSC test results from the second test set for the new compound sample

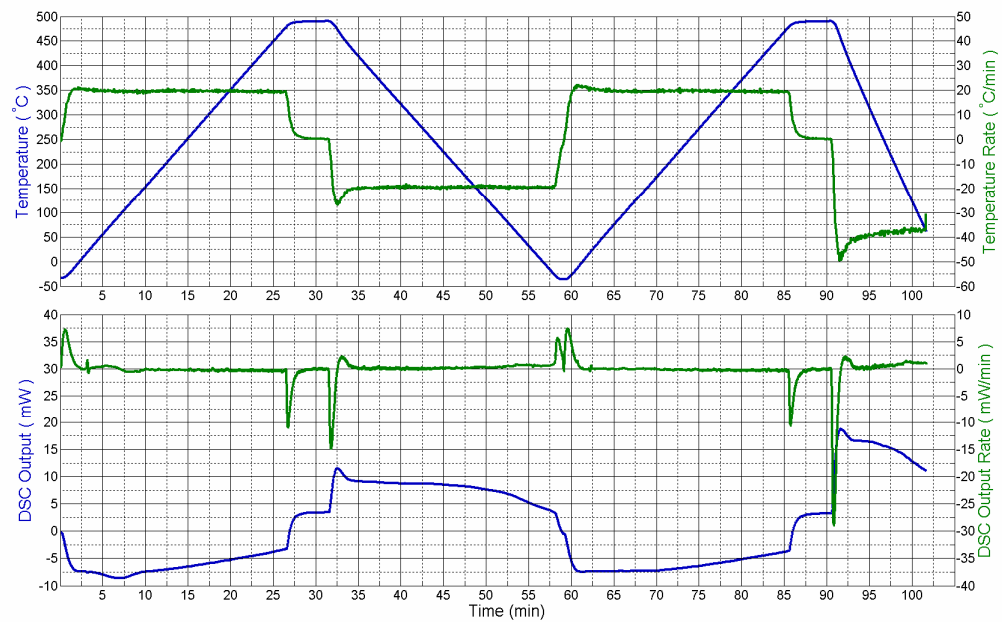


Figure A.7: DSC test results from the second test set for the used compound sample

B. Test details

B.1. SAE J2522 standard

The specific details for the first three test sections concerned with bedding from SAE *J2522: Dynamometer Global Brake Effectiveness* [35] are presented below.

Table B.1: Green Mu Characteristic section detail [35]

Cycle No.	Brake Speed (kph)	Release Speed (kph)	Brake Pressure (kPa)	Initial Brake Temp. (°C)	Final Brake Temp. (°C)
1...30	80	30	3 000	≤ 100	open

Table B.2: Burnish section detail [35]

Cycle No.	Brake Speed (kph)	Release Speed (kph)	Brake Pressure (kPa)	Initial Brake Temp. (°C)	Final Brake Temp. (°C)
1	80	30	1500	≤ 100	open
2	80	30	3000	≤ 100	open
3	80	30	1500	≤ 100	open
4	80	30	1800	≤ 100	open
5	80	30	2200	≤ 100	open
6	80	30	3800	≤ 100	open
7	80	30	1500	≤ 100	open
8	80	30	2600	≤ 100	open
9	80	30	1800	≤ 100	open
10	80	30	3400	≤ 100	open
11	80	30	1500	≤ 100	open
12	80	30	2600	≤ 100	open
13	80	30	1500	≤ 100	open
14	80	30	2200	≤ 100	open
15	80	30	3000	≤ 100	open
16	80	30	4600	≤ 100	open
17	80	30	2600	≤ 100	open
18	80	30	5100	≤ 100	open
19	80	30	2200	≤ 100	open
20	80	30	1800	≤ 100	open
21	80	30	4200	≤ 100	open
22	80	30	1500	≤ 100	open
23	80	30	1800	≤ 100	open
24	80	30	4600	≤ 100	open
25	80	30	2600	≤ 100	open
26	80	30	1500	≤ 100	open
27	80	30	3400	≤ 100	open
28	80	30	2200	≤ 100	open
29	80	30	1800	≤ 100	open
30	80	30	3000	≤ 100	open
31	80	30	1800	≤ 100	open
32	80	30	3800	≤ 100	open

Table B.3: Characteristic Value section detail [35]

Cycle No.	Brake Speed (kph)	Release Speed (kph)	Brake Pressure (kPa)	Initial Brake Temp. (°C)	Final Brake Temp. (°C)
1...6	80	30	3000	≤ 100	open

B.2. Bedding test procedure

Table B.4: First 50 cycles of bedding test procedure

Cycle No.	Brake Speed (rpm)	Initial Brake Temp. (°F)	Brake Temp. Rise (°F)	Brake Pressure (psi)
1	836	340	35.7	139
2	836	340	35.7	139
3	836	340	35.7	139
4	836	340	35.7	139
5	836	340	35.7	139
6	836	340	35.7	139
7	836	340	35.7	139
8	836	340	35.7	139
9	836	340	35.7	139
10	836	340	35.7	139
11	836	340	35.7	139
12	836	340	35.7	139
13	836	340	35.7	139
14	836	340	35.7	139
15	836	340	35.7	139
16	836	340	35.7	139
17	836	340	35.7	139
18	836	340	35.7	139
19	836	340	35.7	139
20	836	340	35.7	139
21	836	340	35.7	139
22	836	340	35.7	139
23	836	340	35.7	139
24	836	340	35.7	139
25	836	340	35.7	139
26	836	340	35.7	139
27	836	340	35.7	139
28	836	340	35.7	139
29	836	340	35.7	139
30	836	340	35.7	139
31	836	340	25.3	70
32	836	340	35.7	139
33	836	340	25.3	70
34	836	340	27.6	83
35	836	340	30.5	102
36	836	340	40.1	176
37	836	340	25.3	70
38	836	340	33.1	120
39	836	340	27.6	83
40	836	340	37.9	157
41	836	340	25.3	70
42	836	340	33.1	120
43	836	340	25.3	70
44	836	340	30.5	102
45	836	340	35.7	139
46	836	340	44.1	213
47	836	340	33.1	120
48	836	340	46.5	236
49	836	340	30.5	102
50	836	340	27.6	83

Table B.5: Second 50 cycles of bedding test procedure

Cycle No.	Brake Speed (rpm)	Initial Brake Temp. (°F)	Brake Temp. Rise (°F)	Brake Pressure (psi)
51	836	340	42.1	194
52	836	340	25.3	70
53	836	340	27.6	83
54	836	340	44.1	213
55	836	340	33.1	120
56	836	340	25.3	70
57	836	340	37.9	157
58	836	340	30.5	102
59	836	340	27.6	83
60	836	340	35.7	139
61	836	340	27.6	83
62	836	340	40.1	176
63	836	340	25.3	70
64	836	340	35.7	139
65	836	340	25.3	70
66	836	340	27.6	83
67	836	340	30.5	102
68	836	340	40.1	176
69	836	340	25.3	70
70	836	340	33.1	120
71	836	340	27.6	83
72	836	340	37.9	157
73	836	340	25.3	70
74	836	340	33.1	120
75	836	340	25.3	70
76	836	340	30.5	102
77	836	340	35.7	139
78	836	340	44.1	213
79	836	340	33.1	120
80	836	340	46.5	236
81	836	340	30.5	102
82	836	340	27.6	83
83	836	340	42.1	194
84	836	340	25.3	70
85	836	340	27.6	83
86	836	340	44.1	213
87	836	340	33.1	120
88	836	340	25.3	70
89	836	340	37.9	157
90	836	340	30.5	102
91	836	340	27.6	83
92	836	340	35.7	139
93	836	340	27.6	83
94	836	340	40.1	176
95	836	340	35.7	139
96	836	340	35.7	139
97	836	340	35.7	139
98	836	340	35.7	139
99	836	340	35.7	139
100	836	340	35.7	139

C. Equation development

C.1. Vehicle deceleration

The following calculations attempt to estimate the vehicle deceleration based upon the various brake system components under an applied brake pressure. The vehicle deceleration calculation was subjected to braking limits imposed by the tire coefficient of friction and vehicle longitudinal weight transfer (aerodynamic effects were ignored).

The total front brake force as a result of an applied brake pressure is:

$$A_{fp} = \frac{\pi}{4} D_{fp}^2 \quad (\text{C.1})$$

$$F_{fc} = N_{fp} p_f A_{fp} \quad (\text{C.2})$$

$$R_{fe} = \sqrt{\left(\frac{1}{2}\right) \left[\left(\frac{D_{fr}}{2}\right)^2 + \left(\frac{D_{fr}}{2} - L_{fp}\right)^2 \right]} \quad (\text{C.3})$$

$$\tau_f = \mu_{fb} F_{fc} R_{fe} \quad (\text{C.4})$$

$$F_f = N_{fc} \tau_f R_{ft} \quad (\text{C.5})$$

The total rear brake force as a result of an applied brake pressure is:

$$p_r = p_f \left(\frac{100}{\%_{fb}} - 1 \right) \quad (\text{C.6})$$

$$A_{rp} = \frac{\pi}{4} D_{rp}^2 \quad (\text{C.7})$$

$$F_{rc} = N_{rp} p_r A_{rp} \quad (\text{C.8})$$

$$R_{re} = \sqrt{\left(\frac{1}{2}\right) \left[\left(\frac{D_{rr}}{2}\right)^2 + \left(\frac{D_{rr}}{2} - L_{rp}\right)^2 \right]} \quad (\text{C.9})$$

$$\tau_r = \mu_{rb} F_{rc} R_{re} \quad (\text{C.10})$$

$$F_r = N_{rc} \tau_r R_{rt} \quad (\text{C.11})$$

The maximum front brake force as a result of tire coefficient of friction and vehicle longitudinal weight transfer is:

$$W_{fs} = \frac{\%_{fm}}{100} m \quad (\text{C.12})$$

$$F_{f-\max} = \mu_{ft} \left[W_{fs} + \left(\frac{h_{cg}}{L_{wb}} \right) ma \right] \quad (\text{C.13})$$

The maximum rear brake force as a result of tire coefficient of friction and vehicle longitudinal weight transfer is:

$$W_{rs} = \left(1 - \frac{\%_{fm}}{100} \right) m \quad (\text{C.14})$$

$$F_{r-\max} = \mu_{rt} \left[W_{rs} - \left(\frac{h_{cg}}{L_{wb}} \right) ma \right] \quad (\text{C.15})$$

If the total front brake force (F_f) is less than or equal to the maximum front brake force ($F_{f-\max}$) and the total rear brake force (F_r) is less or equal to than the maximum rear brake force ($F_{r-\max}$), then the theoretical vehicle deceleration from the total front and rear brake forces is:

$$\boxed{a = \frac{F_f + F_r}{m}} \quad (\text{C.16})$$

If the total front brake force (F_f) is greater than the maximum front brake force ($F_{f-\max}$) or the total rear brake force (F_r) is greater than the maximum rear brake force ($F_{r-\max}$), then the vehicle is experiencing wheel lock up on the axle, front or rear, which has exceeded the maximum available traction.

C.2. Brake rotor surface temperature

To estimate the brake rotor surface temperature during a single stop from simplified temperature analysis (equation C.23), several intermediate equations (C.17 to C.21) were utilized as presented in, *Brake Design and Safety*, by Rudolf Limpert, [47]:

$$V(t) = V_i + at \quad (\text{C.17})$$

$$E_b(t) = \frac{1}{2} m [V(t)]^2 \quad (\text{C.18})$$

$$P_b(t) = \frac{dE_b}{dt} = am(V_i + at) \quad (\text{C.19})$$

$$P_{b-avg} = \frac{1}{2} am [a(t_1 + t_2) + 2V_i] \quad (\text{C.20})$$

$$P_{b-avg}^* = \frac{1}{2} \left(\frac{1}{2} \right) P_{b-avg} Q_{\%r} F_{\%f} \quad (\text{C.21})$$

$$q''_{(o)} = \frac{P_b(t=0)}{A_s} \quad (\text{C.22})$$

$$\Delta T_b = \sqrt{\frac{5}{18} \left(\frac{q''_{(o)} \sqrt{t_f}}{\sqrt{\rho_r c_r k_r}} \right)} \quad (\text{C.23})$$

Assumptions:

- Constant vehicle acceleration
- Kinetic energy of rotating components is negligible
- Brake application duration is shorter than time for thermal energy to conduct through brake rotor
- No convective cooling of the brake rotor surface occurs
- All brake energy is absorbed by the brake rotor and brake pads

C.3. Effective brake rotor radius

To calculate the effective brake radius based on equal swept surface areas on either side of the effective radius, the outer and inner radii must be known. The outer radius is defined by the furthest point, measured radially from the center of the rotor, of the pad friction surface. The inner radius is defined by the closest point, measured radially from the center of the rotor, of the pad friction surface. It follows that:

$$A_o = \pi(R_o^2 - R_e^2) \quad (\text{C.24})$$

$$A_i = \pi(R_e^2 - R_i^2) \quad (\text{C.25})$$

By equating the two swept surface area equations, C.24 and C.25, the effective rotor radius equation can be determined:

$$\pi(R_o^2 - R_e^2) = \pi(R_e^2 - R_i^2) \quad (\text{C.26})$$

$$2R_e^2 = R_o^2 + R_i^2 \quad (\text{C.27})$$

$$\boxed{R_e = \sqrt{\frac{R_o^2 + R_i^2}{2}}} \quad (\text{C.28})$$

For the particular case where the furthest point of the pad friction surface is coincident with the geometric radius of the rotor, the effective rotor radius equation can be manipulated into the following form:

$$\boxed{R_e = \sqrt{\left(\frac{1}{2}\right) \left[\left(\frac{D_r}{2}\right)^2 + \left(\frac{D_r}{2} - L_p\right)^2 \right]}} \quad (\text{C.29})$$

C.4. Coefficient of friction

To calculate the coefficient of friction as measured by the experimental apparatus, the definition of coefficient of friction is used as the basis and the brake pressure and torque measurements are incorporated. It follows that:

$$\mu = \frac{F_{friction}}{F_{normal}} \quad (\text{C.30})$$

$$F_{friction} = \frac{F_{lc} L_{lc}}{R_e} \quad (\text{C.31})$$

$$F_{normal} = N_p A_p P_b \quad (\text{C.32})$$

$$\boxed{\mu = \frac{F_{lc} L_{lc}}{N_p A_p P_b R_e}} \quad (\text{C.33})$$

D. Wiring connections

D.1. Shielded connector block

E. Experimental apparatus design drawings

E.1. Brake actuator mount

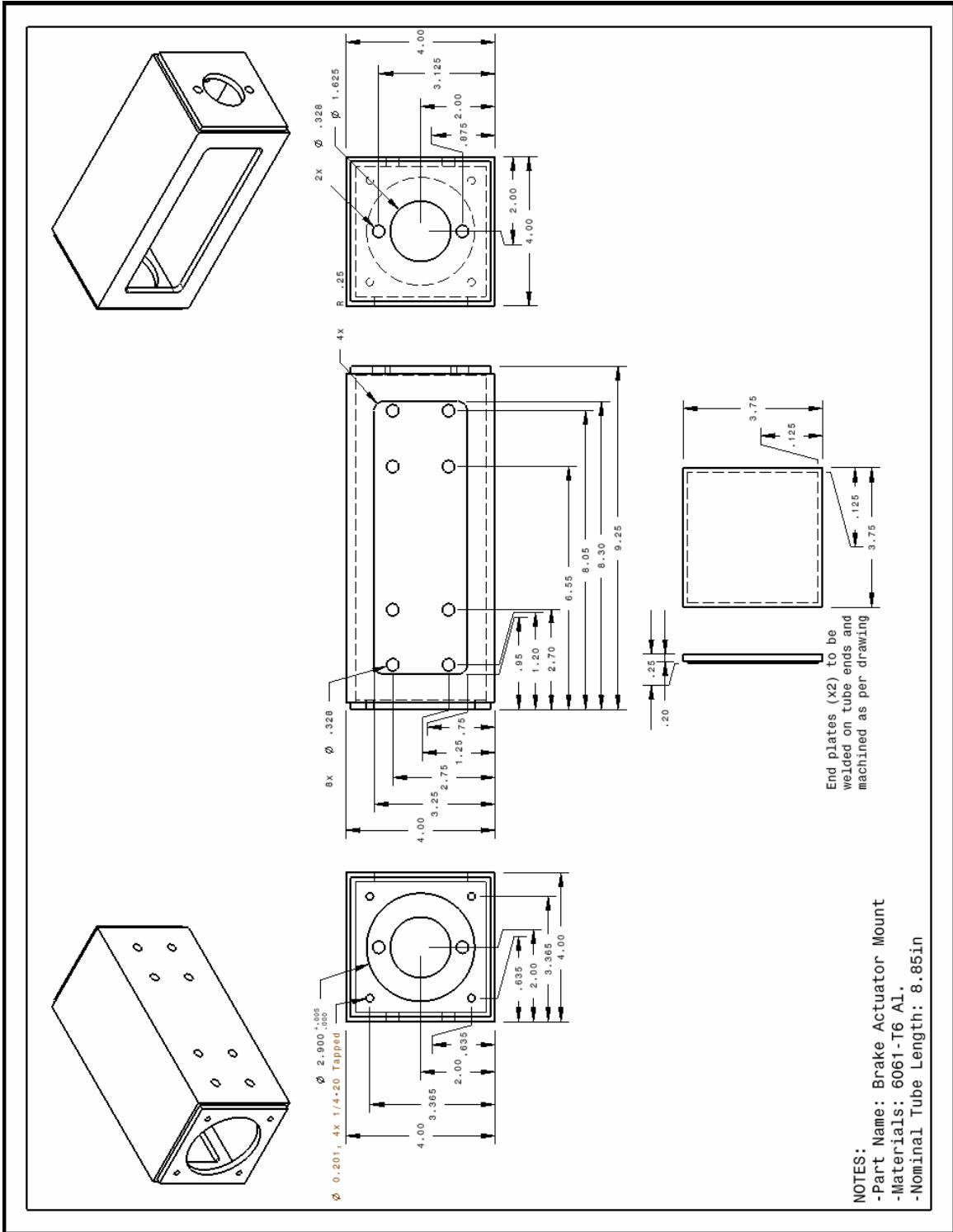


Figure E.1: Brake actuator mount design drawing

E.2. Shaft encoder mount

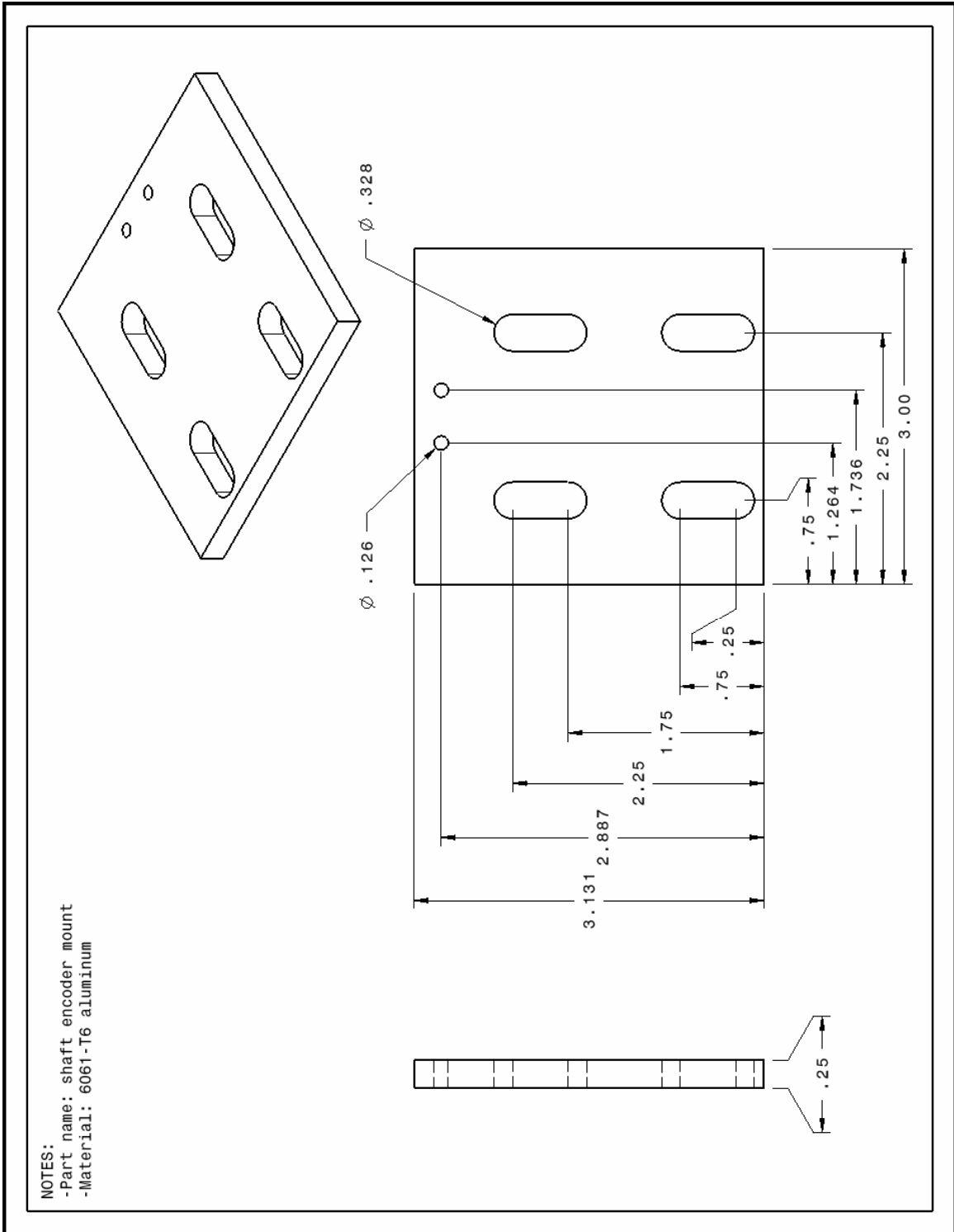


Figure E.2: Shaft encoder mount design drawing

E.3. Shaft encoder toothed wheels

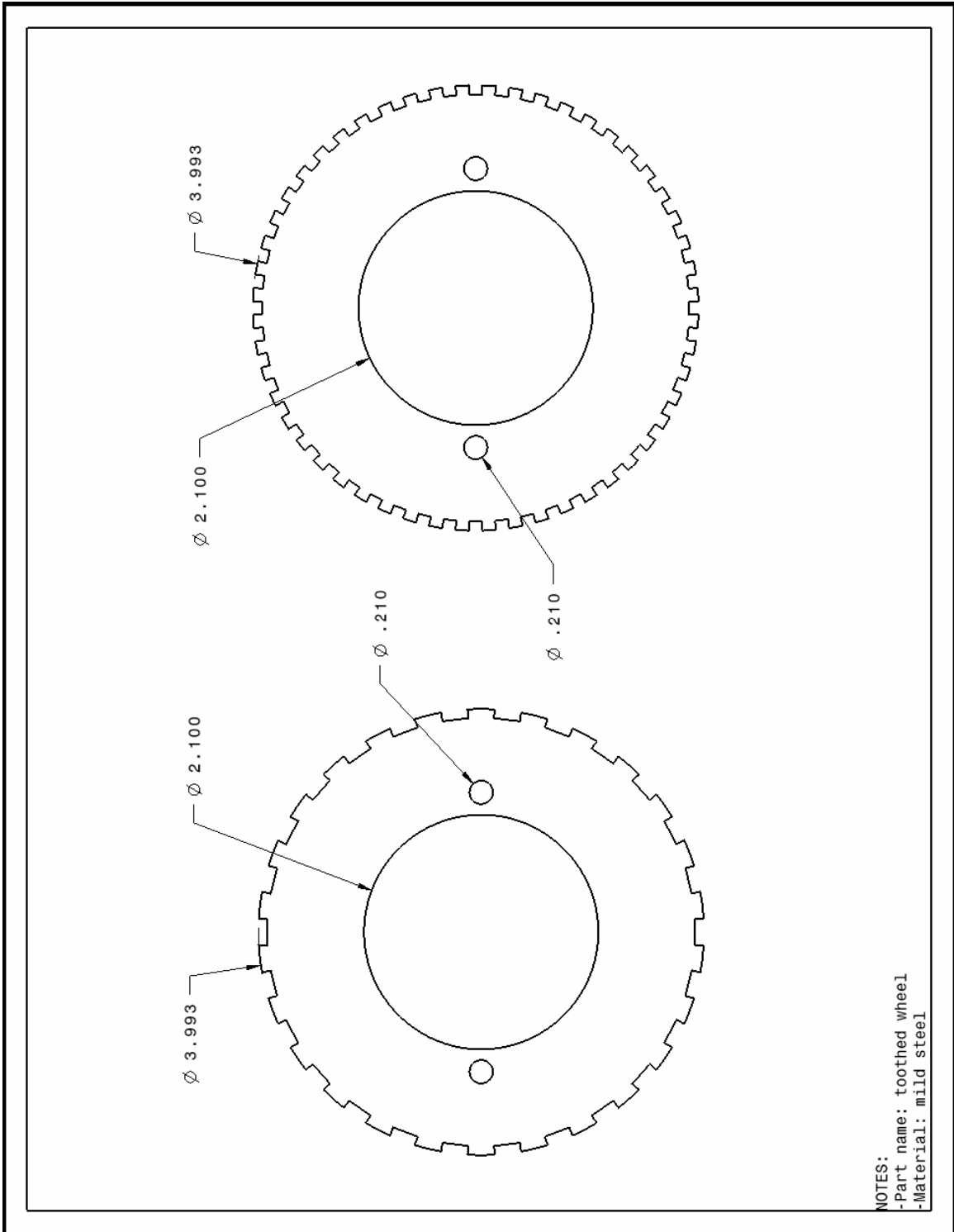


Figure E.3: Shaft encoder toothed wheels design drawing

E.4. Brake rotor

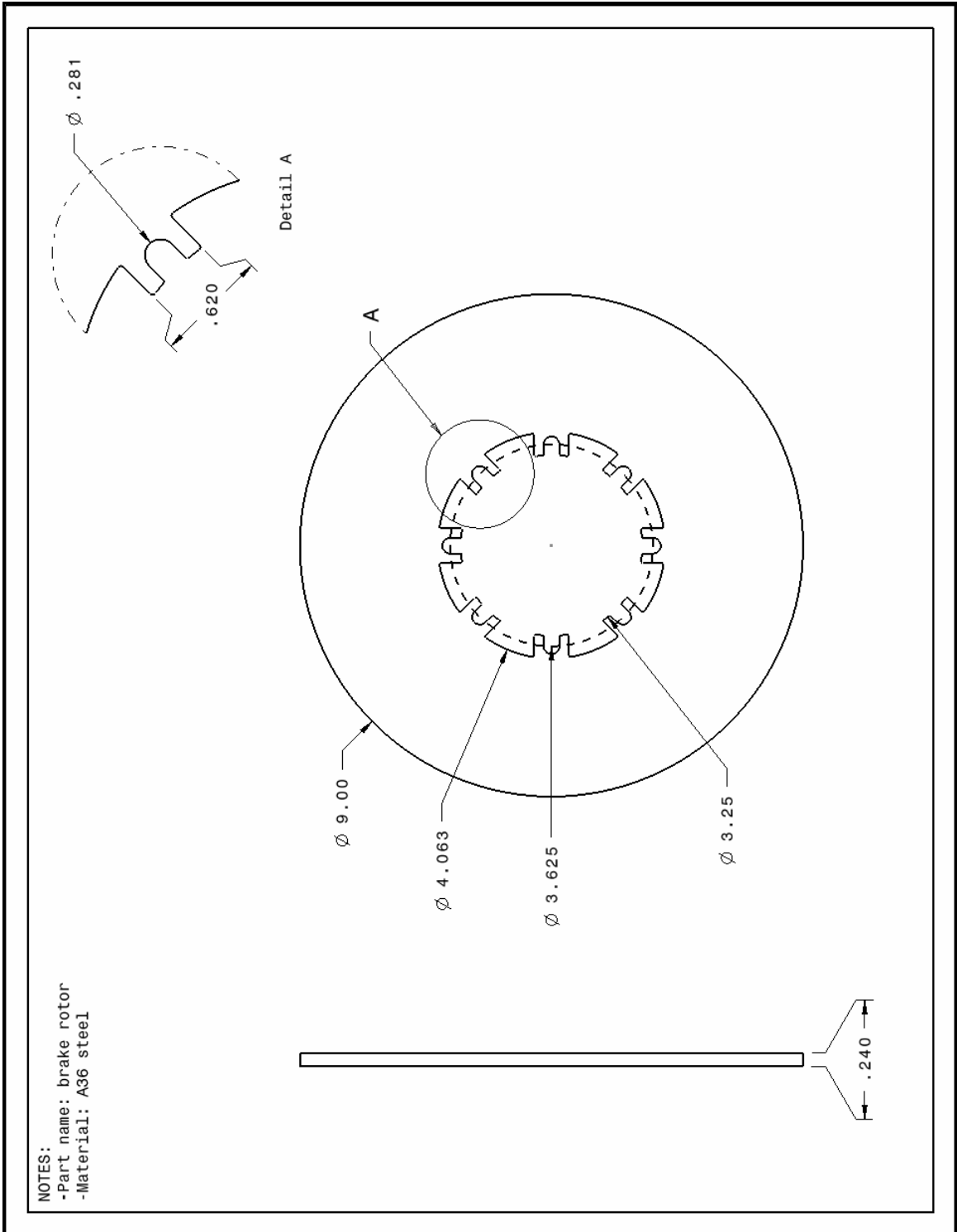


Figure E.4: Brake rotor design drawing

E.5. Brake hat

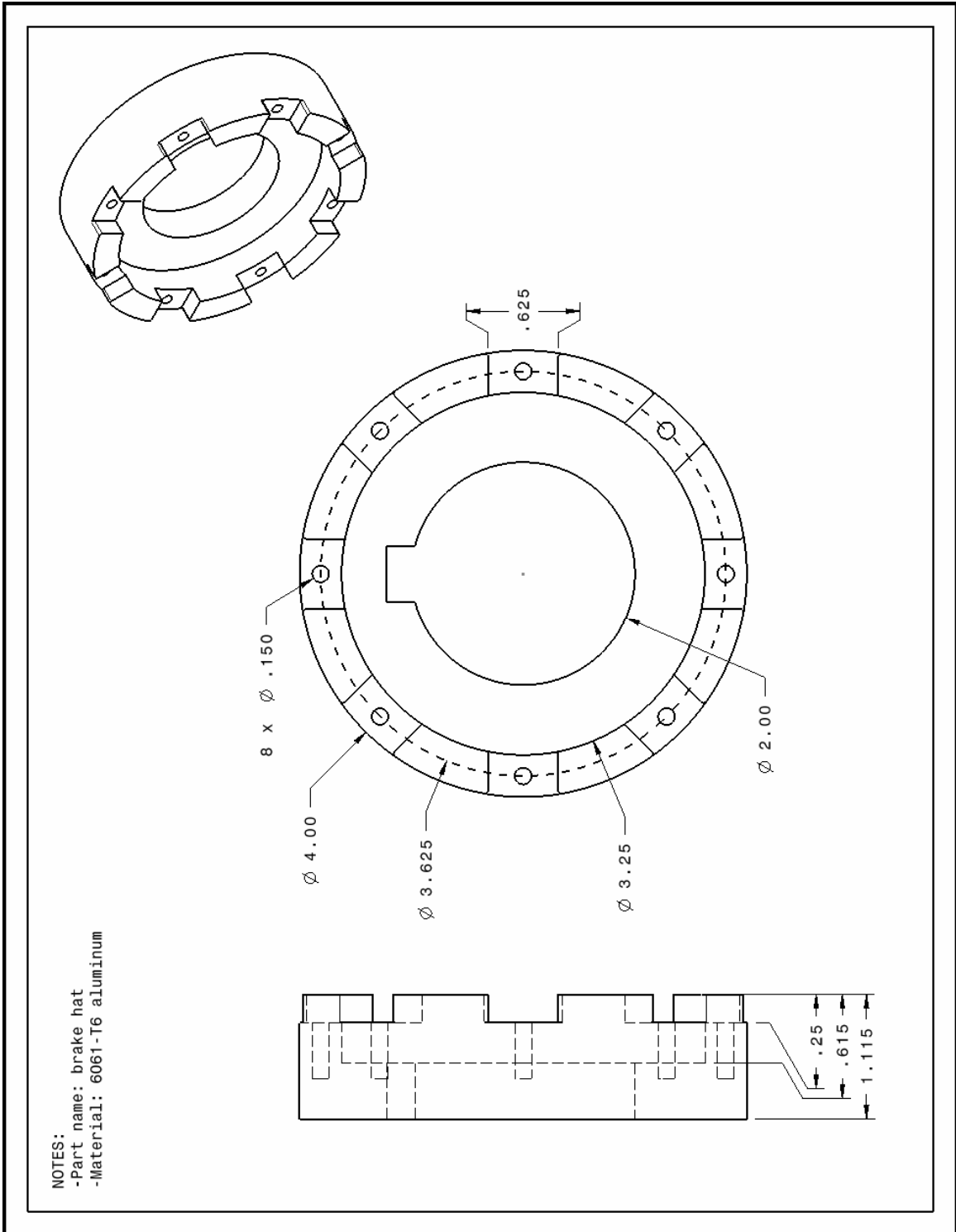


Figure E.5: Brake hat design drawing

E.7. Load cell lower mount

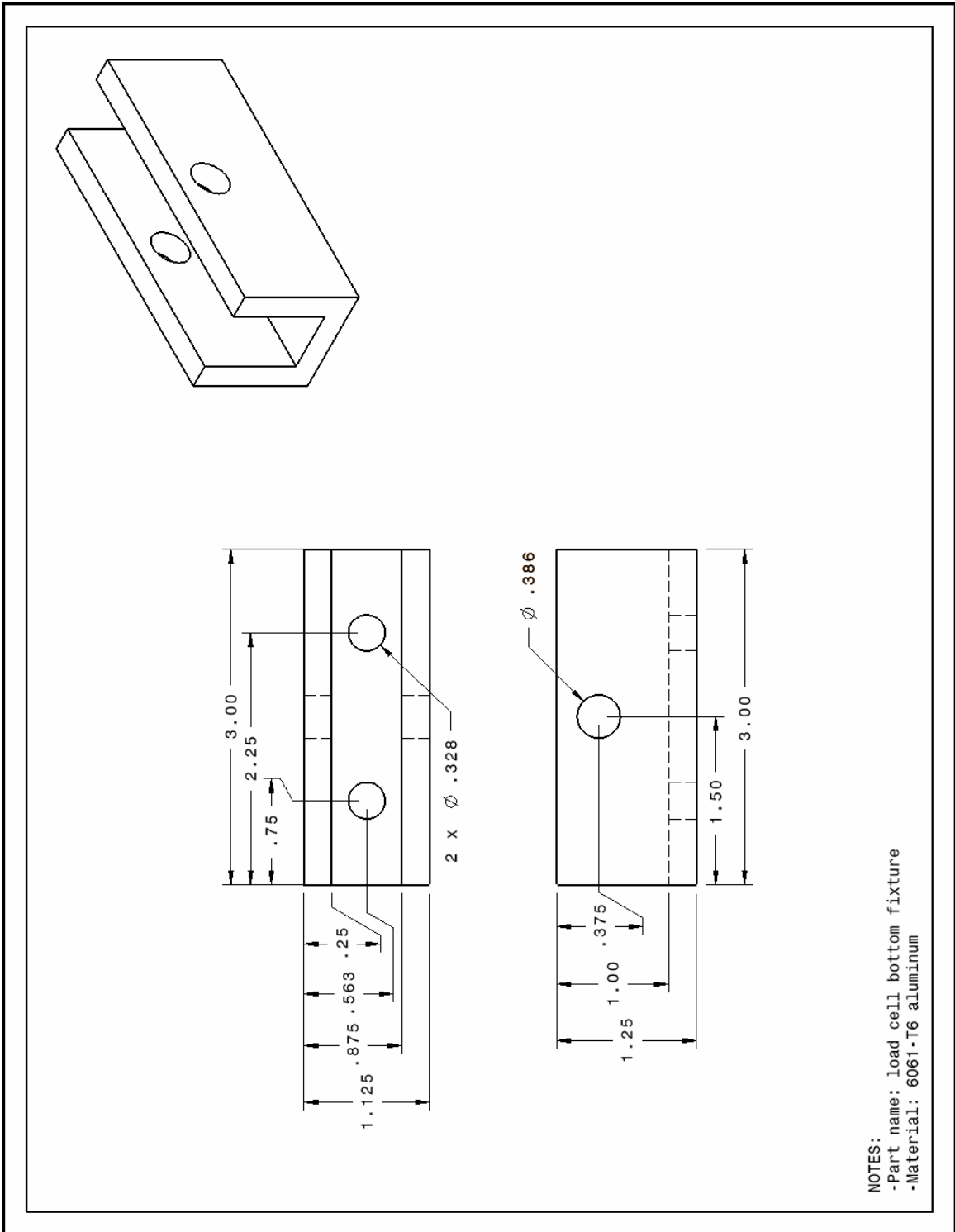


Figure E.7: Load cell lower mount design drawing

E.8. Load cell upper mount

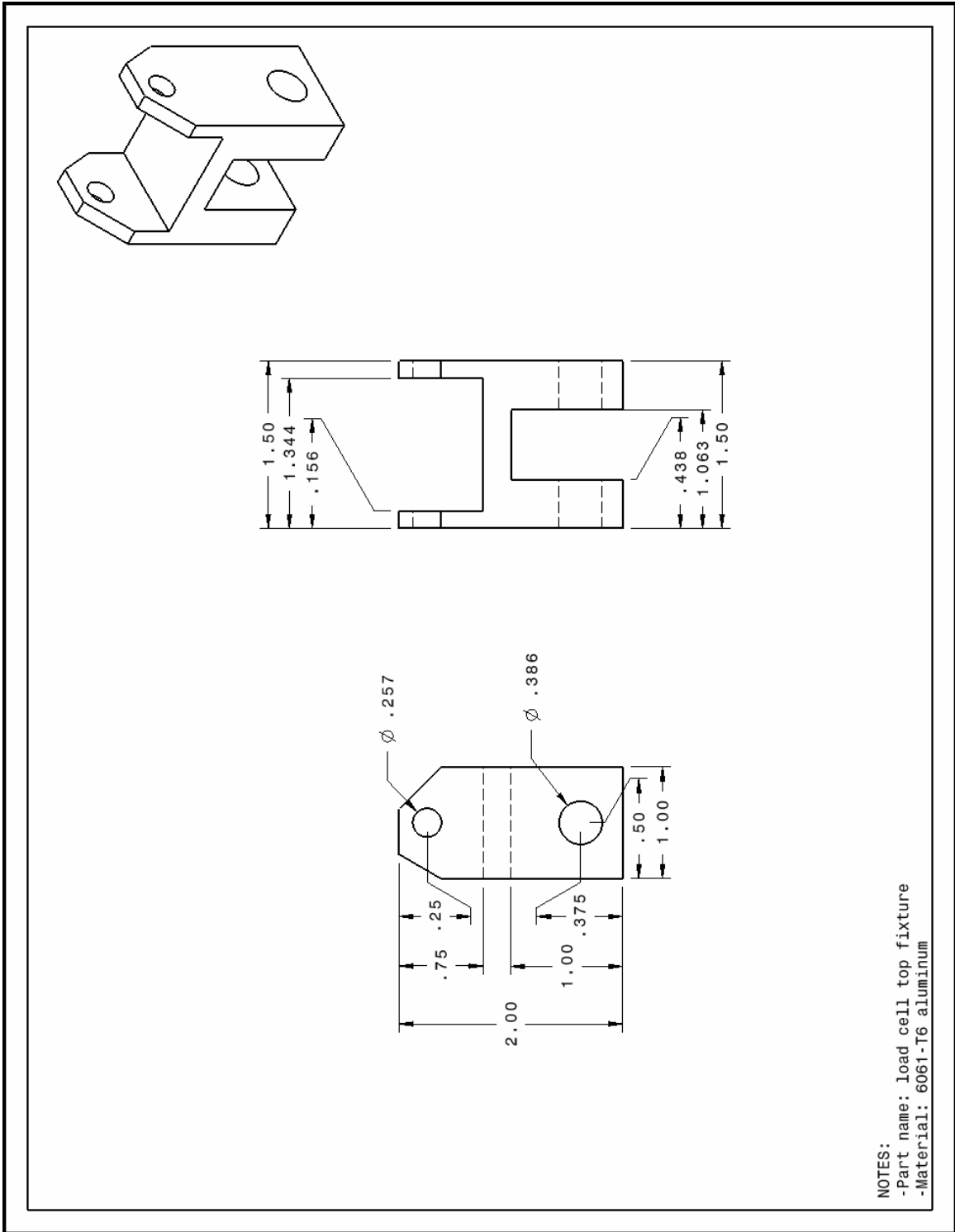


Figure E.8: Load cell upper mount design drawing

F. Experimental apparatus exploded views

F.1. Brake actuator mount

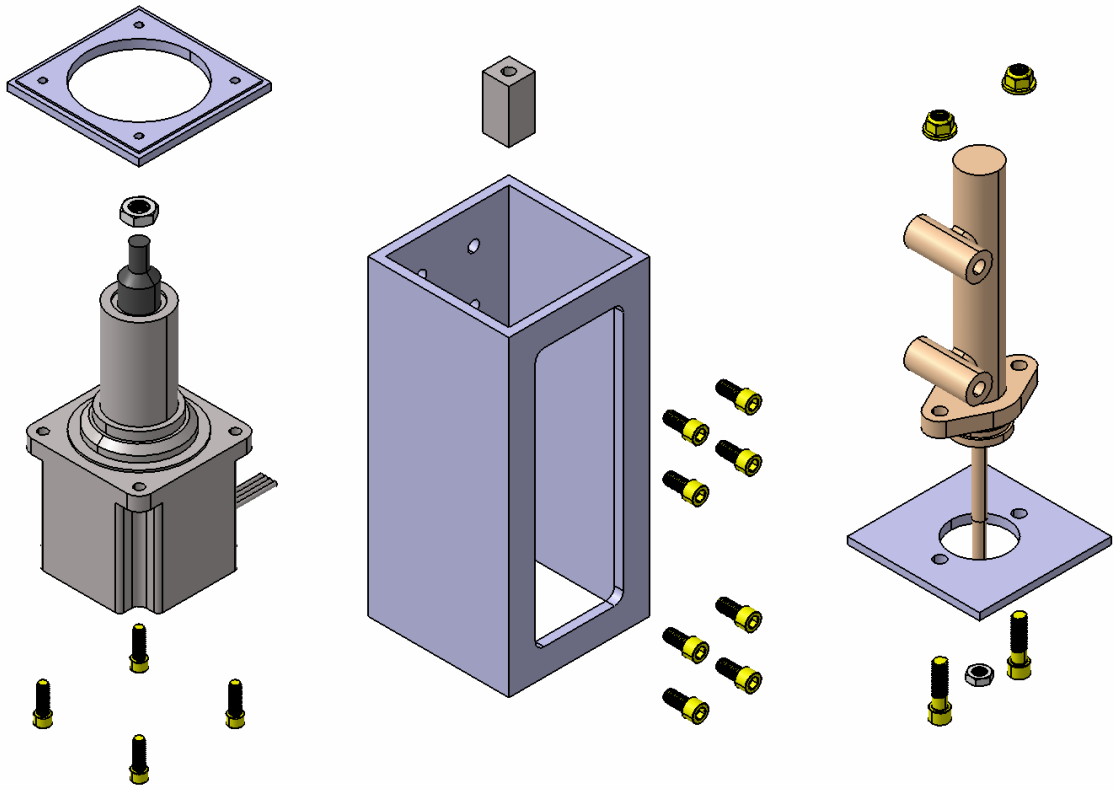


Figure F. 1: Brake actuator mount exploded view

F.2. Shaft encoder mount

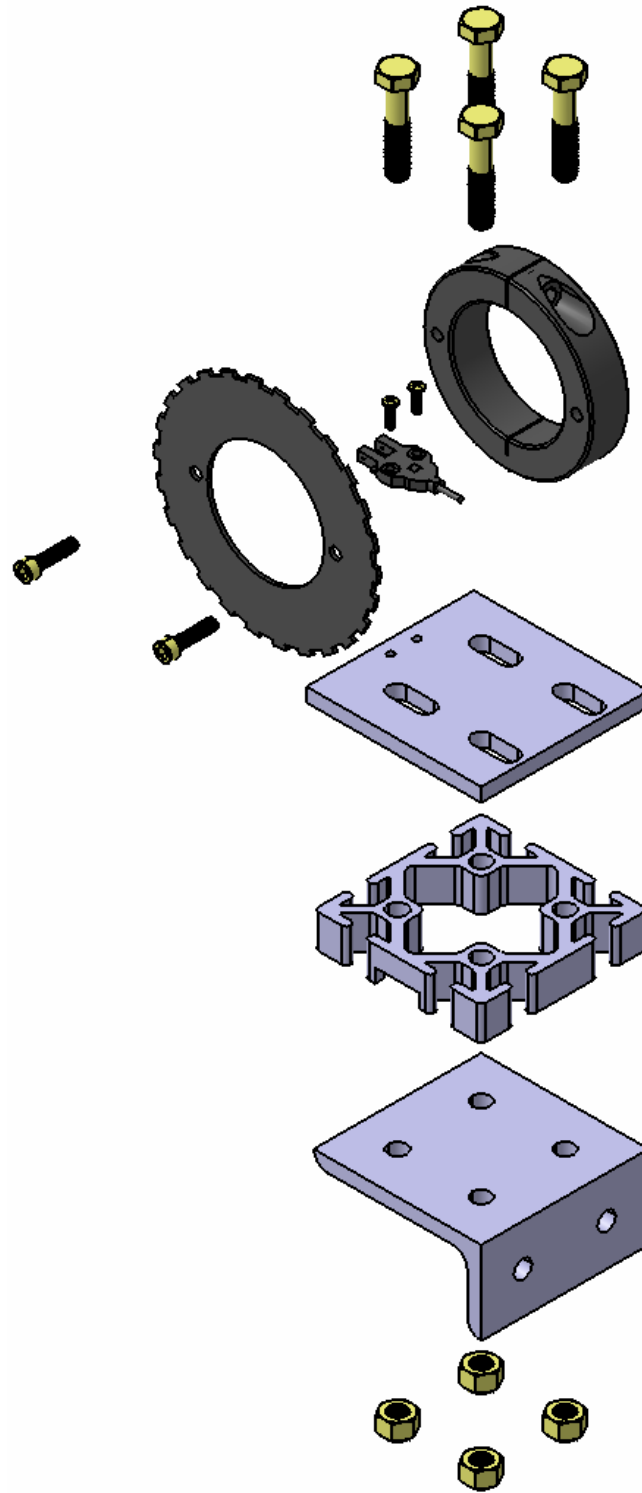


Figure F.2: Shaft encoder exploded view

F.3. Brake rotor and hat

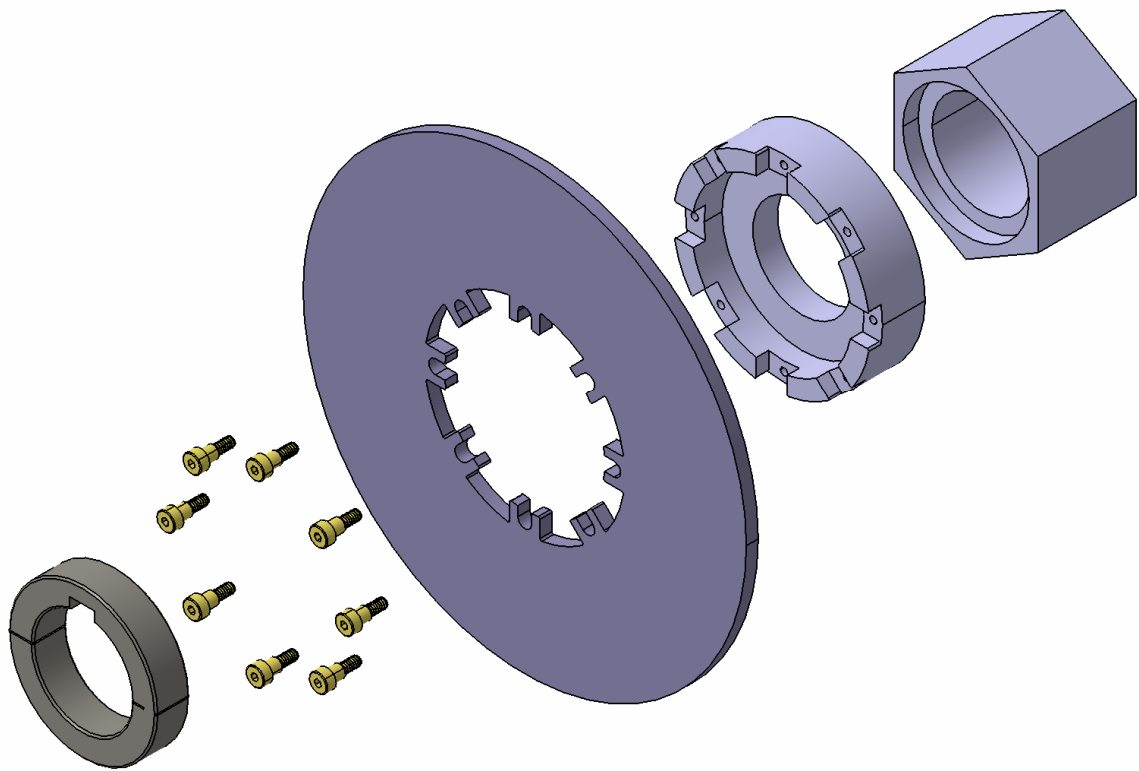


Figure F.3: Brake rotor and hat exploded view

F.4. Caliper mount

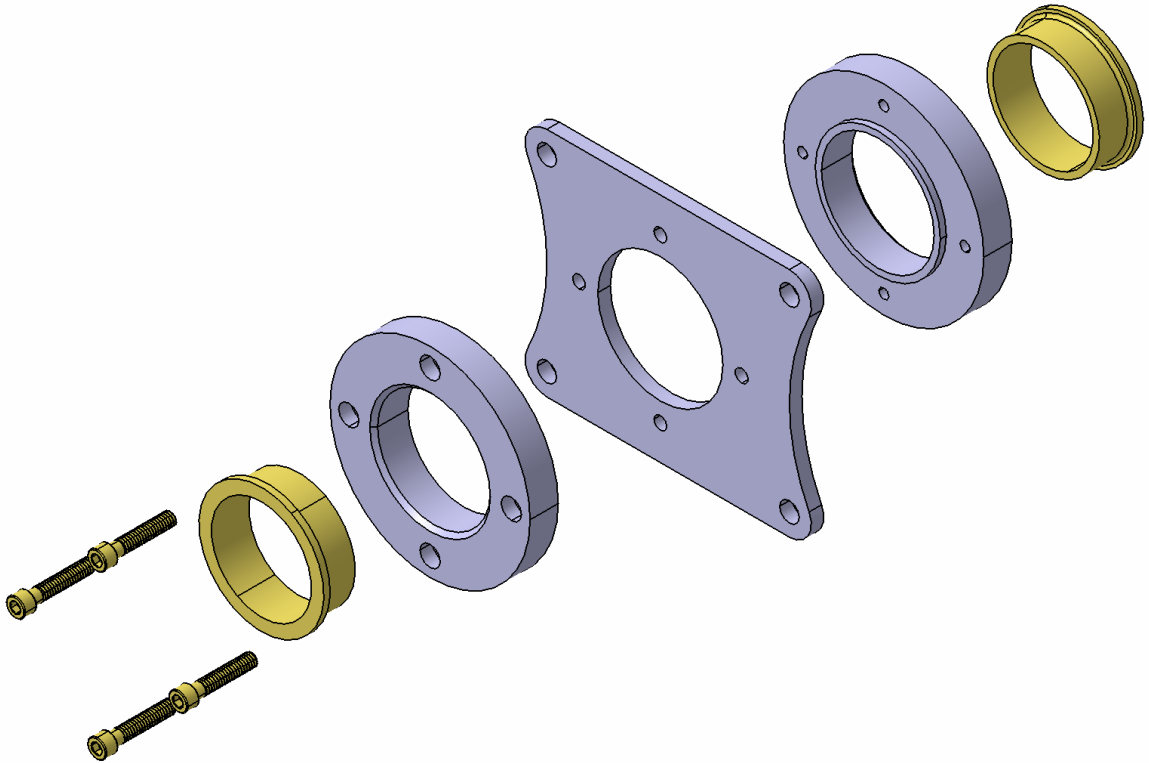


Figure F.4: Caliper mount exploded view

F.5. Load cell

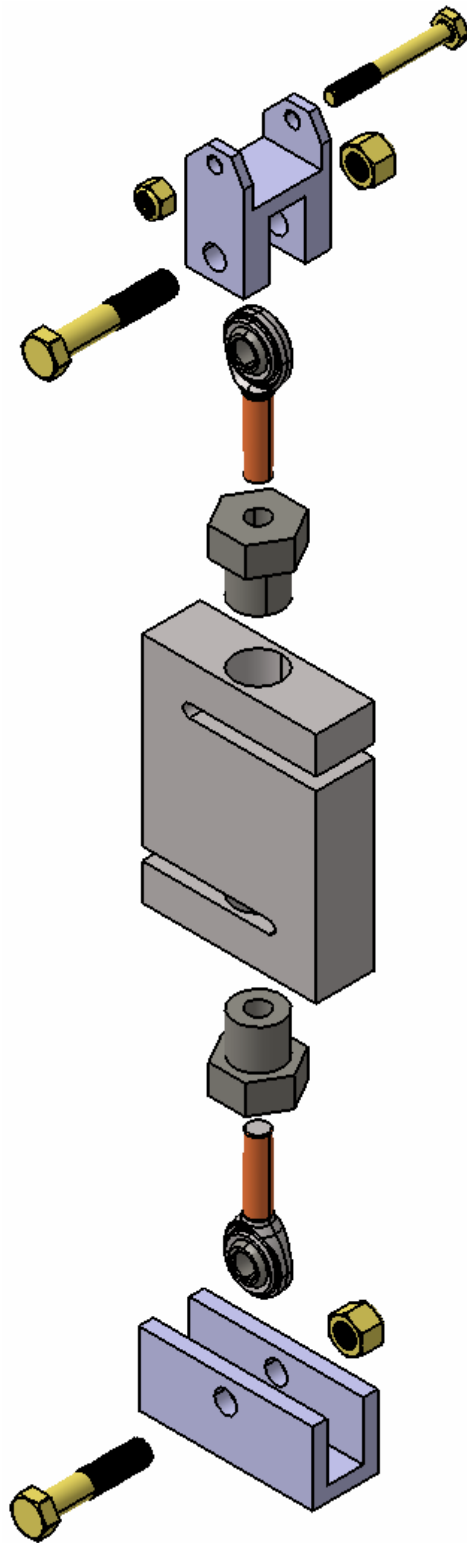


Figure F.5: Load cell exploded view

G. Verification Results

G.1. Bedding test procedures

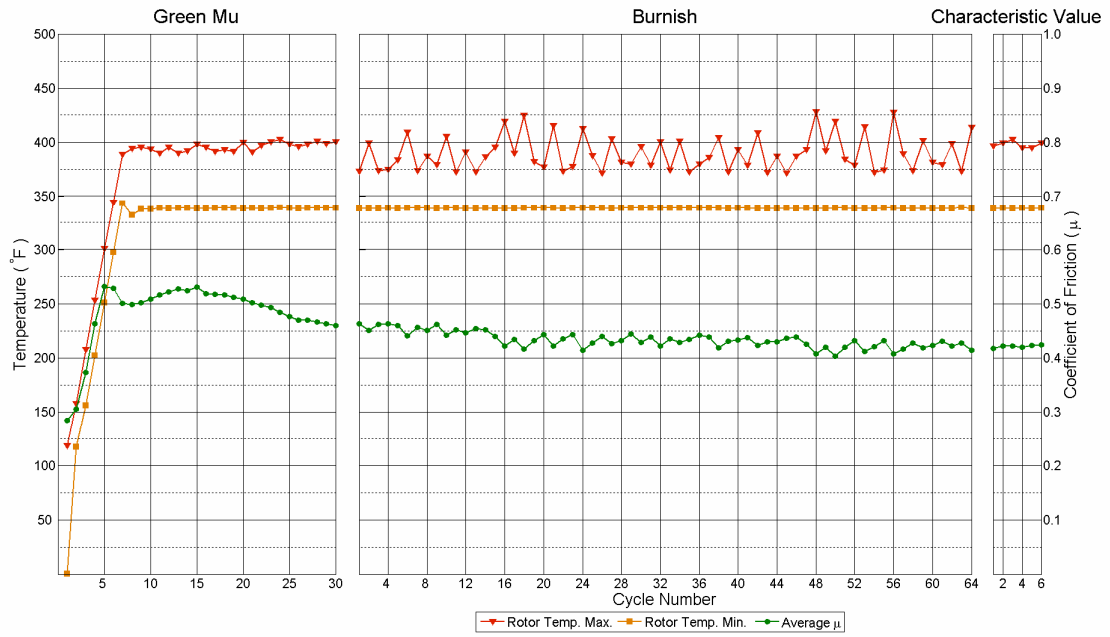


Figure G.1: Bedding test procedure results for control test specimen 1

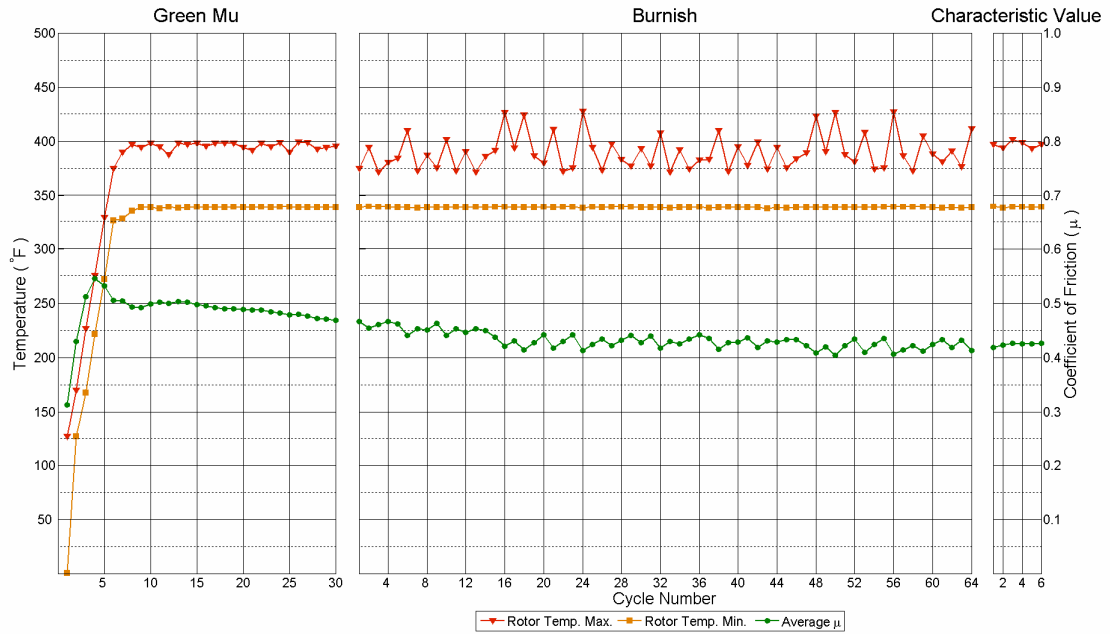


Figure G.2: Bedding test procedure results for treated test specimen 1

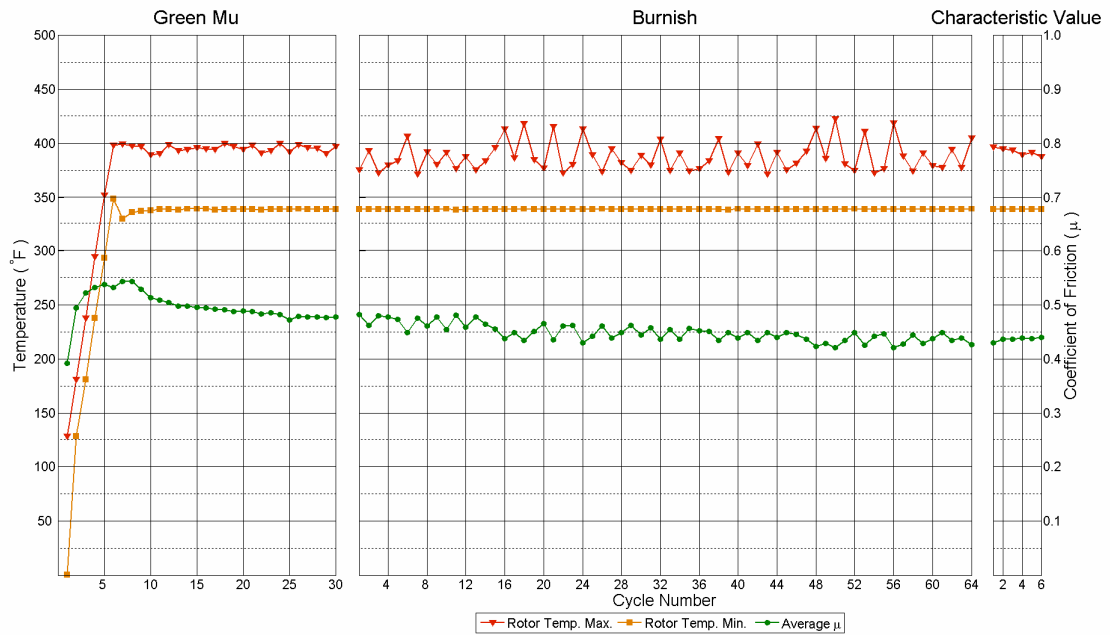


Figure G.3: Bedding test procedure results for control test specimen 2

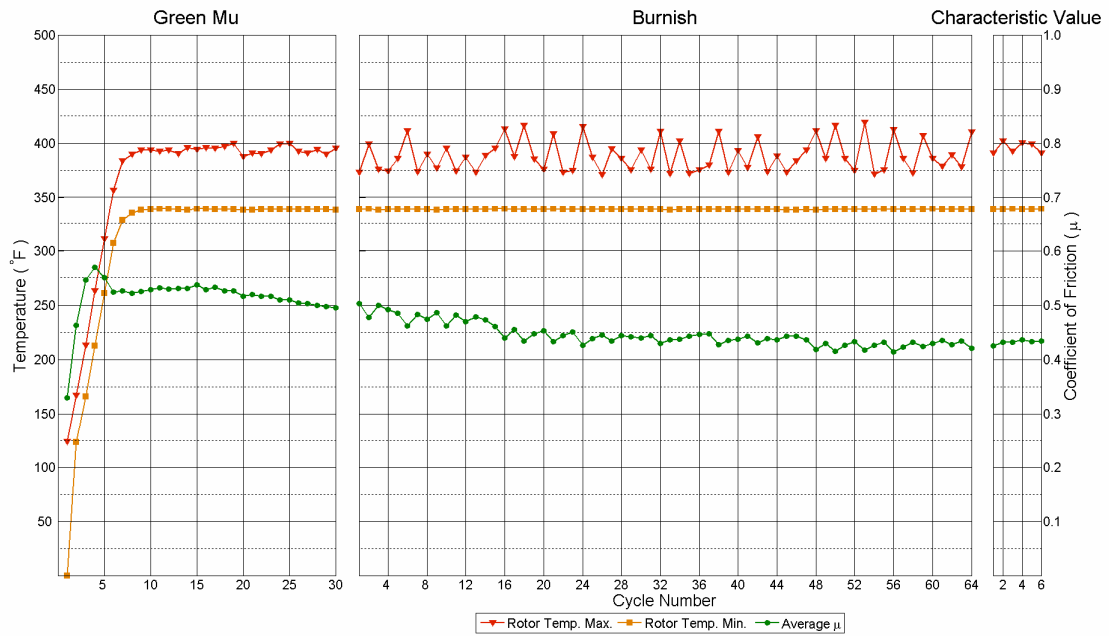


Figure G.4: Bedding test procedure results for treated test specimen 2

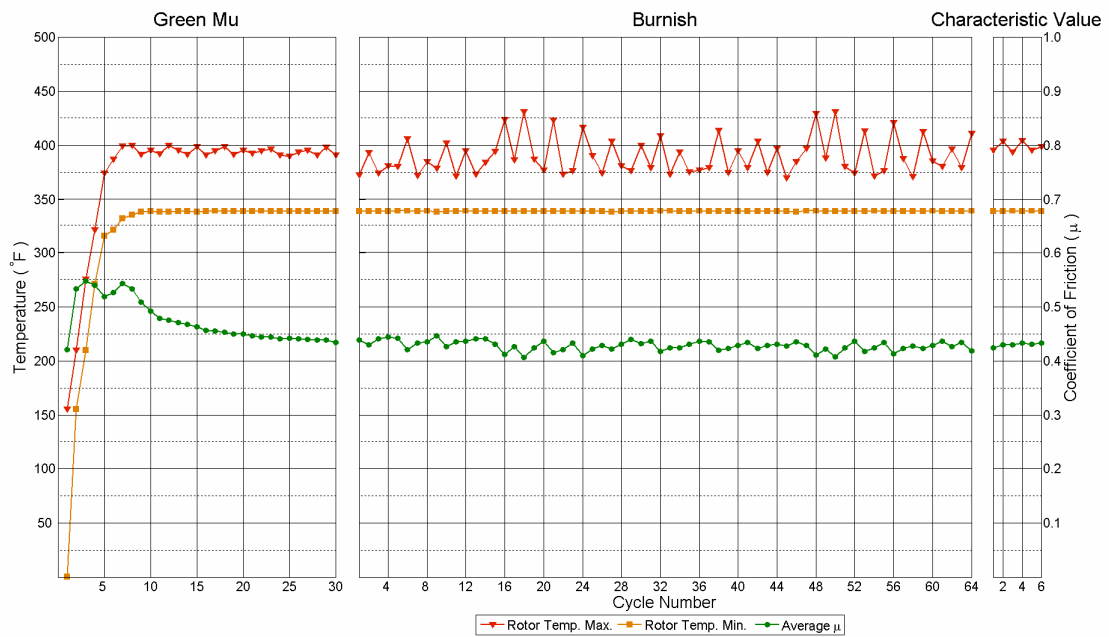


Figure G.5: Bedding test procedure results for treated test specimen 3

G.2. Wear test procedures

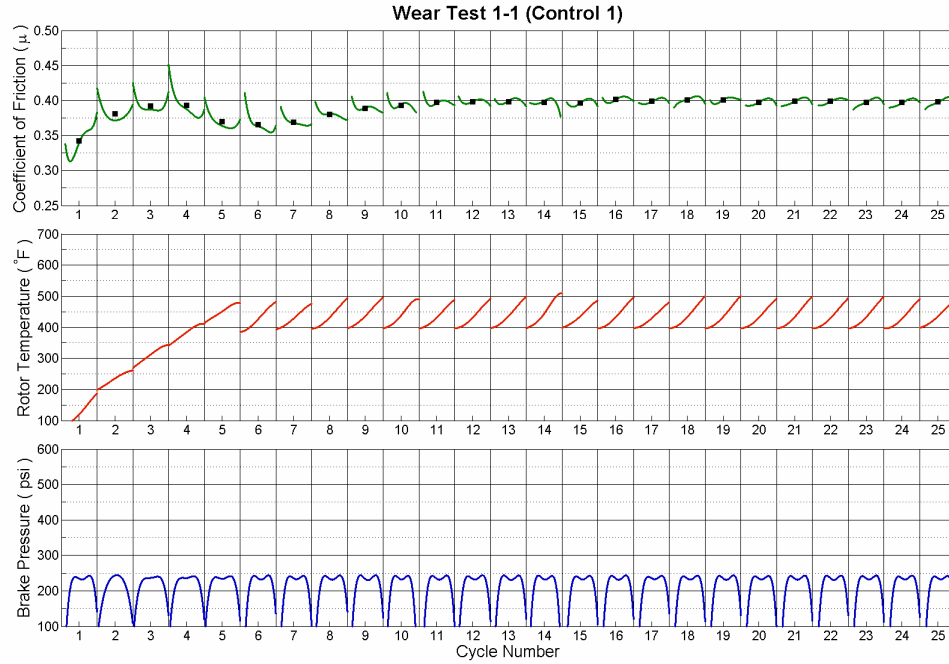


Figure G.6: Wear test procedure results for control test specimen 1, repetition 1

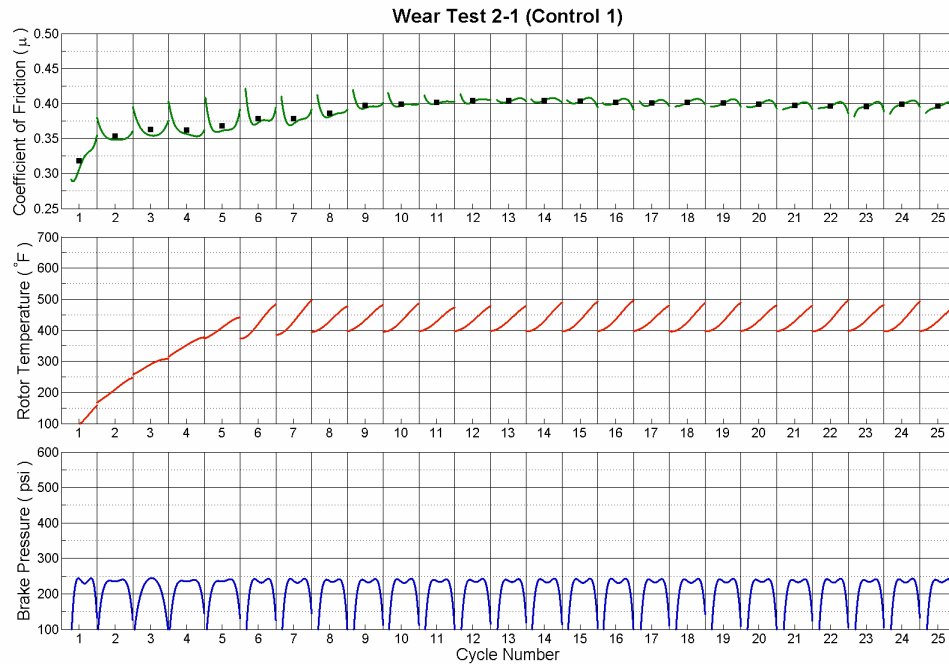


Figure G.7: Wear test procedure results for control test specimen 1, repetition 2

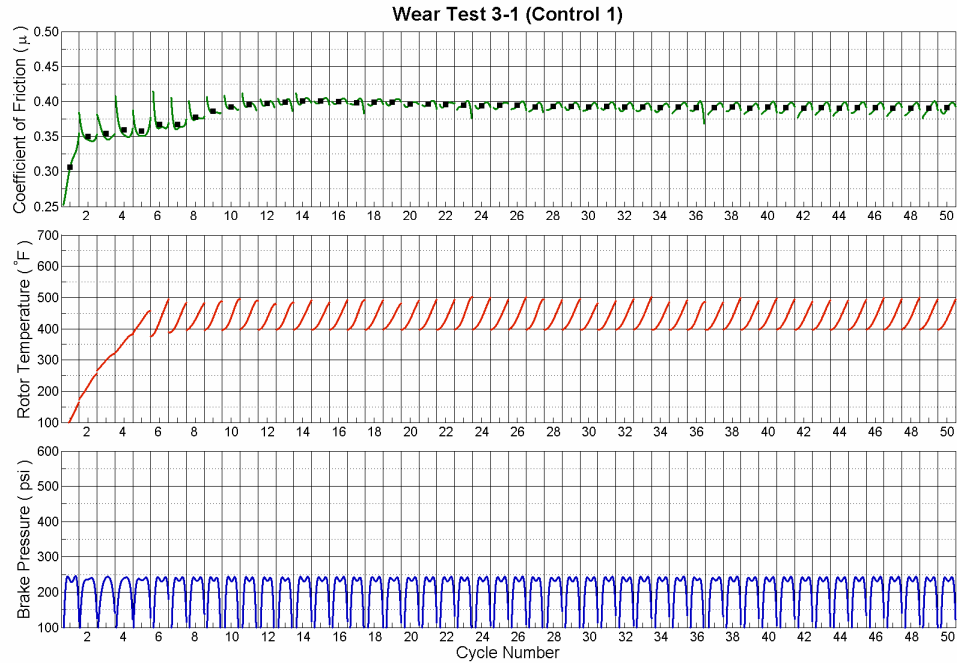


Figure G.8: Wear test procedure results for control test specimen 1, repetition 3

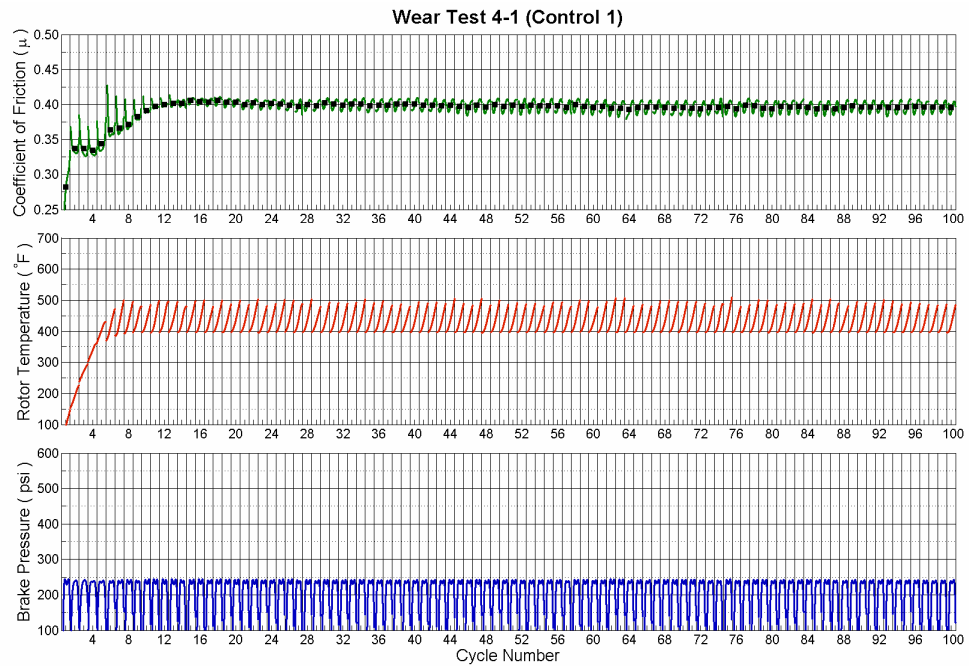


Figure G.9: Wear test procedure results for control test specimen 1, repetition 4

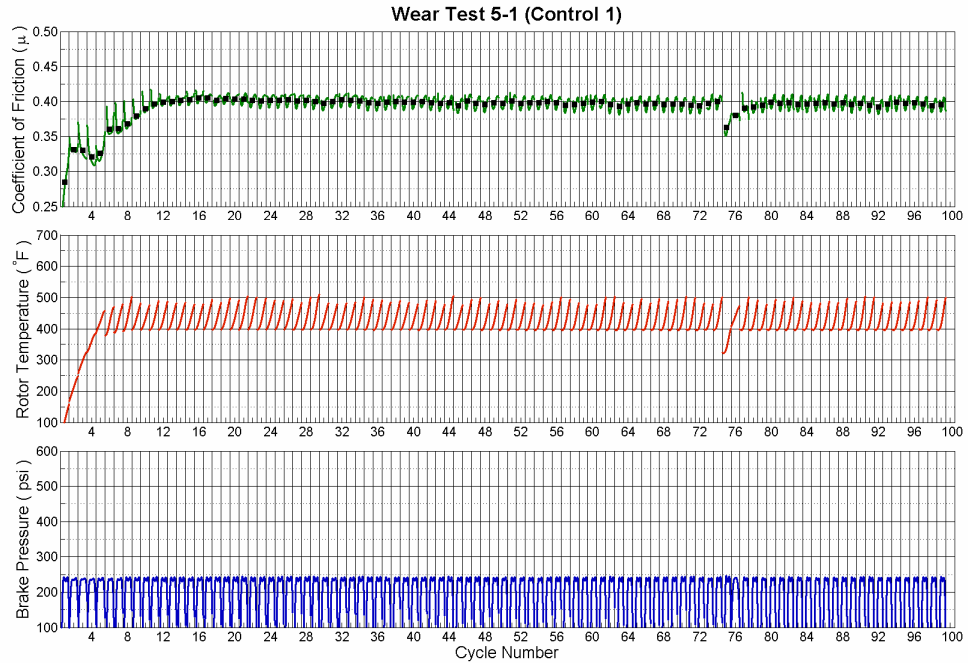


Figure G.10: Wear test procedure results for control test specimen 1, repetition 5

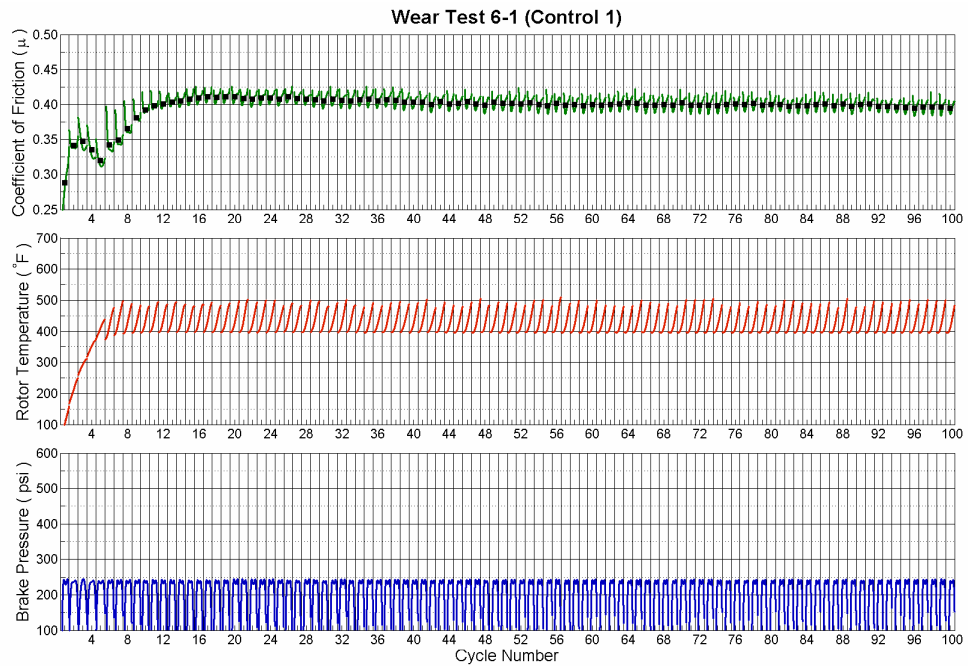


Figure G.11: Wear test procedure results for control test specimen 1, repetition 6

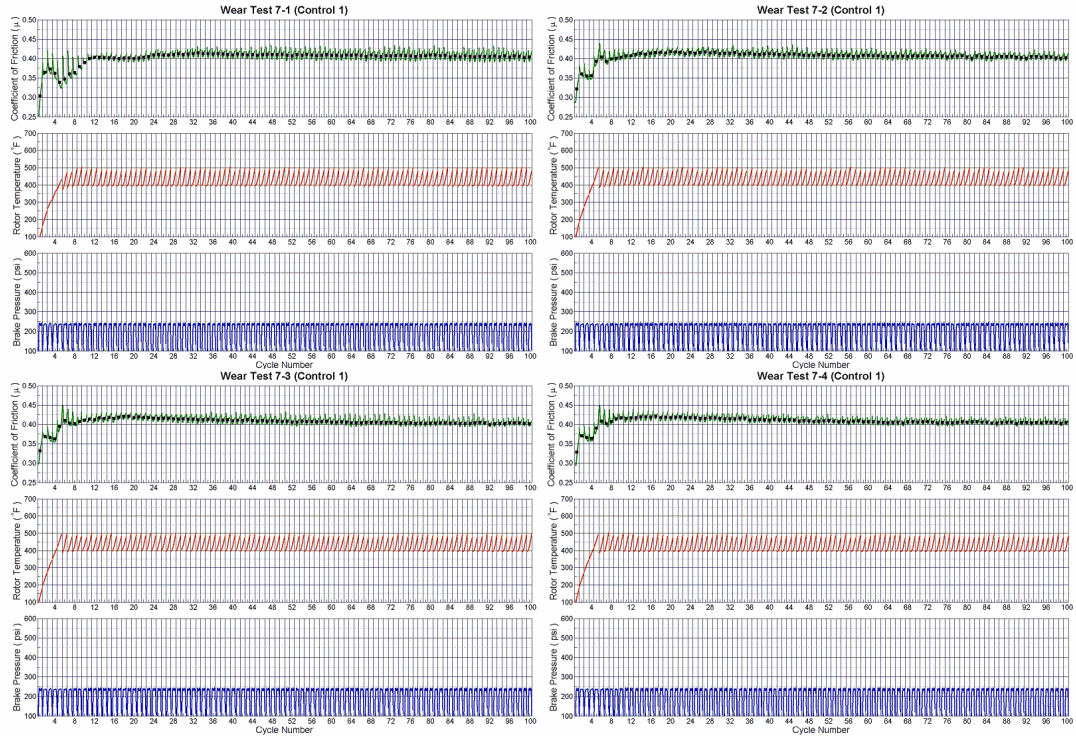


Figure G.12: Wear test procedure results for control test specimen 1, repetition 7

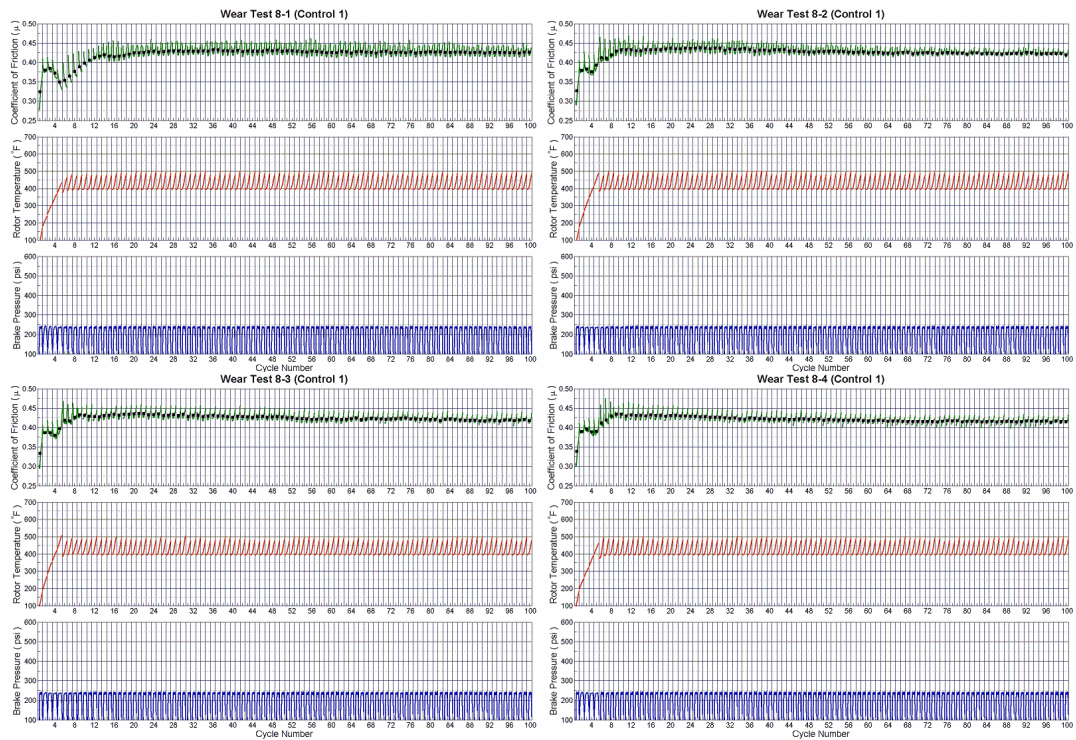


Figure G.13: Wear test procedure results for control test specimen 1, repetition 8

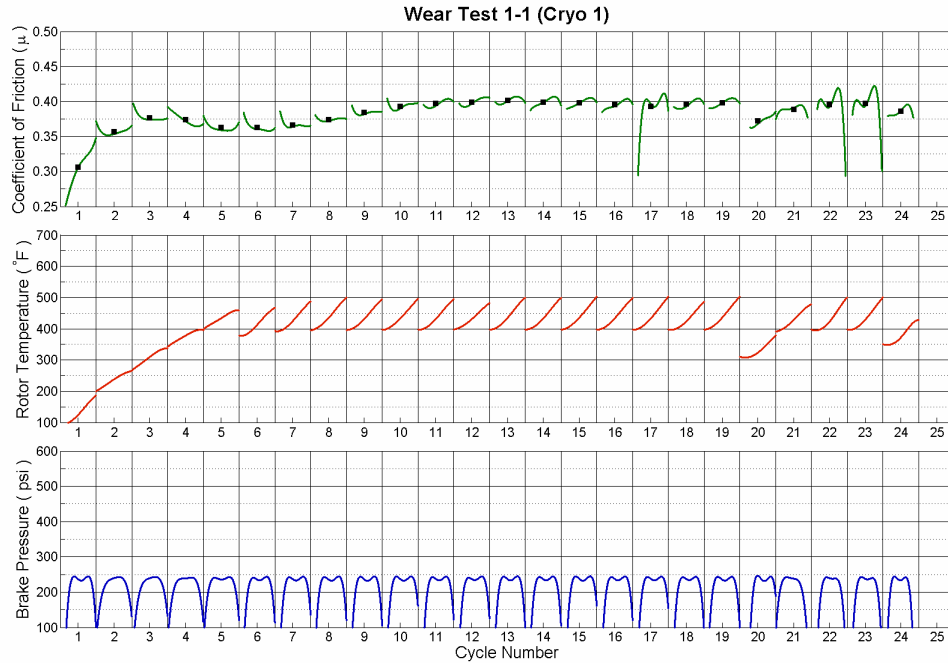


Figure G.14: Wear test procedure results for treated test specimen 1, repetition 1

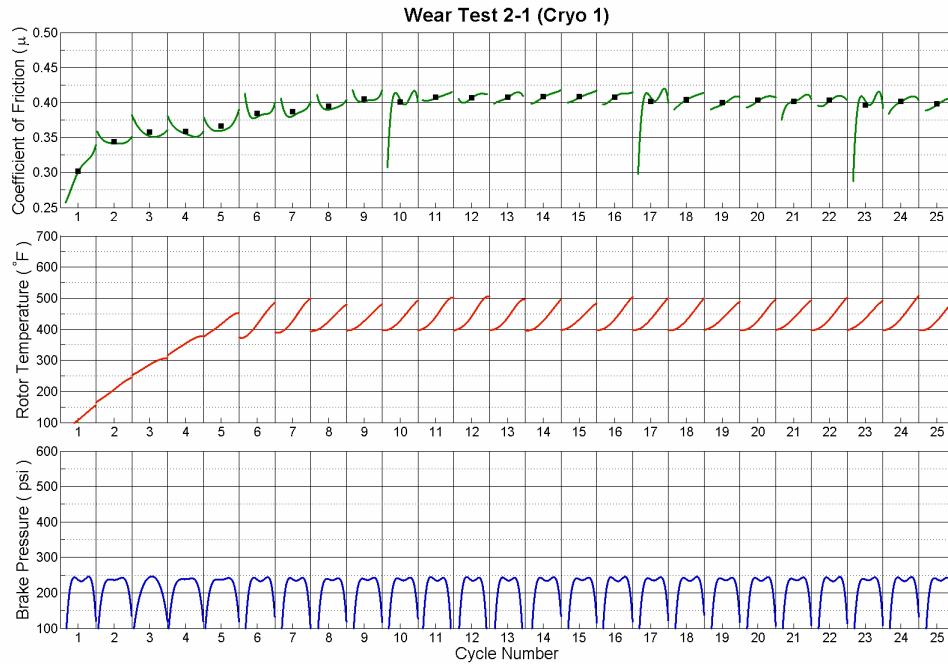


Figure G.15: Wear test procedure results for treated test specimen 1, repetition 2

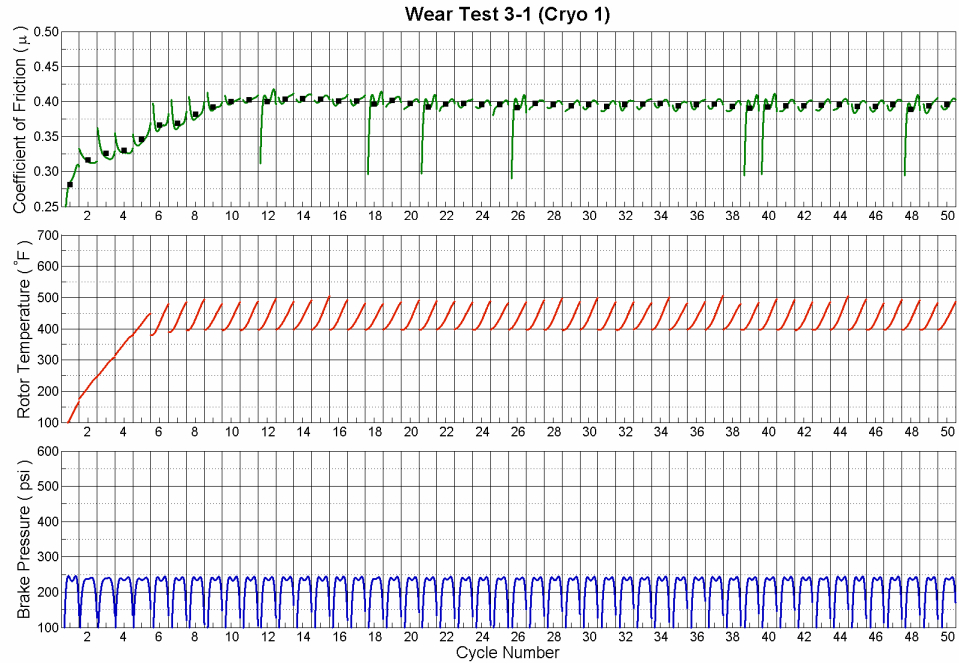


Figure G.16: Wear test procedure results for treated test specimen 1, repetition 3

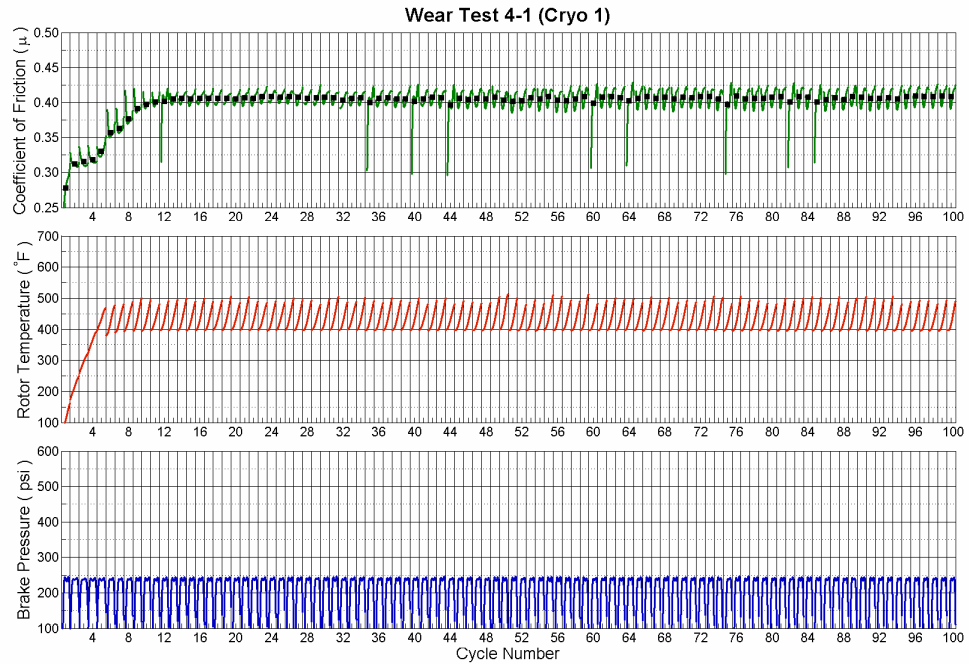


Figure G.17: Wear test procedure results for treated test specimen 1, repetition 4

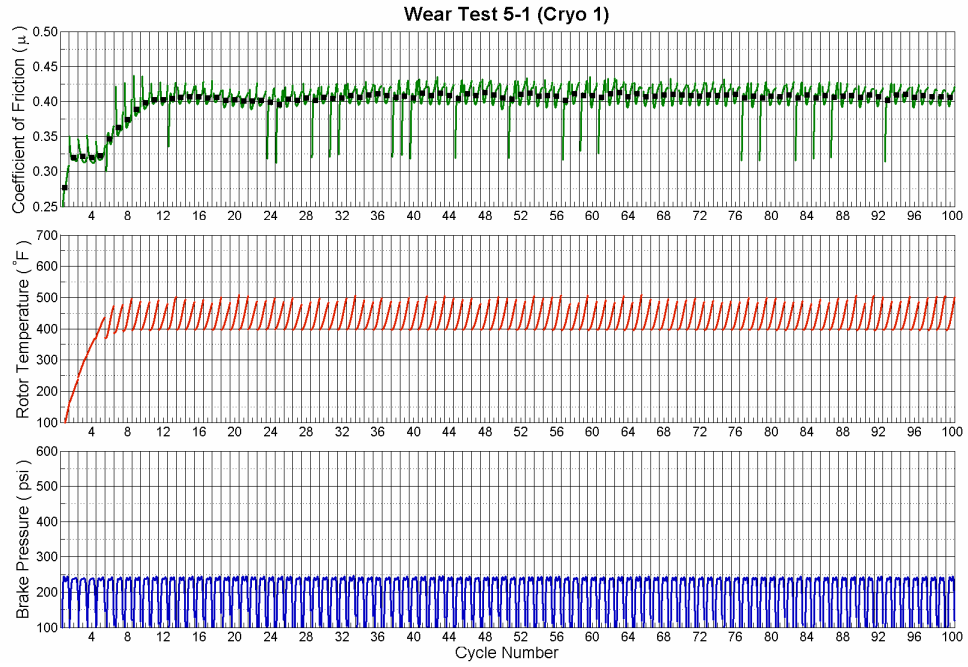


Figure G.18: Wear test procedure results for treated test specimen 1, repetition 5

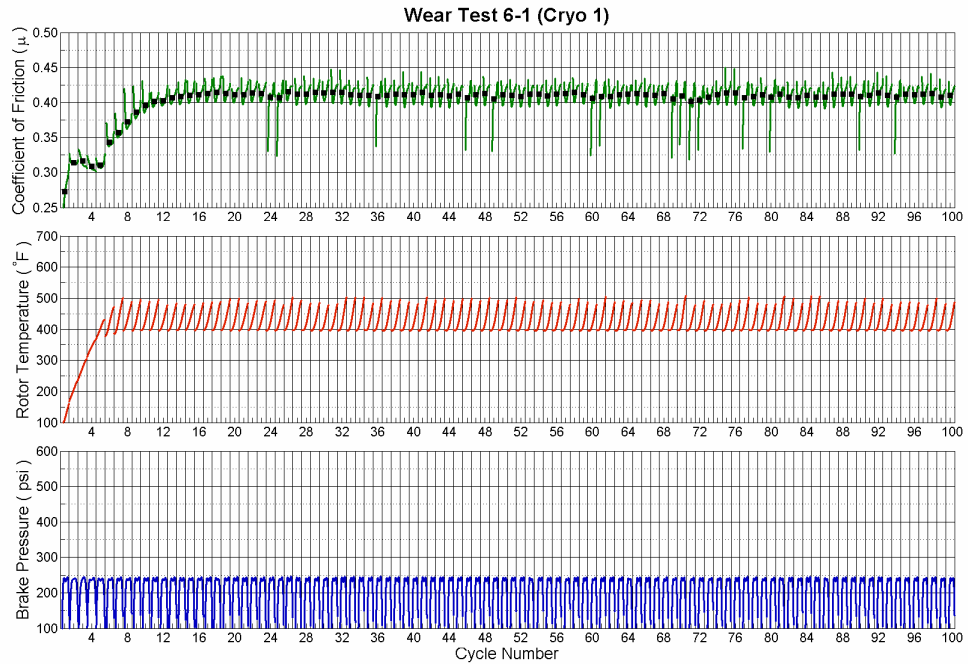


Figure G.19: Wear test procedure results for treated test specimen 1, repetition 6

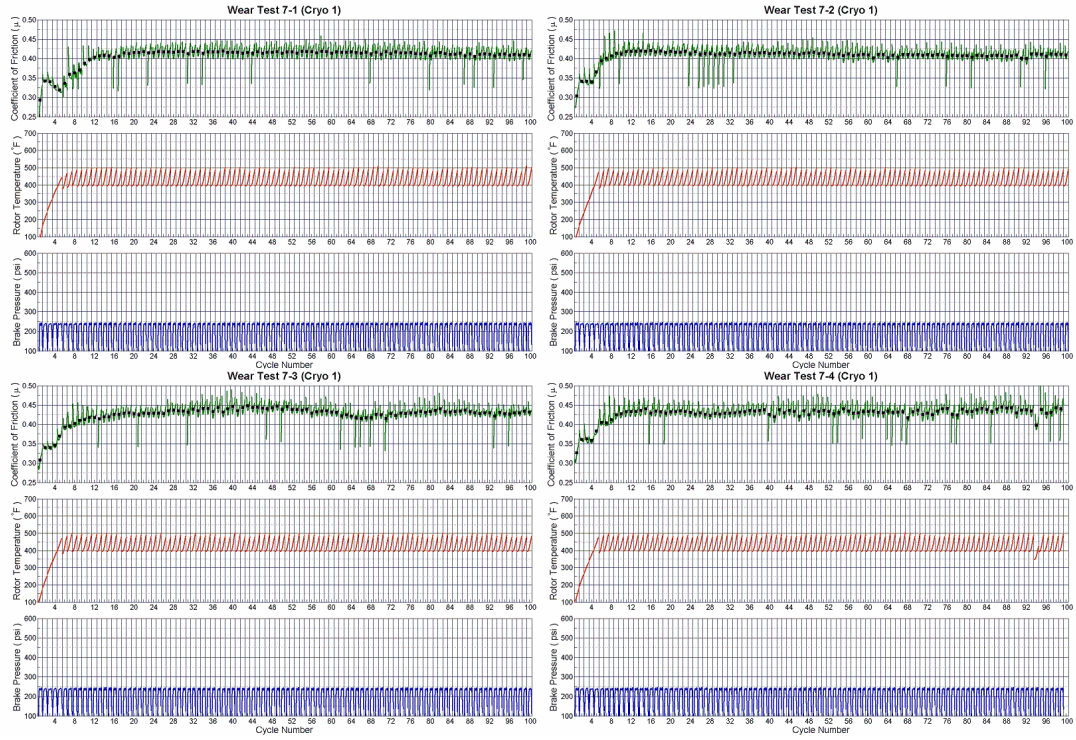


Figure G.20: Wear test procedure results for treated test specimen 1, repetition 7

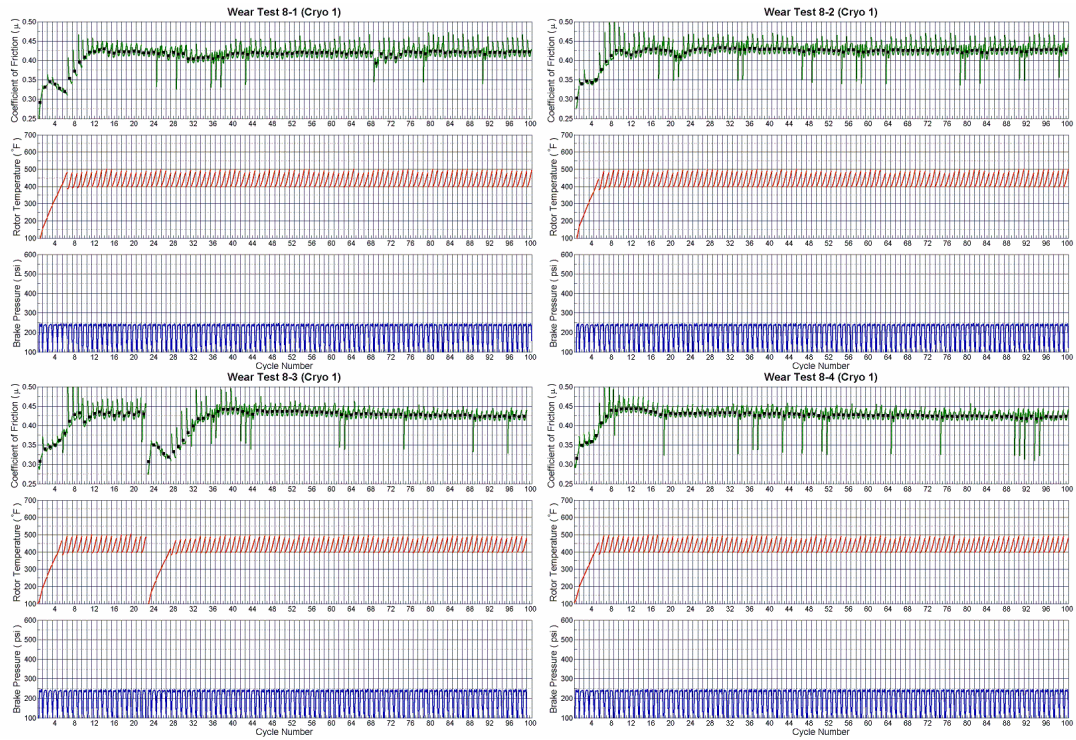


Figure G.21: Wear test procedure results for treated test specimen 1, repetition 8

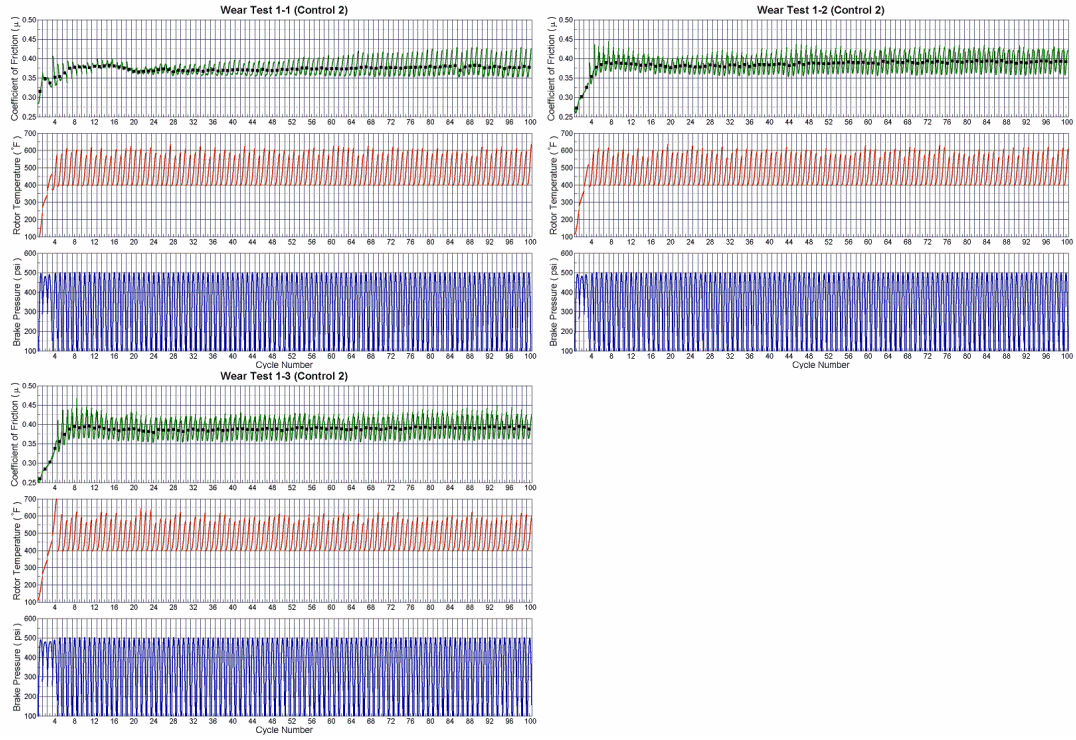


Figure G.22: Wear test procedure results for control test specimen 2, repetition 1

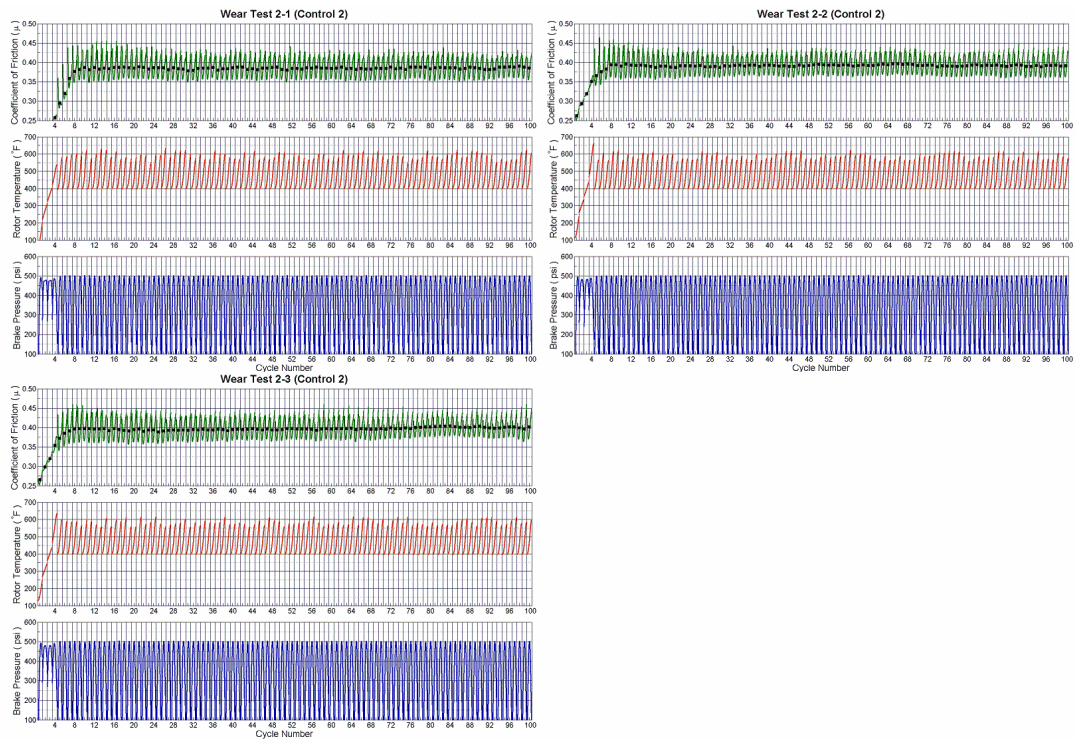


Figure G.23: Wear test procedure results for control test specimen 2, repetition 2

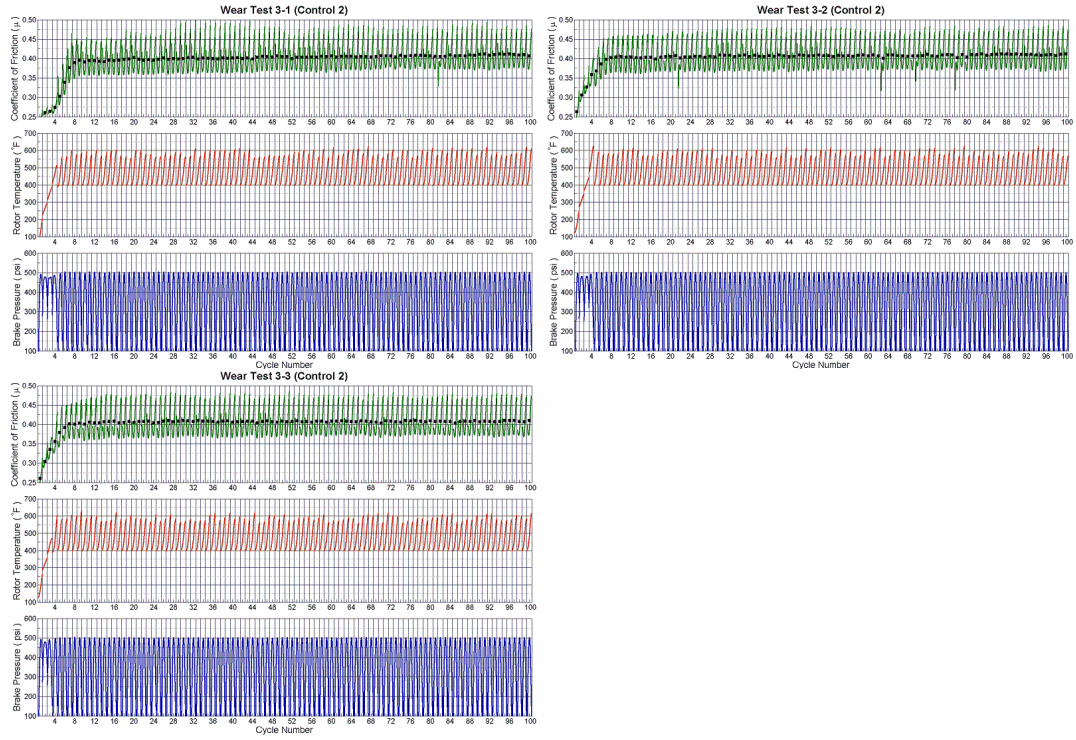


Figure G.24: Wear test procedure results for control test specimen 2, repetition 3

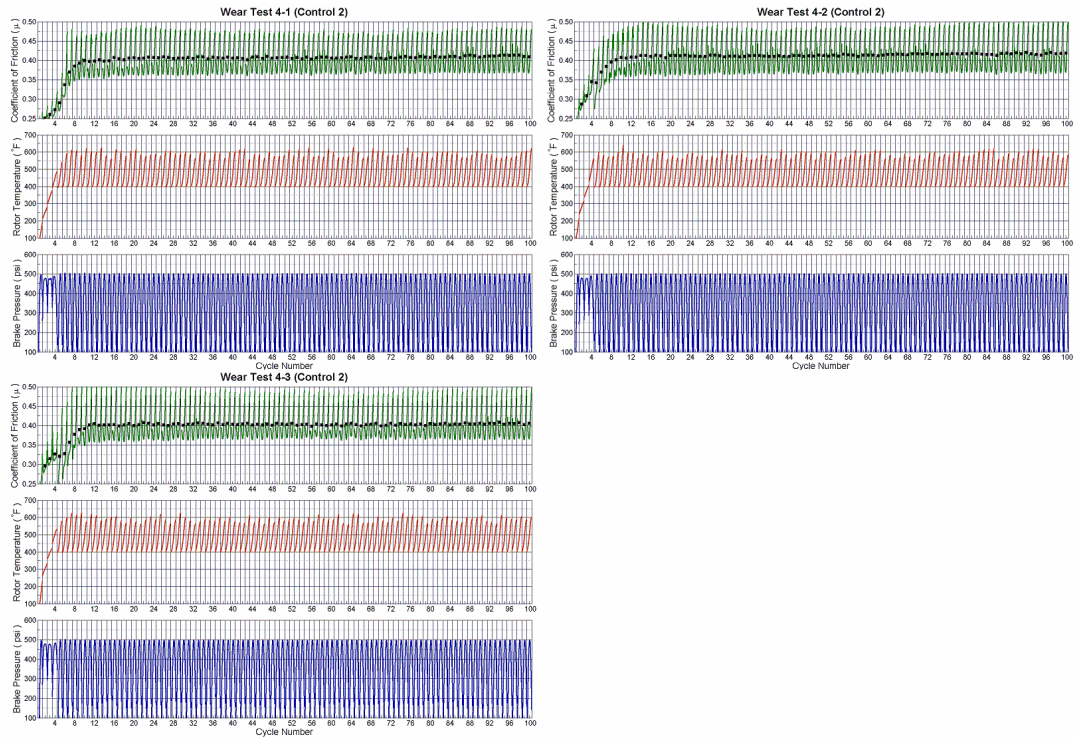


Figure G.25: Wear test procedure results for control test specimen 2, repetition 4

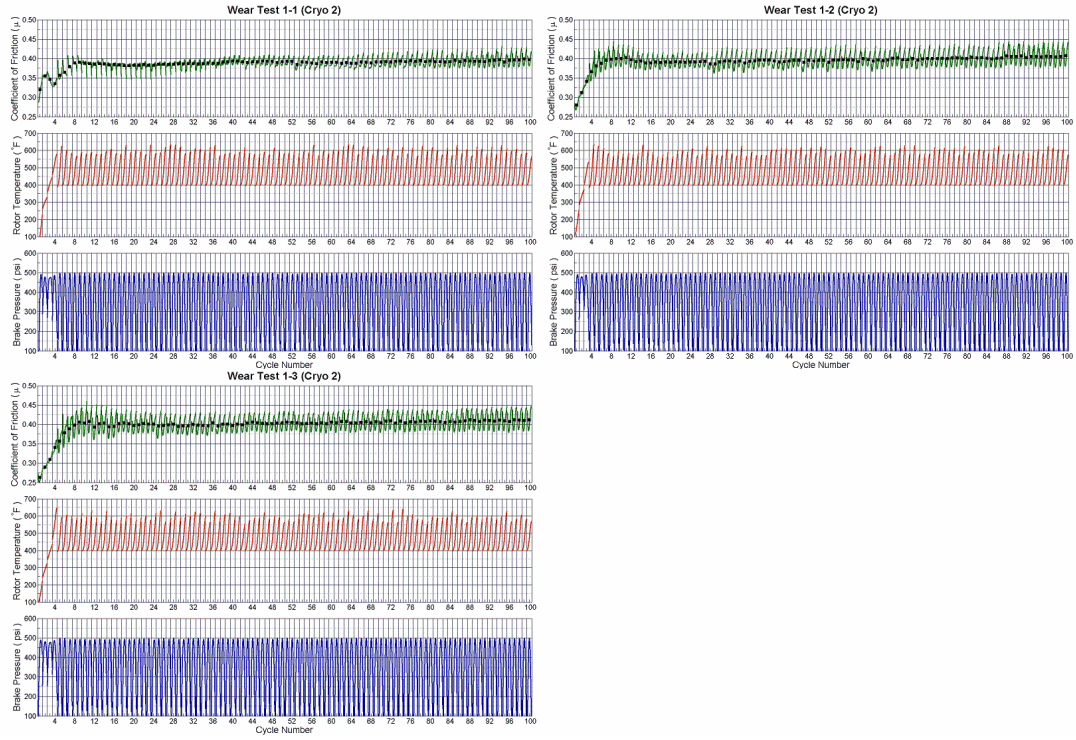


Figure G.26: Wear test procedure results for treated test specimen 2, repetition 1

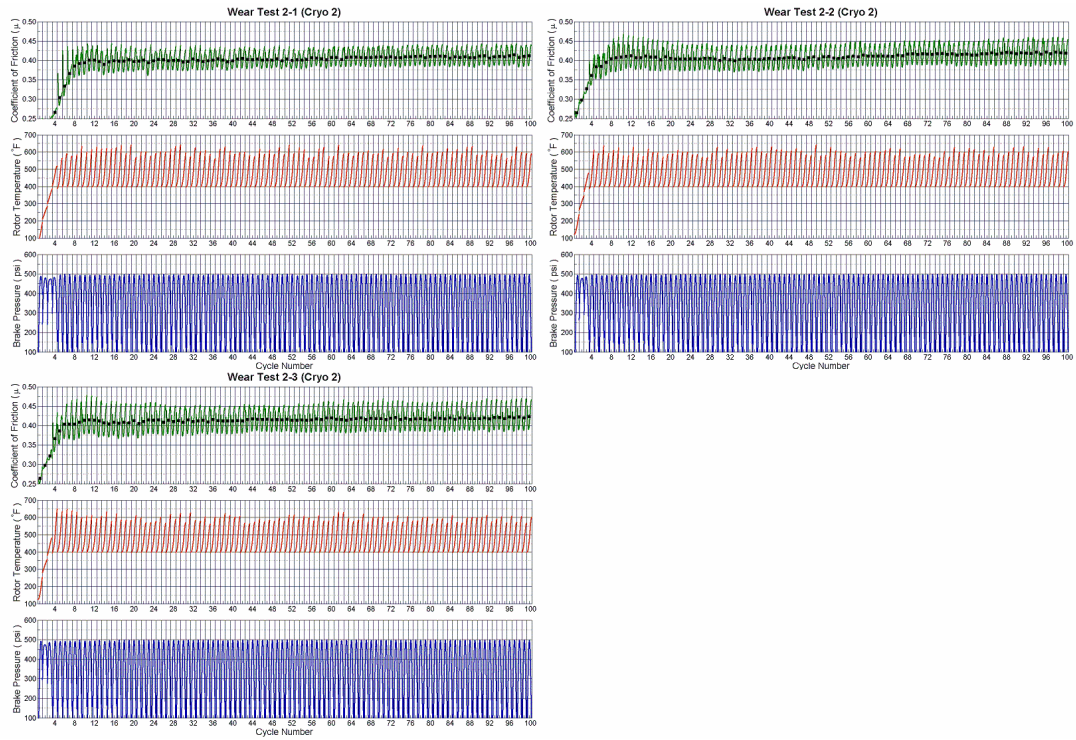


Figure G.27: Wear test procedure results for treated test specimen 2, repetition 2

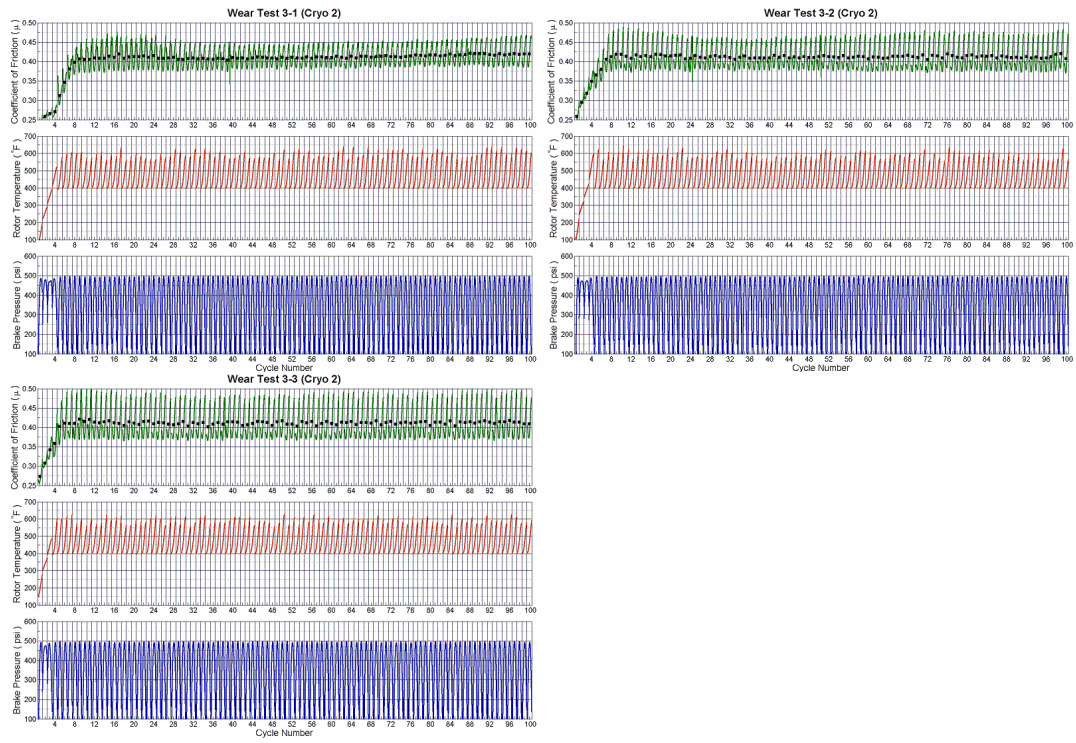


Figure G.28: Wear test procedure results for treated test specimen 2, repetition 3

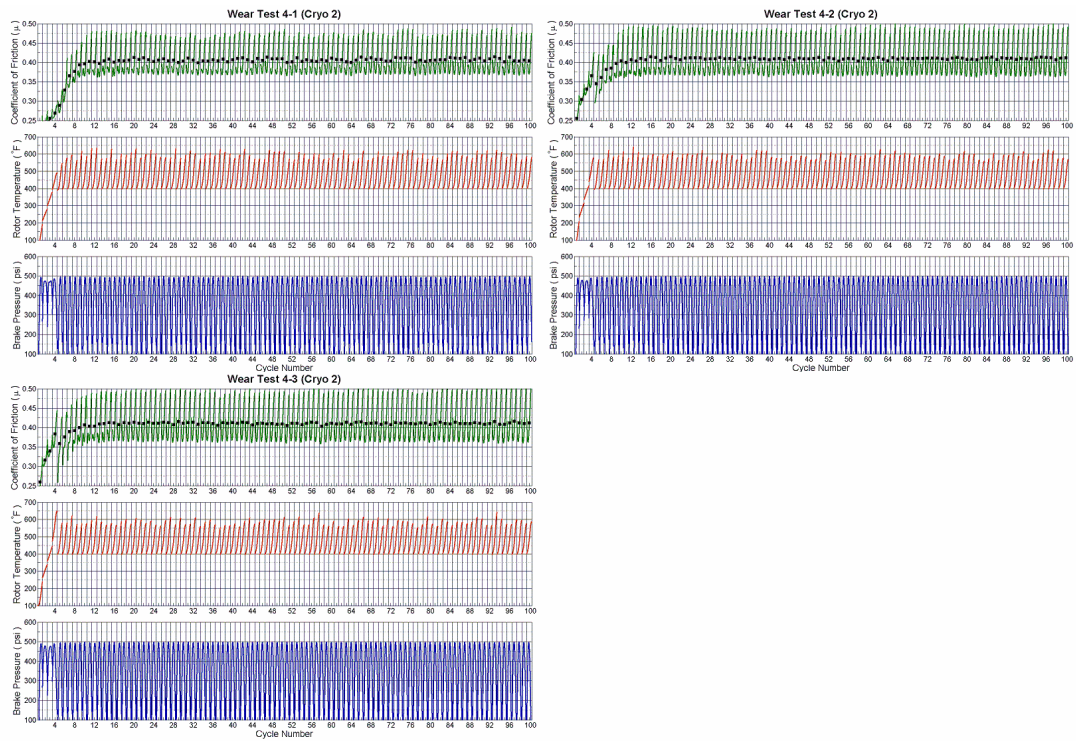


Figure G.29: Wear test procedure results for treated test specimen 2, repetition 4

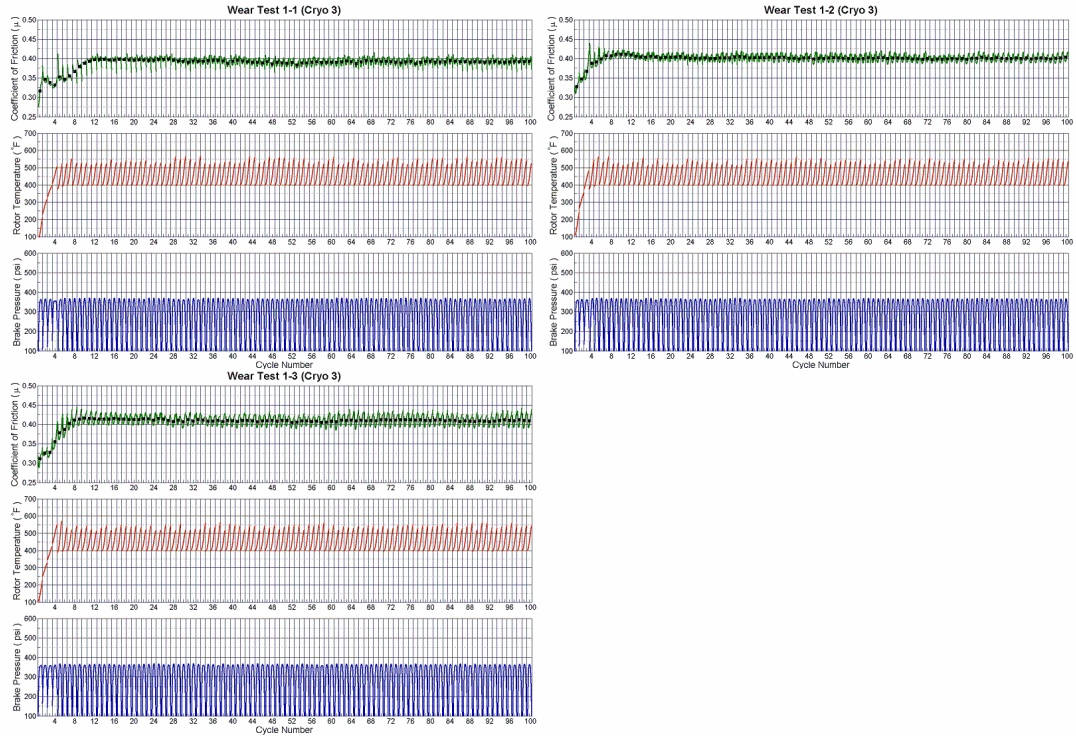


Figure G.30: Wear test procedure results for treated test specimen 3, repetition 1

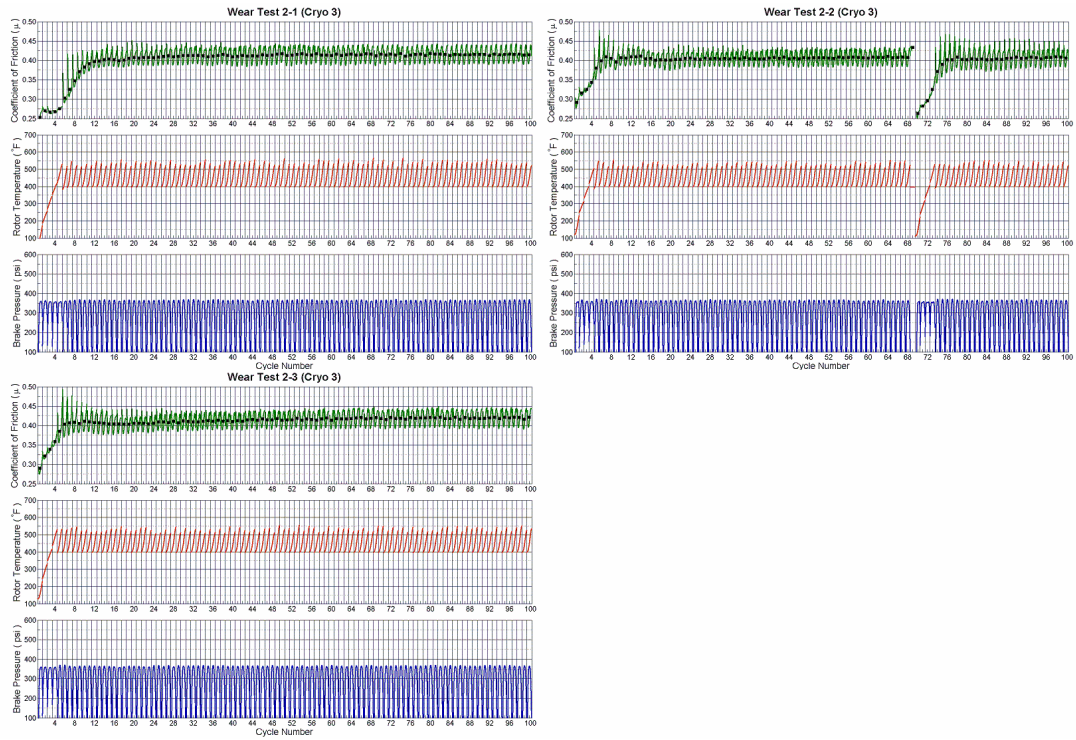


Figure G.31: Wear test procedure results for treated test specimen 3, repetition 2

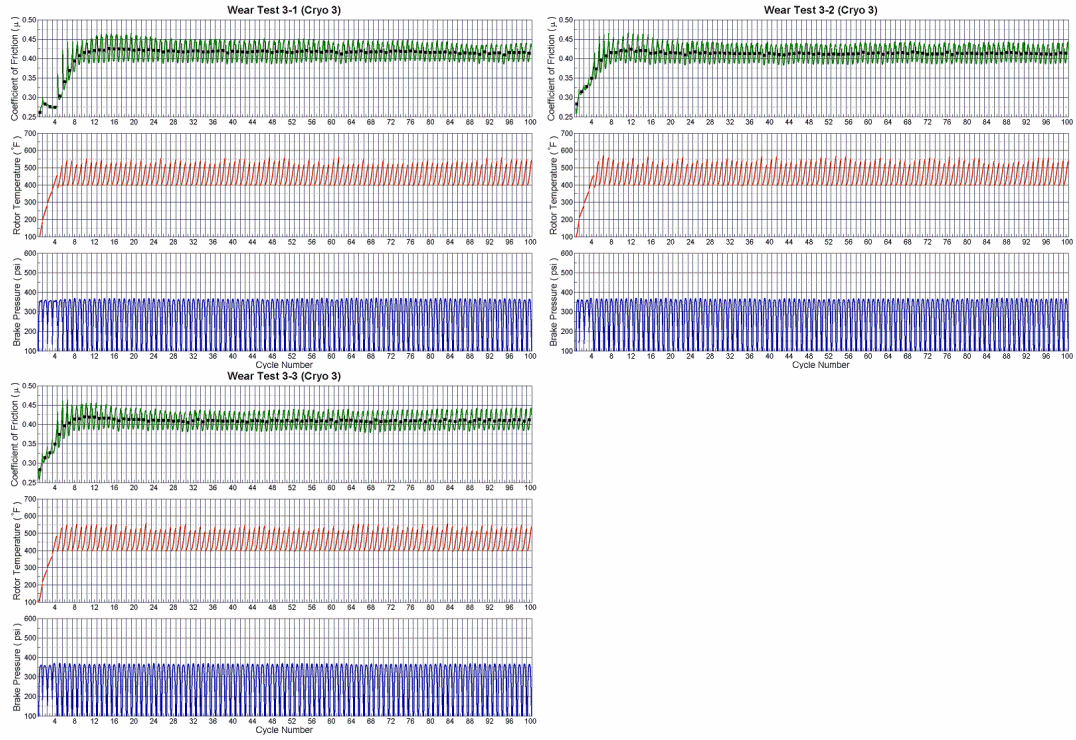


Figure G.32: Wear test procedure results for treated test specimen 3, repetition 3

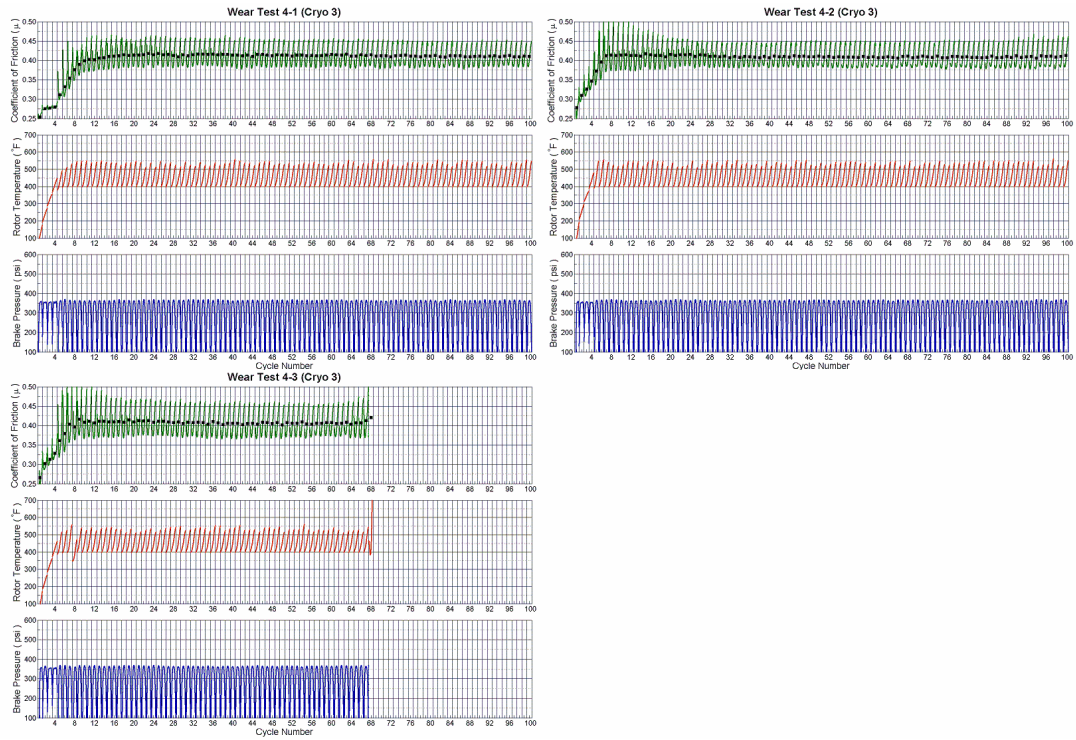


Figure G.33: Wear test procedure results for treated test specimen 3, repetition 4

G.3. Brake rotor and pad mass loss

Table G.1: Individual brake rotor mass loss (g)

Test Procedure	Control 1	Treated 1	Control 2	Treated 2	Treated 3
Bedding	0.52	0.37	*0.61*	0.44	*0.50*
Repetition 1	0.08	0.04	0.86	0.77	0.19
Repetition 2	0.02	0.02	0.84	0.75	0.40
Repetition 3	0.03	0.05	0.80	0.80	0.33
Repetition 4	*0.06*	*0.10*	0.84	0.94	*0.64*
Repetition 5	0.02	0.05	--	--	--
Repetition 6	0.05	0.01	--	--	--
Repetition 7	0.12	0.20	--	--	--
Repetition 8	0.16	0.23	--	--	--
Totals →	1.06	1.07	3.95	3.70	2.06

Table G.2: Individual brake pad mass loss (g)

Test Procedure	Control 1	Treated 1	Control 2	Treated 2	Treated 3
Bedding	0.5531	0.6345	0.7615	0.6678	0.8130
Repetition 1	0.2343	0.1682	2.9035	2.7099	1.4792
Repetition 2	0.0134	0.0095	3.3915	2.8947	1.7279
Repetition 3	0.1886	0.1530	3.4935	3.1655	1.6229
Repetition 4	0.2868	0.3410	3.2501	3.5899	*2.4347*
Repetition 5	0.2104	0.2814	--	--	--
Repetition 6	0.2243	0.1900	--	--	--
Repetition 7	0.9921	1.2013	--	--	--
Repetition 8	1.1893	1.3259	--	--	--
Totals →	3.8923	4.3048	13.8001	13.0278	8.0777

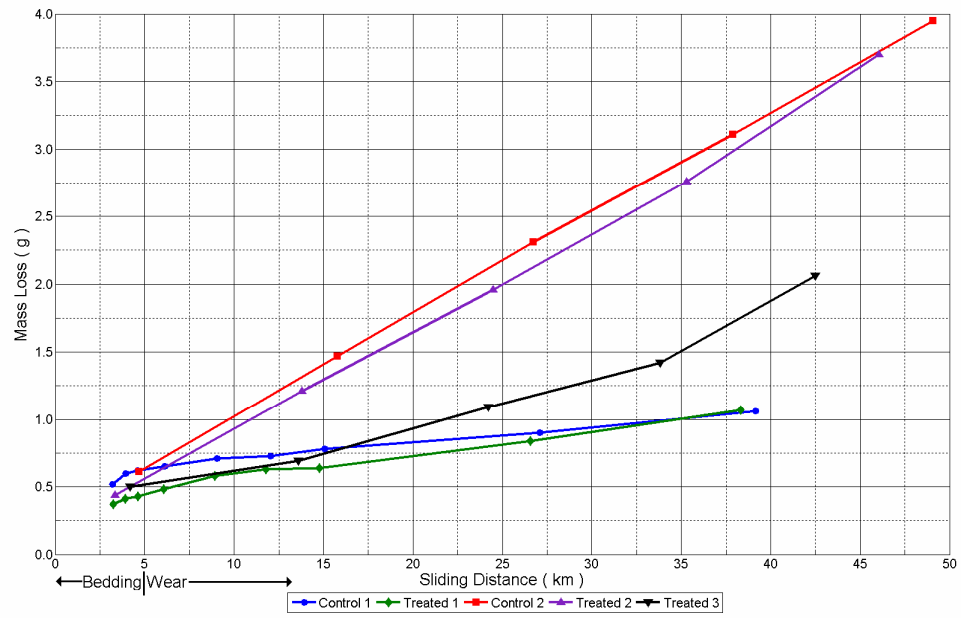


Figure G.34: Cumulative brake rotor mass loss (g) verses sliding distance (km)

Table G.3: Cumulative brake rotor mass loss (g)

Test Procedure	Control 1	Treated 1	Control 2	Treated 2	Treated 3
Bedding	0.52	0.37	*0.61*	0.44	*0.50*
Repetition 1	0.60	0.41	1.47	1.21	0.69
Repetition 2	0.62	0.43	2.31	1.96	1.09
Repetition 3	0.65	0.48	3.11	2.76	1.42
Repetition 4	*0.71*	*0.58*	3.95	3.70	*2.06*
Repetition 5	0.73	0.63	--	--	--
Repetition 6	0.78	0.64	--	--	--
Repetition 7	0.90	0.84	--	--	--
Repetition 8	1.06	1.07	--	--	--

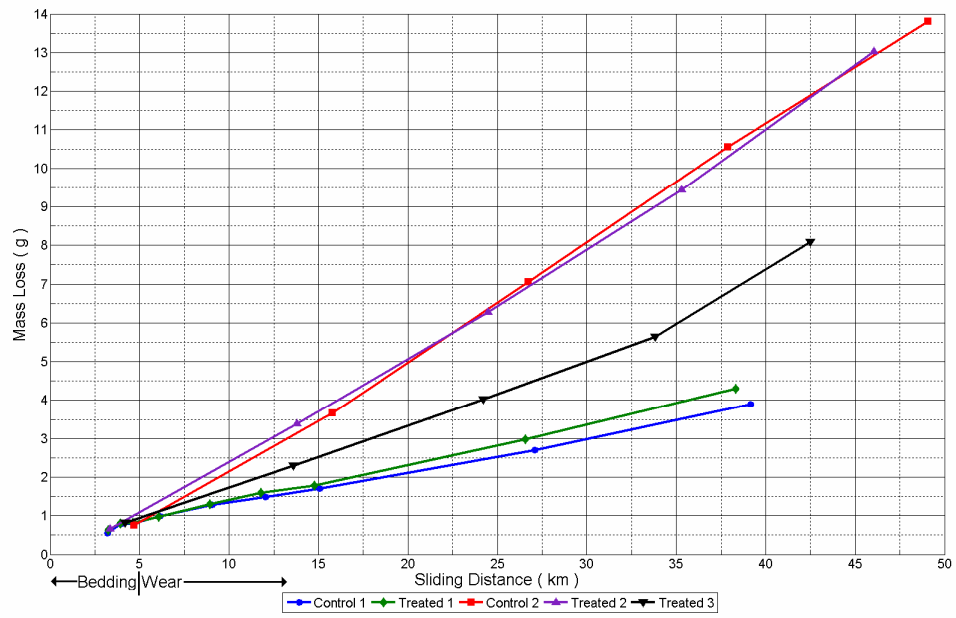


Figure G.35: Cumulative brake pad mass loss (g) versus sliding distance (km)

Table G.4: Cumulative brake pad mass loss (g)

Test Procedure	Control 1	Treated 1	Control 2	Treated 2	Treated 3
Bedding	0.5531	0.6345	0.7615	0.6678	0.8130
Repetition 1	0.7874	0.8027	3.6650	3.3777	2.2922
Repetition 2	0.8008	0.8122	7.0565	6.2724	4.0201
Repetition 3	0.9894	0.9652	10.5500	9.4379	5.6430
Repetition 4	1.2762	1.3062	13.8001	13.0278	*8.0777*
Repetition 5	1.4866	1.5876	--	--	--
Repetition 6	1.7109	1.7776	--	--	--
Repetition 7	2.7030	2.9789	--	--	--
Repetition 8	3.8923	4.3048	--	--	--

